Title
Novel Magnetoelastic Materials for Multiferroic Applications

Author
Lee, Taehwan

Publication Date
2019

UNIVERSITY OF CALIFORNIA

Los Angeles

Novel Magnetoelastic Materials for Multiferroic Applications

A dissertation submitted in partial satisfaction of the
requirements for the degree Doctor of Philosophy
in Materials Science and Engineering

by

Taehwan Lee

2019

ABSTRACT OF THE DISSERTATION

Novel Magnetoelastic Materials for Multiferroic Applications

by

Taehwan Lee
Doctor of Philosophy in Materials Science and Engineering
University of California, Los Angeles, 2019
Professor Gregory P. Carman, Chair

Controlling magnetic properties using other parameters (i.e. voltage, strain, and current) than the magnetic field has been extensively investigated to reduce the physical dimensions and energy consumption of spintronic devices. Among several options, the strain is the most energy-efficient way to modulate magnetic properties. The high-quality and functional magnetoelastic materials are a critical component to realize the strain-mediated multiferroic concept, and they are the focus of this dissertation. Various thin-film magnetoelastic materials having different key features have been investigated to satisfy different requirements of multiferroic devices.

In Chapter 2, the high-quality polycrystalline Terfenol-D films, showing the highest magnetostriction at room temperature, are fabricated by optimizing the deposition conditions. The elemental magnetic moments of the Terfenol-D films are investigated by using X-ray magnetic circular dichroism technique. The spin and orbital moments of each element are separated by sum

rule analysis. The correlation between the elements' orbital moments and crystalline anisotropy of the films is figured out as a function of temperature. The large difference of the orbital moments between Dy and Tb is partly responsible for enhanced crystalline anisotropy of Terfenol-D films at low temperatures.

Chapter 3 focuses on amorphous magnetoelastic TbFe films representing exchange spring magnetic (ESM) behavior. The ESM TbFe films are enabled by composition gradient formed through the film thickness. The gradient produces Tb and Fe-dominant regions, and their exchange coupling at the interface creates an ESM behavior. By applying a mechanical strain to the film, a two-step switching with a negative coercive field is both modulated and eliminated showing the promise of 180° switching. The modulation is caused by relatively higher magnetostriction coefficient in the Tb-dominant region compared to Fe-dominant producing larger changes in magnetic anisotropy as the strain is applied.

Chapter 4 presents the development of amorphous TbFe films having perpendicular magnetic anisotropy (PMA) and the correlations between process parameters, intermediate properties, and PMA. For this work, a wafer curvature technique is used to measure the residual stress of deposited films. From the correlations between parameters, it is turned out that both of residual film stress and atomic composition strongly impact on PMA property simultaneously.

The dissertation of Taehwan Lee is approved.

Dwight Christopher Streit

Christopher S. Lynch

Gregory P. Carman, Committee Chair

University of California, Los Angeles

2019

This dissertation is dedicated to my wife who is my timeless Ally.

Contents

Novel Magnetoelastic Materials for Multiferroic Applications

List of Figures

Acknowledgments

I would first like to thank my academic advisor, Prof. Greg Carman for his consistent caring and giving me great inspiration. He always appreciates my potential values, which makes me have confidence in what I think and know. Also, I was able to have tons of opportunities thanks to him including collaborations, cutting-edge facilities, project proposals, and presentations. I have been truly inspired by his enthusiasm and positive vibe.

I would also like to express my gratitude to my committee members, Profs. Chris Lynch, Dwight Streit, and Yong Chen. From the qualifying exam in my 2nd year to the final defense in my 6th year, they kindly served as my committee members and gave me big encouragements and advice to successfully finish my research works. My big thanks should also go to Dr. Mohanchandra. My research is initially motivated by his results and I would not be able to pave a path without your help and discussion.

I was so lucky to get into the Active Materials Lab. (AML) and meet amazing lab-mates. I would like to give my appreciation to all the past and current AML members who make a super-friendly and collaborative lab atmosphere. In particular, thanks to Tony for having a mind-breaking discussion and showing a positive mindset. I will not forget the nights we spent on the XMCD measurements and the chats we had all night. I appreciate Andres, Auni, and Devin for having coffee breaks together and encouraging me when I am down. I also have received big help from past AML members. Hyung Suk kindly introduced me to this fascinating lab and Prof. Carman. Paul helped me settle down into the lab by guiding me to write the first proposal and teaching me magnetic measurement tools, MOKE and SQUID. Kyle gave me deep insights about magnetic materials and multiferroics at the group meeting or lab discussions. Scott Strutner, a great partner in the NASA project, showed me his enthusiasm in the project and made the project move forward with me. Cheng-Yen always made all the lab members smile and personally encouraged me. Cai always cared for every lab works, which might be bothering him.

The research works have been able to be done with lots of help from outside the lab. Alpha N'Diaye in Lawrence Berkeley National Lab. gave me a great opportunity for the XMCD measurement and guided me to operate them by myself. Ignacio Martini taught me to use SQUID and helped me to troubleshoot the issues in it. Kin Wong trained me to use MOKE system and always let me in the MOKE room for convenient usage. Hoc Ngo helped me to use the sputtering tool in the Nanolab. He has been helpful to me even for quite difficult requests. Tony Wright also kindly trained me to use the sputtering in ISNC. Derek Stewart in Western Digital gave me valuable inputs on the principle calculation corresponding to my experimental works. Steven Bennett provided high-quality crystalline samples for collaborative work. Chang Wan from Purdue University (now in Intel) kindly characterized my sample on the Titan TEM in his lab. Sergey Prikhodko also trained me to use SEM and investigated my samples on TEM.

A number of funding sources enabled my research works and Ph.D. life. I appreciate the NASA project and TANMS engineering research center. I was able to have an opportunity for teaching as a TA. Prof. Sepulveda first gave me a chance for TA in his composite materials course. Prof. Carman recommended me as a TA of the TANMS online multiferroic course. I also thank the Graduate Division for giving me an award of the Dissertation Year Fellowship. Along with the funding itself, many administrative staffs helped me receive the funds and get the degree done. Thanks to Lili Bulhoes in MSE, Evgenia Grigorova in MAE, and Tsai-Tsai & Michelle in TANMS.

My sincere friends in MSE have been my reliable supporters. At the first year, I and my batches, Hyunpil, Sanghoon, and Jaesung helped each other to go through the tight coursework series and pass the preliminary exam. Jin Hee, Hyung Suk, and You Seung also provided lots of help about classes, research, and how to survive here.

Finally, I am really grateful to my family and parents. My wife, Jiyoon (Ally) has unconditionally supported me with sacrificing her career. I should pay back to her until the end of my life. I want to thank my daughter, Sia (Stella) for existing, eating, sleeping, smiling, and growing. I really appreciate parents and parents-in-law for their supports even in that they cannot see their son and daughter. I believe I could not have done this without their prayer. I also truly thank my siblings: Sujin, Jongpil, and Sohyung, and sister-in-law, Jisoo for taking over our role as children supposed to be next to our parents.

VITA

Education:

Korea University Seoul, South Korea │ February 2009
Master of Engineering, *Materials Science and Engineering*, GPA: 3.83/4.00
"Electrical spin injection in epitaxial ferromagnet/semiconductor hybrid structures"

Korea University Seoul, South Korea │ February 2007
Bachelor of Engineering, *Materials Science and Engineering*, GPA: 3.70/4.00

Professional Employment:

Samsung Electronics Yongin, South Korea │ Feb. 2009 – Feb. 2012
Device & Integration Engineer, *Foundry Business, Semiconductor Division*

Publications:

1. T. Lee, M. K. Panduranga, A. T. N'Diaye, A. Barra, and G. P. Carman, "Elemental orbital/ spin angular magnetic moment measurement of magnetostrictive $Tb_{0.3}Dy_{0.7}Fe_2$ film", ***In preparation***

2. I. J. Park, T. Lee, P. Das, B. Debnath, G. P. Carman, and R. K. Lake, "A first principles study: Strain control of the Neel vector in L10-type Mn-based antiferromagnetic materials", ***Under Review in Applied Physics Letters***

3. K. P. Mohanchandra, T. Lee, S. V. Prikhodko, and G. P. Carman, "Polycrystalline Terfenol-D Thin Films Grown at CMOS Compatible Temperature", ***AIP Advances***, **8**, 056404 **(2018)**

4. T. Lee, M. K. Panduranga, C. W. Han, V. Ortalan, and G. P. Carman, "Strain-modulated exchange spring magnetic behavior in TbFe Thin Films", ***Physical Review Applied***, **8**, 024024 **(2017)**

5. S. M. Choi, T. Lee, C. S. Yang, K. H. Shin, and S. H. Lim, "Effects of lateral dimensions of the magnetic thin films on the characteristics of thin-film type orthogonal fluxgate sensors", ***Thin Solid Films***, **565**, 271 **(2014)**

6. T. H. Lee, H. C. Koo, H. J. Kim, S. H. Han, and S. H. Lim, "Crystalline anisotropy effect on magnetic properties and its competition with shape anisotropy", ***Metals and Materials International***, **17**(3), 509 **(2011)**

7. T. H. Lee, H. C. Koo, K. H. Kim, H. J. Kim, J. Y. Chang, S. H. Han, J. K. Hong, and S. H. Lim, "Temperature dependence of spin injection efficiency in an epitaxially grown Fe/GaAs hybrid structure", ***Journal of Magnetism and Magnetic Materials***, **321**(22), 3795 **(2009)**

8. T. H. Lee and S. H. Lim, "Design optimization of the bit and word lines in magnetic random access memory in the Stoner-Wohlfarth model", ***Physica Status Solidi (c)***, **4**(12), 4341 **(2007)**

1. Introduction

1.1 Motivation

Nowadays, people rely on multiple mobile devices like a smart phone, tablet pc, and smart watch to perform computational operations. This reliance also yields frustration when one of the devices' battery begins to run out. One of the primary causes of this energy consumption in the device is leakage current reportedly responsible for almost 70 % of the energy consumption of the chips inside our cell phones [1]. In order to reduce this waste of energy and preserve battery power, individuals have proposed magnetic random-access memory (MRAM) which is being researched, and currently being manufactured. In the early stages of MRAM development, they used local magnetic fields generated by a current-carrying conducting wire to switch the magnetic memory cell. While successfully writing the bit, there are a number of problems associated with this writing concept in micro/nanoscale devices. For example, the resistive energy loss from the current-carrying wires is significant in small scale devices presenting a problem where energy efficiency represents one of the key issues. While a number of researchers have investigated approaches to reduce the required magnetic switching field with maintaining the thermal stability by optimizing the cell design [2-4], all of these still suffered from resistive loss due to the electrical current in the wires. Therefore, a new efficient approach is needed to realize MRAM devices at small scales.

One approach that has been considered uses Spin Transfer Torque (STT) rather than Ampere field from electrical current [5-7]. In the STT mechanism, highly spin-polarized currents are passed through a magnetic tunneling junction (MTJ) to switch the magnetic moment of the free layer. Here the spin-polarized current flips the magnetic moment rather than an Oersted magnetic field. However, even the STT switching mechanism produces energy-related problems due to the high writing current required for switching the magnetic cells. These high switching currents result in both large cell areas due to the large width of access transistors, limiting the areal density, as well as large energy inefficiencies or dissipation (~100 fJ/bit) [8]. Therefore, while the STT approach is beneficial it does not reduce the energy dissipation to an acceptable level.

More recently researchers have explored voltage actuated strain-mediated multiferroics to reduce the writing energy or energy dissipations. The strain-mediated multiferroic concept uses a voltage to switch magnetic cells instead of an electrical current to significantly reduce the writing energy [8,9]. The word ‘multiferroics’ refers to a material or structure exhibiting more than one ferroic order parameter simultaneously among the ferromagnetism, ferroelectricity, or ferroelasticity. In this dissertation, the focus is on the class of multiferroics comprised of a ferroelectric (piezoelectric) with a ferromagnetic material (magnetoelastic). In this strain-coupled multiferroic system, the applied voltage (electric field) on the ferroelectric creates a strain (piezoelectric effect) that is transferred into the attached ferromagnetic layer. The strain on the ferromagnetic layer is converted into a magnetization change due to its magnetoelastic property.

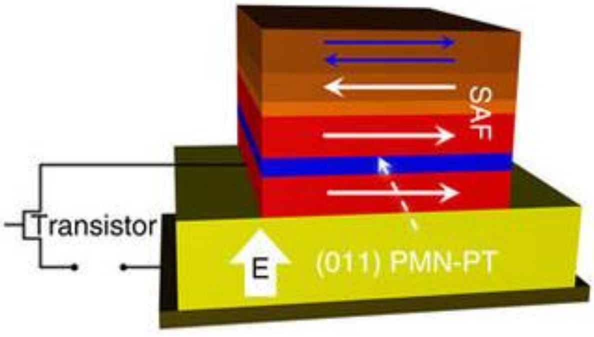

Figure 1.1. Schematic of strain-mediated magnetic random access memory (MRAM).

Figure 1.1 shows a schematic structure of the strain-mediated MRAM cell. When a voltage is applied, the magnetic free layer (red, bottom) is controlled by the induced strain signal from the ferroelectric/ piezoelectric PMN-PT layer. This particular strain-mediated multiferroic memory cell suggests a writing energy efficiency improvement by 6 orders of magnitude compared to a conventional DRAM cell (1 pJ/bit → 1 aJ/bit) [10].

The strain-mediated multiferroics application fields are not limited to only memory devices. Many kinds of electromagnetic devices can be created or improved from conventional versions including a nanomotor, energy-efficient antenna, and magnetic sensor as shown in Fig. 1.2 [9,11-14]. All of these examples shown in Fig 1.2 use the magnetoelastic material as a critical component enabling device operation. Specifically, a substantial amount of research has been devoted to small scale ferroelectrics/ piezoelectrics, however, very little research has been conducted on a small scale (micron) magnetoelastic materials. Therefore, this dissertation focuses on developing high-quality and functional magnetoelastic materials by studying the underlying mechanisms coupling magnetism to strain. In the next few sections, I start with an overview of the multiferroics and how the strain-mediated multiferroics operate. This section is followed by a fundamental of magnetic anisotropy and how it influences on operational concepts. Finally, this background section reviews magnetostriction in the context of magnetoelastic anisotropy.

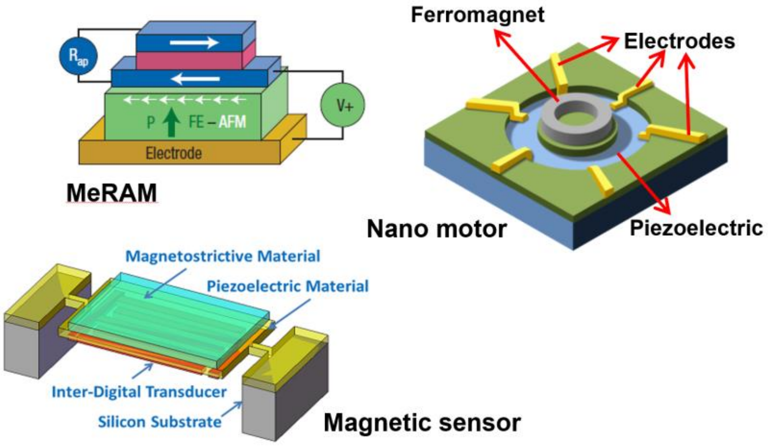

Figure 1.2. Potential application fields of strain-mediated multiferroics

1.2 Background

1.2.1 Multiferroics

Multiferroics is defined as a class of materials or structures, in which at least two order states such as magnetic, electric, or elastic phases coexist. Figure 1.3 graphically represents three ferroic order states and possible multiferroic cross-coupling cases. Well-known couplings such as piezo-electricity and magneto-elasticity are important for technological applications because they facilitate direct control of ferromagnetic and ferroelectric properties via externally applied mechanical strain.

There are two additional multiferroic possible states, each displaying cross-couplings between the order states: (i) magneto-electric multiferroic, in which the electric and magnetic order states coexist; and (ii) elasto-magneto-electric multiferroic, in which all three order states are present. The direct magneto-electric coupling refers to multiferroics in which the application of electric or magnetic field results in changes of magnetization or electric polarization of the system, respectively. The representative example of this coupling is a “single-phase” multiferroics. A second mechanism of activating the magneto-electric effect occurs primarily in elasto-magneto-electric multiferroics, also known as composite multiferroics, and it is called the indirect magneto-electric effect. In this case, the application of a magnetic or electric field does not affect directly the electric polarization or magnetization, respectively. Instead, they are modified indirectly via a strain-mediated magneto-electric coupling [15].

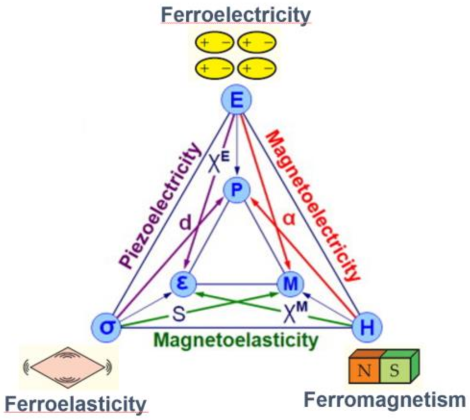

Figure 1.3. Possible cross-couplings in multiferroics. E – electric field; P – electric polarization; σ – applied mechanical stress; Ɛ – strain; H – magnetic field; M – magnetization.

Single-phase multiferroic materials display both ferroelectric and ferromagnetic properties simultaneously in homogeneous compounds at any point within the material. Since one of the ferroic components is the electrically ordered phase, which requires dielectric materials, unsurprisingly all single-phase multiferroic materials are dielectric oxides. However, single-phase multiferroics rarely occur in nature. The reasons behind the scarcity of single-phase are linked to symmetry restrictions since only 13-point groups out of a total of 122 possible crystallographic point groups accept multiferroic state.

The only room temperature single-phase multiferroic material is $BiFeO_3$, usually called BFO. This material has perovskite crystal structure, and both properties of antiferromagnet and ferroelectric. This antiferromagnet material can have ferromagnetic property by the Dzyaloshinskii–Moriya (DM) interaction, which can make a canting of the antiferromagnetically aligned spins. As a result, only weak ferromagnetism is generated in the material. The directions of polarization and weak magnetization are coupled to each other and this coupling produces the reorientation of one order as the other order is manipulated with an applied field.

The mechanism producing the weak ferromagnetism is explained in Fig. 1.4. Usual antiferromagnetic materials have magnetic configuration similar to the illustration shown in Fig. 1.4(a), i.e. zero net magnetic moment. Note that the oxygen atom is paramagnetic, but that can be schematically represented as the opposite direction half-spins. As a result, Fe moments form exchange coupling with the half spins of the oxygen atom, resulting in the overall oxygen ion-mediated antiferromagnetic coupling. When an electric field is applied and an electrical polarization is induced, the oxygen atomic displacement from Fe-Fe bonding line appears and the corresponding DM vector is generated as shown in Fig. 1.4(b). This DM vector causes the antiferromagnetically aligned Fe spins to cant producing weak ferromagnetism along the perpendicular direction to the polarization direction. To sum up, a polarization generates a DM vector, and this DM vector, in turn, induces a weak net magnetization.

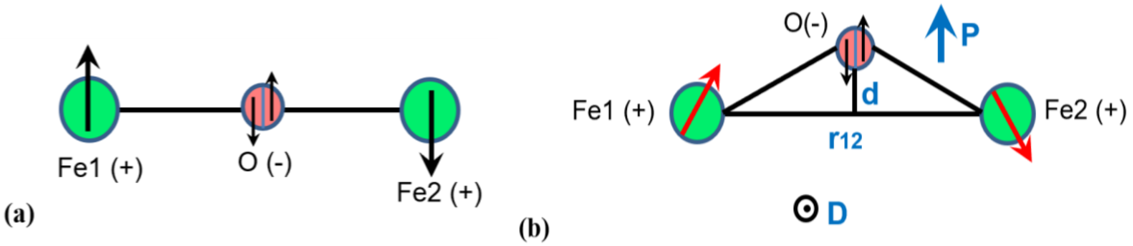

Figure 1.4. Schematic explanation of DM interaction. (a) Atomic magnetic moment configuration of usual antiferromagnet materials with no net magnetization. (b) After electric polarization, oxygen displacement vector (d) induces DM vector (D), resulting in the canting of antiferromagnetically aligned spins.

While single-phase multiferroics can have both ferroic- order parameters, the weak ferromagnetism, and magneto-electric coupling limit their applicability in many devices. To tackle this limitation of weak ferromagnetism, the single-phase multiferroic material (BFO) has been coupled with the ferromagnetic layer (CoFe) to enhance the magnetic coupling effect [16]. While beneficial, the coupling coefficient of these layered single phase material is still lower than that of other composite multiferroic structures. For example, strain-mediated multiferroics represent a composite structure consisting of magnetoelastic and piezoelectric materials combined. As schematically illustrated in Fig. 1.5, an applied *E*-field produces strain in piezoelectric material that can change the magnetization in piezomagnetic material [17]. These multiferroic composites are defined as compounds in which electric, magnetic, and piezo order states coexist within the material. The order phases are geometrically separated from each other within the multiferroic composite material as contrasted with the single-phase multiferroics where the states coexist at a point.

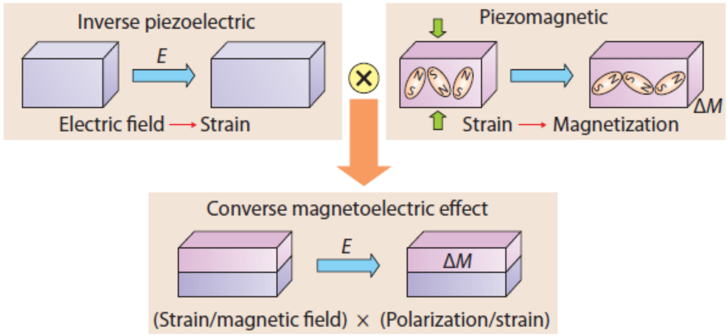

Figure 1.5. Schematic illustration of strain-mediated multifferoics. Piezoelectric and piezomagnetic materials can be combined as a composite to obtain the magnetoelectric effect.

The general idea of fabricating multiferroic composites offers substantial advantages including greater flexibility in designing the materials for specific applications and optimization of the magneto-electric coupling. Finally, the magneto-electric coupling effects measured in the strain-mediated composite multiferroics are a few orders of magnitude larger than those of single-phase multiferroics. Also, most composite multiferroics operate at or above room temperature [15] which is in sharp contrast to many of the single-phase multiferroics which are limited to cryogenic temperatures.

Among the extensive research works on the strain-mediated multiferroics, I will introduce several key results here. In 2001, J. Ryu et. al. firstly fabricated a Terfenol-D/ PZT laminate composite to demonstrate the sensing of magnetic fields, i.e. an applied magnetic field creates a voltage [18]. PZT disks were prepared by the conventional ceramic process. Electrodes are deposited on the machined PZT disks by gold sputtering and electrically polarized under the electric field of 3 kV/mm. Terfenol-D disks were also machined to a dimension of φ12.7 × 1 mm. PZT and Terfenol-D disks were bonded using silver epoxy. Figure 1.6(a) shows the schematic structure of a laminar composite sample and (b) is a photograph of the assembled devices. The magnetoelectric voltage coefficient, dE/dH, increased with decreasing thickness and increasing piezoelectric voltage constant (g31) of the PZT layer. The highest magnetoelectric voltage coefficient of 4.68 V/cm·Oe at room temperature for the sample with high g33 PZT of 0.5 mm in thickness as shown in Fig. 1.6(c).

Figure 1.6. Magnetoelectric lamina composite using TERFENOL-D and PZT disks. (a) schematic structure, and (b) photograph of the device. (c) Magnetoelectric voltage coefficient as a function of applied d.c. magnetic bias with various thickness of PZT layer at 1 kHz [18].

In the following year, G. Srinivasan et. al. developed layered composites of ferromagnetic lanthanum manganites and piezoelectric PZT [19]. The samples were prepared from thick films obtained by “doctor blade” techniques. Fine powders of manganites were prepared by the standard ceramic technique. The sample synthesis involved the preparation of tapes of manganites and PZT, lamination, and final sintering. The best ME parameters were obtained at low temperatures for the bilayer sample. Figure 1.7 shows the H dependence of the transverse coefficient $\alpha_{E,zx}$ for a bilayer (n=2) of $La_{0.7}Sr_{0.3}MnO_3$-PZT. The data are for temperatures 120 and 300 K and for a frequency of 100 Hz for the ac magnetic field. Considering the data at 120 K, as H is increased from -500 Oe, $\alpha_{E,zx}$ increases in magnitude and peaks at -35 Oe. One observes a large remanence at H=0. In this research, thick-film bilayers of lanthanum strontium manganite-PZT prepared by tape-casting techniques show magnetoelectric effects as strong as in ferrite-PZT multilayer composites.

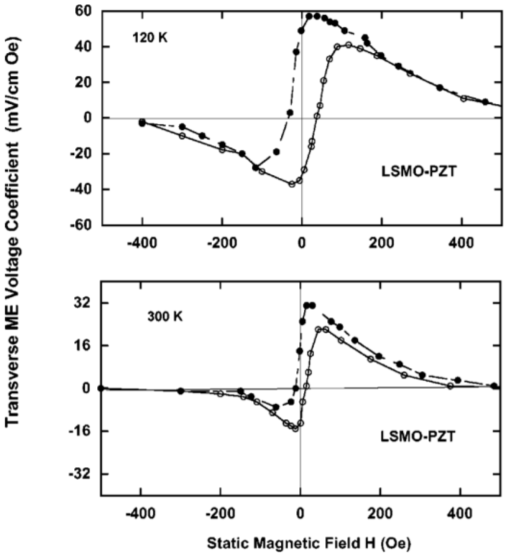

Figure 1.7. Transverse magnetoelectric (ME) voltage coefficient $\alpha_{E,zx} = \delta E_z/\delta H_x$ at 120 and 300 K as a function of static magnetic field H for a two-layer structure of LSMO and PZT [19].

In 2008, D. A. Pan et. al. fabricated Ni/PZT/Ni layered composite structure and tested the magnetoelectric (ME) effect with different lateral size, shape, and frequency [20]. The large PZT-5H piece was cut into rectangular smaller pieces 0.8 mm thick and polarized along the thickness direction at 425 K in an electric field of 30–50 kV/cm. Following poling, PZT samples were bathed in a nickel plating solution, and Ni was electrodeposited on both sides of the PZT samples for 8 h. The resulting total thickness of the two Ni layers was approximately 0.8 mm and the sample geometry is sketched in Fig. 1.8(a). The ME voltage coefficient is plotted in Fig. 1.8(b) as a function of the applied magnetic field frequency (f) for a Ni/PZT/Ni trilayered composite with dimensions of 16 × 25 × 1.6 mm^3. There are three resonant peaks at 67.2, 102 and 125 kHz in rectangular symmetric trilayered ME composites. The first resonance peak corresponds to the longitudinal mode along the diagonal direction in a rectangle and not to the bending resonant mode traditionally considered for bilayered structures. The diagonal resonant mode causes mutual weakening of the ME effect down to zero at the first resonant frequency for a square sample. Figure 1.8(c) plots ME voltage coefficients corresponding to the first and the third resonance peaks as a function of the sample width W with the constraint that the sample area remains constant, i.e. W × L = 400 mm^2. The ME voltage coefficient of layered ME composites scales with its in-plane dimensions.

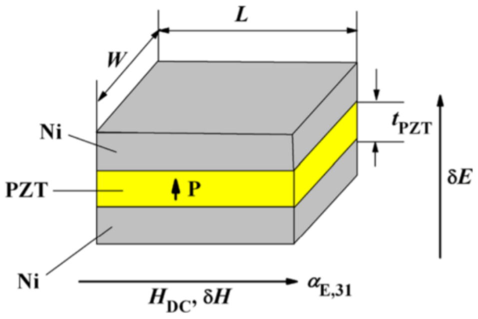

(a)

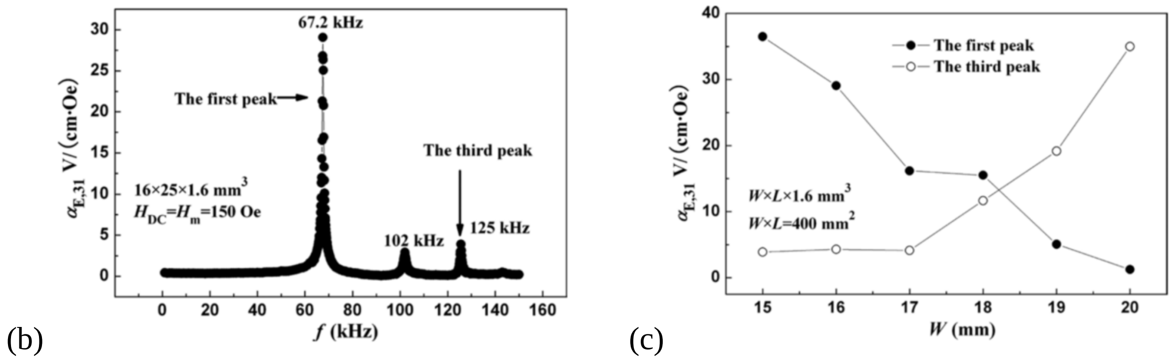

Figure 1.8. (a) Schematic of the trilayered composite structure geometry and the applied magnetic field. Vector P shows the PZT polarization direction. (b) The dependence of the ME voltage coefficient $\alpha_{E,31}$ on the frequency for the ME trilayered composite. (c) The dependence of the ME voltage coefficient on the width W of layered ME composites with the same interfacial area [20].

In 2013, researchers at UCLA (H. Kim et al.) successfully demonstrated a new kind of composite multiferroic structure of Ni nanoparticles and PMN-PT substrate [21]. In these tests, 16 nm diameter Ni magnetoelastic nanocrystals are mechanically coupled to (011) PMN-PT ferroelectric single crystal substrates. Magnetoelectric composites were produced by slowly evaporating a dilute solution of the Ni nanocrystals dissolved in hexane onto an unpoled PMN-PT substrate coated with a thin titanium adhesion layer. After nanocrystal deposition, the organic ligands on the particles were removed and without breaking vacuum, a 30 nm thick Pt layer was deposited onto the PMN-PT substrate to fully encase the Ni particles and protect them from oxidation as shown in the left panel of Fig. 1.9.

The M-H loops measured along x and y directions before (a, b) and after (c, d) applying electric fields are shown in the right panel of Fig. 1.9. Before applying electric fields, small coercive fields, Hc < 20 Oe, are observed in both directions indicating that the sample is both magnetically isotropic in-plane and dominantly superparamagnetic. After the sample has been poled ($\varepsilon x = -300$ με, $\varepsilon y = -1000$ με), a hard magnetic axis is created parallel to the x-direction.

The Mr/Ms ratio is very low, suggesting that domains tend to orient in an off-axis direction. In contrast, the poled sample shows that a magnetic easy axis is created along the y-direction. In this direction, Mr is approximately equal to Ms, indicating that the sample consists of essentially single domain Ni nanocrystals that are aligned along the y-axis. This result thus demonstrates that the application of an electric field stabilized the y-axis aligned spin state, resulting in a net magnetization equivalent to the saturation magnetization of Ni (i.e., 485 emu/cc) [21].

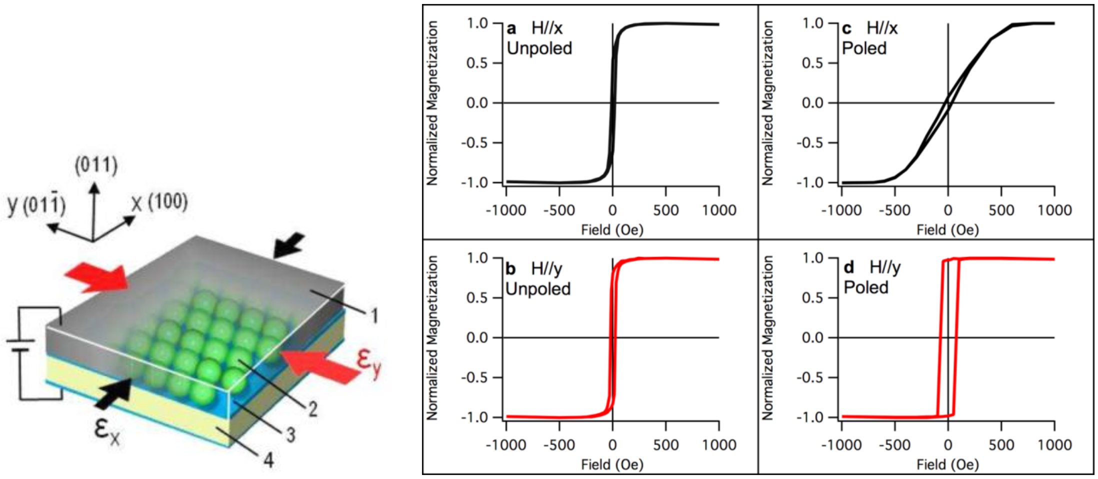

Figure 1.9. The schematic sample structure (left) and the measured results obtained from Ni/PMN-PT sample (right). (a, b) Before applying electric fields. (c, d) After applying electric field and poling the sample.

In the same year, J. Cui et al. showed that a patterned thin-film piezoelectric structure could be used for multiferroic magnetization switching [22] and overcome the substrate clamping problem. The patterned electrodes on a piezoelectric PZT substrate produced a localized strain of sufficient magnitude to control the magnetic anisotropy in the Ni elements. The configuration, shown in the left panel of Fig. 1.10, was fabricated on a polycrystalline plate of PZT. The electrode patterns and magnetic Ni islands were deposited on the PZT plates using a two-step optical mask lithography approach. Electrodes of 3 nm Ti (adhesion layer) and 100 nm Al were deposited by e-beam evaporation (CHA Solutions). 50 nm of SiO_2 was evaporated to create an insulating layer to reduce the likelihood of electric breakdown between the pads. Finally, a film of 3 nm Ti/35 nm Ni was deposited. The circular shape of the Ni was selected to minimize the effect of shape anisotropy. The induced localized strain around the corresponding electrodes (A-A or B-B) enabled the Ni islands to deterministically rotate 90°. When the PZT is poled with the selected in-plane electrodes, the induced strain signal can be concentrated on the electrode position, and the corresponding in-plane strain is conveyed to the magnetoelastic Ni islands. The experimental and simulation results in the right panel of Fig. 1.10 show this voltage induced magnetization change depending on the *E*-field applied.

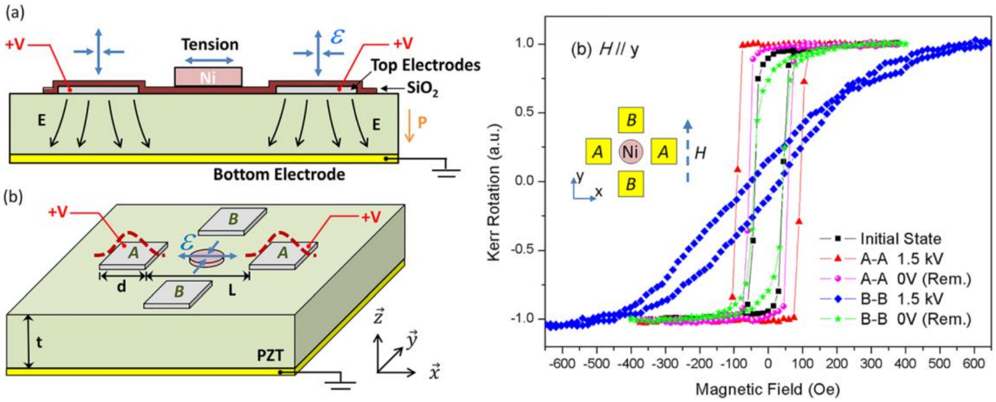

Figure 1.10. Strain-mediated multiferroic structure with the in-plane patterned electrodes (left) and their measured *M-H* loops with different poling states (right) [22].

1.2.2 Magnetic Anisotropy

Magnetic anisotropy is the directional dependence of a material's magnetic properties. Without a magnetic field applied to a magnetic material, the direction of magnetization prefers to point in a specific direction usually referred to as the easy axis. This magnetic anisotropy is one crucial component needed to be understood when working with strain-mediated multiferroics. This is because the strain signal impacts on the magnetic elements in the form of magnetic anisotropy, which can be combined with another kind of anisotropy resulting in showing more functionality [23,24]. The origin of the magnetic anisotropy can be classified by magnetocrystalline anisotropy, shape anisotropy, and magnetoelastic anisotropy. In the following paragraphs I start with magnetocrystalline anisotropy followed by shape anisotropy and finally conclude with mixed anisotropy. The specifics of induced magnetoelastic anisotropy will be described in the section following this one.

When magnetic properties depend on the crystal axis of the material, this is called magnetocrystalline anisotropy. The typical M-H curves measured in the plane of a disk-shaped Fe (body-centered cubic, BCC) along different crystal orientations are shown in Fig. 1.11. In the <100> direction, a magnetic saturation can be achieved with quite low fields, of the order of a few tens of Oe at most, which is called the “easy direction” of magnetization. For the <110> and <111> directions, on the other hand, almost 500 Oe magnetic field is required to make the specimen saturated, which indicates the “hard direction” of the material.

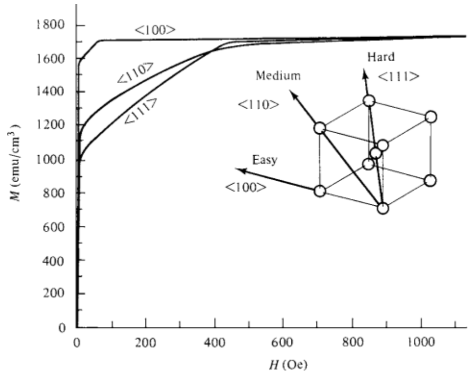

Figure 1.11. Magnetization curves for single crystals of iron [25].

The Crystalline anisotropy can be regarded as a force which tends to hold the magnetization in certain equivalent crystallographic directions (easy axis). Because the applied field must work against the anisotropy force to turn the magnetization vector away from an easy direction, there should be some energy stored in any non-easy direction. This is called the crystalline anisotropy energy E. In a cubic crystal, let the saturation magnetization Ms make angles a, b, c with the crystal axes, and let a1, a2, a3 be the cosines of these angles, which are called direction cosines. Then the energy in the system can be represented by

$$E = K_0 + K_1({\alpha_1}^2{\alpha_2}^2 + {\alpha_2}^2{\alpha_3}^2 + {\alpha_3}^2{\alpha_1}^2) + K_2({\alpha_1}^2{\alpha_2}^2{\alpha_3}^2) + \cdots$$

where K_0, K_1, K_2, . . . are anisotropy constants for specific materials and are expressed in erg/cm^3 (cgs) or J/m^3 (SI). Higher powers are generally not needed, and sometimes K_2 is so small that the term can be neglected.

The crystalline anisotropy of Fe is a typical example of cubic crystals. The other type of magnetocrystalline anisotropy appears in the hexagonal close-packed (HCP) structure. The typical example of crystalline anisotropy for the HCP structure is represented in Fig. 1.12. Magnetization curves of HCP Co along different crystal orientations are shown. The hexagonal c axis is the direction of easy magnetization, and, within the accuracy of the measurements, all directions in the basal plane are found to be equally hard. Under these circumstances, the anisotropy energy E depends on only a single angle, the angle ɵ between the Ms vector and the c axis, and the anisotropy can be described as a uniaxial anisotropy along the c axis. Therefore, the energy is expressed as

$$E = K_0' + K_1' cos^2\theta + K_2' cos^4\theta + \cdots$$

However, it is usual to write the equation for E in uniaxial crystals in powers of sin ɵ. Putting $\cos^2$ ɵ = 1- $\sin^2$ ɵ into the equation, we have

$$E = K_0 + K_1 sin^2\theta + K_2 sin^4\theta + \cdots$$

When K_1 and K_2 are both positive, the energy E is minimum for ɵ = 0, and the c-axis is an axis of easy magnetization. A crystal with a single easy axis, along which the magnetization can point either up or down, is referred to as a uniaxial crystal. Its domain structure in the demagnetized state is particularly simple. Elemental cobalt, barium ferrite, and many rare earth-transition metal intermetallic compounds behave in this way.

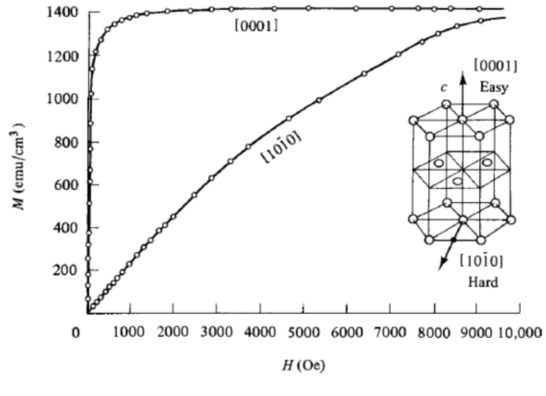

Figure 1.12. Magnetization curves for a single crystal of cobalt.

This crystalline anisotropy is mainly due to spin-orbit coupling. A coupling means a kind of interaction. We can speak of the exchange interaction between two neighboring spins as a spin-spin coupling. This coupling can be very strong and acts to keep neighboring spins parallel or antiparallel to one another. But the associated exchange energy is isotropic. So, the spin-spin coupling cannot contribute to the crystalline anisotropy. The orbit-lattice coupling is also strong. This means that the orientations of the orbits are fixed very strongly to the lattice, and so even large fields cannot change them.

There is also a coupling between the spin and the orbital motion of each electron. When an external field tries to reorient the spin of an electron, the orbit of that electron also tends to be reoriented. But the orbit is strongly coupled to the lattice and therefore resists the attempt to rotate the spin axis. The energy required to rotate the spin system of a domain away from the easy direction, which we call the anisotropy energy, is just the energy required to overcome the spin-orbit coupling. This coupling is relatively weak because fields of a few hundred Oe or a few tens of kA/m are usually sufficient to rotate the spins. Inasmuch as the "lattice" consists of a number of atomic nuclei arranged in space, each with its surrounding cloud of orbital electrons, we can also speak of spin-lattice coupling and conclude that it too is weak. These relationships are depicted in Fig. 1.13.

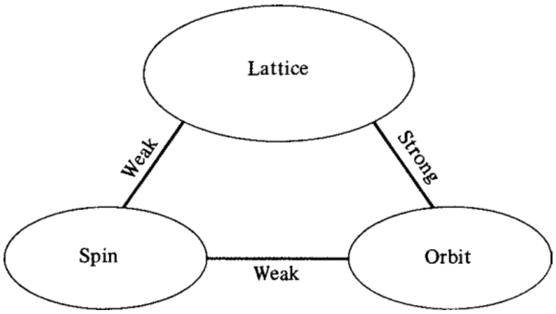

Figure 1.13. Spin–lattice–orbit interactions.

Consider a polycrystalline specimen having no preferred orientation of its grains, and therefore no net crystalline anisotropy. If it is spherical in shape, the same applied field will magnetize to the same extent in any direction. But if it is non-spherical, it will be easier to be magnetized along a long axis than a short axis. The reason for this is that the demagnetizing field along a short axis is stronger than a long axis. The applied field along a short axis then should be stronger to produce the same true field inside the specimen. Thus, the shape of the specimen alone can be a source of magnetic anisotropy, and this is called a shape anisotropy.

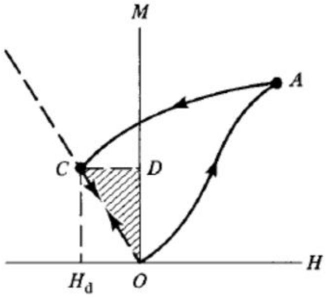

Figure 1.14. Magnetostatic energy of a magnetized body in zero applied field.

In order to treat shape anisotropy quantitatively, we need an expression for the magnetostatic energy E_{ms} of a magnetized body in zero applied field. If a body is magnetized by an applied field to some level A (see Fig. 1.14) and the applied field is then removed, the magnetization will decrease to C under the action of the demagnetizing field H_d, which depends on the specimen's shape and the measured magnetization direction. Here OC is the demagnetizing-field line, with a slope of $-1/N_d$, where N_d is the demagnetizing coefficient. The specimen then contains stored energy E_{ms} equal to the area of the shaded triangle OCD. This energy is associated with the demagnetizing field of the specimen and called magnetostatic energy. This energy is represented as a vector form of the area of the triangle OCD in Fig. 1.14:

$$E_{ms} = -\frac{1}{2} H_d \cdot M$$

because H_d is antiparallel to M.

This equation can be written in terms of N_d, by the substitution $H_d = N_d M$:

$$E_{ms} = \frac{1}{2} N_d M^2 \; erg/cm^3 \; (cgs) \qquad\qquad E_{ms} = \frac{1}{2} \mu_0 N_d M^2 \; J/m^3 \; (SI)$$

We now consider a specimen in the shape of a prolate spheroid (rod) with semi-major axis c and semi-minor axes a of equal length (see Fig. 1.15). Let it be magnetized to a value M at an angle ө to c. Then, taking components of M parallel and perpendicular to c, we have

$$E_{ms} = \frac{1}{2}[(Mcos\theta)^2 N_C + (Msin\theta)^2 N_a]$$

, where N_c and N_a are demagnetizing coefficients along c and a, respectively. Substituting $\cos^2$ ө = 1 - $\sin^2$ ө, we find

$$E_{ms} = \frac{1}{2} M^2 N_c + \frac{1}{2}(N_a - N_c) M^2 sin^2\theta$$

This expression for the magnetostatic energy has an angle-dependent term of the exact same form as uniaxial crystalline anisotropy energy. The long axis of the specimen plays the same role as the easy axis of the crystal, and the shape-anisotropy constant K_S is given by

$$K_S = \frac{1}{2}(N_a - N_c) M^2 \; erg/cm^3 \; (cgs) \qquad\qquad K_S = \frac{1}{2}\mu_0 (N_a - N_c) M^2 \; J/m^3 \; (SI)$$

Magnetization is easy along the c-axis and equally hard along the axis normal to c. If c shrinks until it equals a, the specimen becomes spherical, $N_a = N_c$, $K_S = 0$, and shape anisotropy disappear.

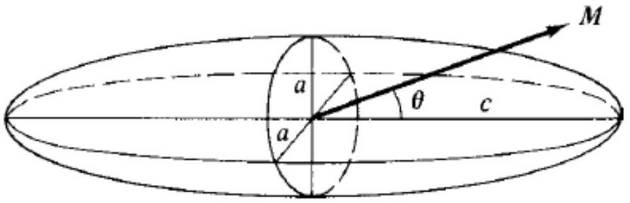

Figure 1.15. Prolate ellipsoid.

As the above equation shows, the "strength" of shape anisotropy depends both on the axial ratio c/a of the specimen, which determines (Na–Nc), and on the magnitude of the magnetization M. To numerically illustrate the demagnetization factor dependence, we put M = 1422 emu/cm^3, which is the room-temperature saturation magnetization of uniaxial Co and calculate the value of the shape-anisotropy constant K_S as a function of c/a for a prolate spheroid of polycrystalline Co with no preferred orientation [26]. Figure 1.16 shows the results and at an axial ratio of about c/a = 3.5, K_S is about 45×10^5 erg/cm^3, which is equal to the value of the first crystal-anisotropy constant K_1 of crystalline HCP Co. In other words, neglecting K_2, we can say that a prolate spheroid of saturated Co, with axial ratio 3.5 and without any crystal anisotropy, would show the same uniaxial anisotropy as a spherical cobalt crystal with its normal crystal anisotropy.

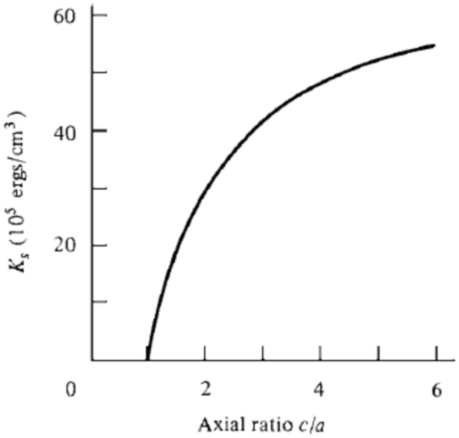

Figure 1.16. Shape anisotropy constant vs axial ratio of a prolate spheroid. Numerical values calculated for cobalt (M_S = 1422 emu/cm^3).

The previous paragraph suggests a more practical situation, in which two anisotropies of different physical origin are present together (i.e. magnetocrystalline anisotropy and shape anisotropy). The discussion will be limited to uniaxial anisotropies. For example, we might have a rod-shaped crystal of a uniaxial substance like Co, with its easy crystal axis at right angles to the rod axis. Will it be easier to magnetize along the rod axis, as dictated by shape anisotropy, or at right angles to the rod axis, as dictated by crystal anisotropy? Both anisotropy energies are given, except for constant terms, by expressions of the form: energy = (constant)·$\sin^2$(angle between M and easy axis). The problem is generalized in Fig. 1.17, where AA represents one easy axis and BB the other. The separate anisotropy energies, distinguished by subscripts, are

$$E_A = K_A sin^2\theta,$$
$$E_B = K_B sin^2(90^{\circ} - \theta)$$

So, the total energy is

$$E = K_A sin^2\theta + K_B cos^2\theta = K_B + (K_A - K_B) sin^2\theta$$

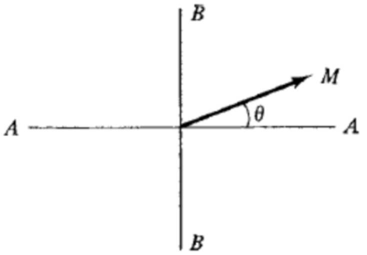

Figure 1.17. Mixed anisotropy.

If the two anisotropies are of equal strength ($K_A = K_B$), then E is independent of angle and there is no anisotropy. (Thus, two equal uniaxial anisotropies at right angles are not equivalent to biaxial anisotropy.) If they are not equal, we want the value of θ for which E is a minimum:

$$\frac{dE}{d\theta} = (K_A - K_B) sin2\theta = 0$$

The solutions are $\theta = 0$ and θ = 90°. To find whether they are minima or maxima, we take the second derivative,

$$\frac{d^2E}{d\theta^2} = 2(K_A - K_B) cos2\theta$$

, which must be positive for a minimum. Therefore, $\theta = 0$ is a minimum energy position if $K_A > K_B$, and $\theta = 90°$ if $K_A < K_B$. The direction of easiest magnetization is not, as might be expected, along with some axis lying between AA and BB. The easy direction is along AA if the A anisotropy is stronger, and along BB if B is stronger. The basic reason for this behavior is that a uniaxial anisotropy exerts no torque on M when M is at 90° to the uniaxial axis. If the two easy axes of Fig. 1.17 are at some angle a to each other, rather than at right angles, they will be together equivalent to a new uniaxial axis CC, which either (a) lies midway between AA and BB, if $K_A = K_B$, and has a strength of $K_C = K_A = K_B$, or (b) lies closer to AA, if $K_A > K_B$, and has a strength $K_C > K_A$.

Since nowadays most spintronic devices require thin-film type magnetic electrodes with a rectangular shape cross-section [27], the calculation effort on the mixed anisotropy situation is performed for the rectangular thin-film patterns by T. Lee et al. [23]. Here, the magnetization states as functions of the pattern dimensions and crystalline anisotropy constants during the magnetization reversal process are systematically calculated. The observations of remanent states provide information about the magnetic easy axis. Material parameters and dimensions were inserted, and the iteration of solving the Landau-Lifshitz equation was performed.

When the angle between crystalline and shape easy axes is 90°, the combined anisotropy effect is observed through the magnetization behavior. Figure 1.18(a, b) shows the demagnetizing dynamics of the patterns, whose shape and crystalline anisotropies compete. By definition, when the saturation field is removed, the magnetization vector indicates the closest easy axis. In the saturation state ($t = t_S$), the amplitudes of M_x and M_y are identical. After removing the field, the magnetization vectors show that the shape anisotropy is more dominant in the initial stage ($t = t_1$).

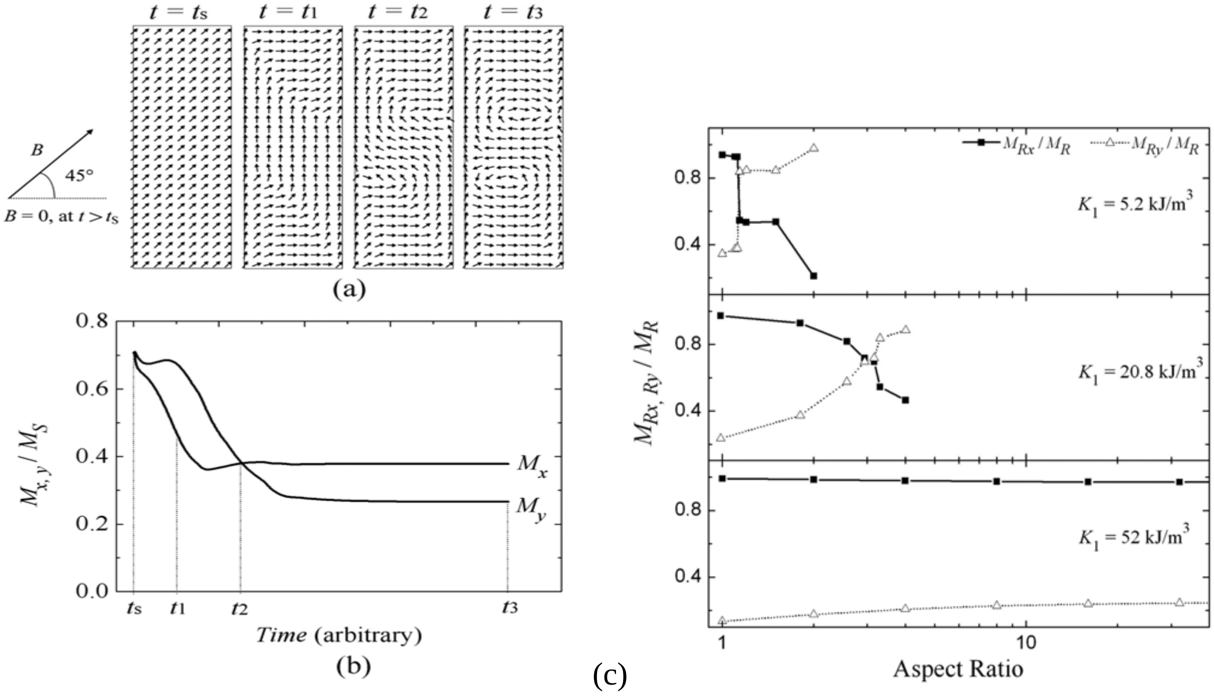

Figure 1.18. (a, b) Remanence dynamics after magnetization saturation along the 45° of shape and crystalline easy axes. (c) Observation of easy axis after applying diagonal direction field. These graphs present aspect ratio dependence of M_{Rx}/M_R and M_{Ry}/M_R for various crystalline anisotropy constant (K_1) [23]

The competition behavior between the crystalline and shape anisotropies can be shown by the critical aspect ratio (R_{CR}), which is the aspect ratio required to offset the crystalline anisotropy. To determine the critical aspect ratio, the relative remanent magnetizations for the easy axes of the shape and crystalline anisotropy, i.e., M_{Rx}/M_R and M_{Ry}/M_R, are compared in Fig. 1.18(c). The film thickness is 20 nm and the width (x) is 1 μm. To implement the required lateral aspect ratio, the length (y) was adjusted in this case. As shown in the top panel of Fig. 1.18(c), only a small aspect ratio ($R_{CR} = 1.13$) is enough to overcome the crystalline anisotropy when K_1 equals 5.2 kJ/m^3. As the K_1 increases, a greater aspect ratio is necessary to offset the crystalline anisotropy. When $K_1 =$ 20.8 kJ/m^3, the critical aspect ratio is 3.7. If K_1 is larger, the shape anisotropy scarcely overcomes the crystalline anisotropy. When K_1 = 52 kJ/m^3, M_x is nearly equal to M_R, even when the aspect ratio exceeds 32. To sum up, crystalline and shape anisotropy constants can be combined when their easy axes are parallel or perpendicular to each other. The crystalline anisotropy is compensated by the critical aspect ratio which increases with the crystalline anisotropy constant.

1.2.3 Magnetostriction (Magnetoelastic Anisotropy)

In addition to the magnetic anisotropies introduced so far, a magnetoelastic anisotropy (magnetostriction) is a critical one associated with strain-mediated multiferroics. In magnetoelastic/magnetostrictive samples exposed to a magnetic field, the material's physical dimensions change. This change effect is called magnetostriction. It was discovered in 1842 by Joule, who showed that an iron rod increased in length when it was magnetized lengthwise by a weak field [28]. The fractional change in length $\Delta l / l$ is simply a strain, and to distinguish it from the strain Ɛ caused by an applied stress, people usually use a special symbol λ for the magnetically induced strain:

$$\lambda = \frac{\Delta l}{l}$$

The value of λ measured at magnetic saturation is called the saturation magnetostriction λ_S, and when the word "magnetostriction" is used without qualification, λ_S is usually implied.

Although the direct magnetostrictive effect is small in many materials, and not usually important by itself, there exists an inverse effect which causes such properties as permeability and the size and shape of the hysteresis loop to be strongly dependent on stress in many materials. Magnetostriction, therefore, has many practical consequences, and a great deal of research has accordingly been devoted to it.

The value of the saturation longitudinal magnetostriction λ_S can be positive, negative, or, in some alloys at some temperatures, zero. The value of λ depends on the extent of magnetization and hence on the applied field, and Fig. 1.19 shows how λ typically varies with H for a substance with positive magnetostriction. The process of magnetization occurs by two mechanisms, domainwall motion, and domain rotation. Most of the magnetostrictive change in length usually occurs during domain rotation.

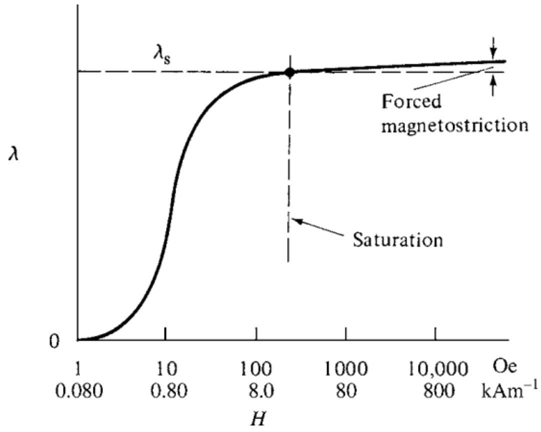

Figure 1.19. Dependence of magnetostriction on magnetic field (schematic).

The measurement of longitudinal magnetostriction is straightforward but non-trivial, especially over a range of temperatures. While early investigators used mechanical and optical levers to magnify the magnetostrictive strain to an observable magnitude, today the measurement on bulk samples is commonly made with an electrical-resistance strain gage cemented to the specimen. When the sample changes shape, so does the grid, and the change in shape causes a change in the electrical resistance of the gage. Thin film samples present special challenges in the measurement of magnetostriction since the films are almost always bonded to a nonmagnetic substrate. If the substrate is thin enough, a change in dimension of the magnetostrictive film may produce a measurable curvature in the substrate, from which the magnetostrictive strain can be deduced. Another approach is to apply known stress to the sample and measure the resulting change in magnetic anisotropy. This method makes use of the concept of the magnetoelastic anisotropy, as described later in this chapter.

Magnetostriction is mainly due to spin-orbit coupling. This coupling is also responsible for crystalline anisotropy as discussed in the previous chapter. It is relatively weak because applied fields of a few hundred Oe usually suffice to rotate the spins away from the easy direction. The relation between magnetostriction and spin-orbit coupling can be crudely pictured in Fig. 1.20, which is a section through a row of atoms in a crystal. The black dots represent atomic nuclei, the arrows show the atom's net magnetic moment, and the oval shapes mean the non-spherically distributed electrons about each nucleus. The upper row of atoms depicts the paramagnetic state above Tc. When the spin-orbit coupling is very strong below Tc, the effect of the spontaneous magnetization would rotate the spins and electron clouds into some particular orientation determined by the crystalline anisotropy (left to right for the middle row in Fig. 1.20). The nuclei would be forced further apart, and the spontaneous magnetostriction would be $\Delta L'/L'$. If we then apply a strong magnetic field vertically, the spins and electron clouds would rotate through 90° and would experience the magnetostrictive strain by an amount of $\Delta L/L$.

The strains pictured in this figure are enormously exaggerated. But, we know that in practice, the magnetostrictive strain produced in a domain or a crystal is usually very small, on the order of 10^{-5}. This means that the reorientation of electron clouds takes place only to a very small extent. This conclusion is supported by the fact that orbital magnetic moments are almost entirely quenched in most materials (i.e. not susceptible to rotation by an applied field).

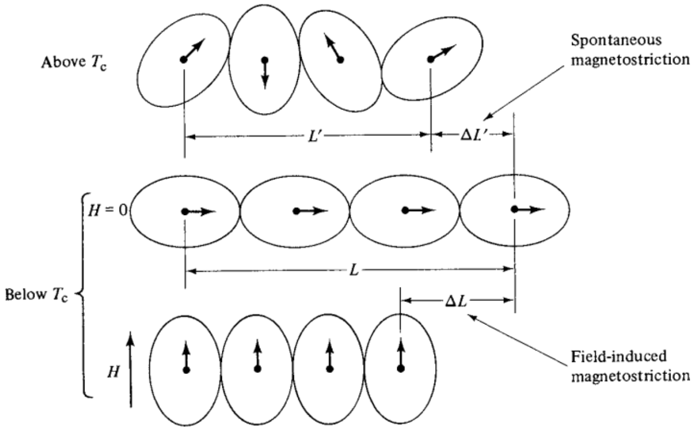

Figure 1.20. Mechanism of magnetostriction (schematic).

The rare-earth metals are exceptions to the above statements. Many of them are ferromagnetic only at temperatures well below room temperature, and their orbital moments are not quenched and the spin-orbit coupling is strong. Moreover, the electron cloud about each nucleus is decidedly non-spherical. Therefore, when an applied field rotates the spins, the orbits rotate accordingly, resulting in a considerable distortion. At 22K the saturation magnetostriction of Dy is about 4.5×10^{-3} in the basal plane (i.e. about 100 times of non-rare-earth metals and alloys). Some rare-earth compounds with transition metals Fe, Ni, and Co also have abnormally large values of magnetostriction with Curie points above room temperature.

Considering that the magnetostriction and crystalline anisotropy are both due to spin-orbit coupling, we would expect some correlation between the two. In fact, a large value of the anisotropy constant K_1 is usually accompanied by a large value of λ_S. For example, hexagonal substances tend to have larger absolute values of both K_1 and λ_S than cubic ones. And in binary alloys, the addition of the second element in solid solution often decreases both K_1 and λ_S. These are just general trends, however, and there are exceptions [29].

Although the magnetostrictive strain is small in most magnetic materials, the existence of magnetostriction means that applied mechanical stress can alter the domain structure and create a new source of magnetic anisotropy. This can have a substantial effect on the low-field magnetic properties, such as permeability and remanence. Figure 1.21(a) shows the effects of applied stress on the magnetization behavior of polycrystalline Ni. At 10 Oe (800 A/m), a compressive stress of 10,000 lb/in2 (70 MPa) almost doubles the permeability μ, while the same amount of tensile stress reduces μ to about one-tenth of the zero-stress value and makes the M-H curve practically linear. The magnetostriction of Ni is negative making the values of magnetization and permeability larger under compressive stresses. For a material with positive magnetostriction such as 68 permalloy, the effect of stress is just the opposite. Applied tensile stress (rather than compressive) increases the permeability of this alloy as shown in Fig. 1.21(b).

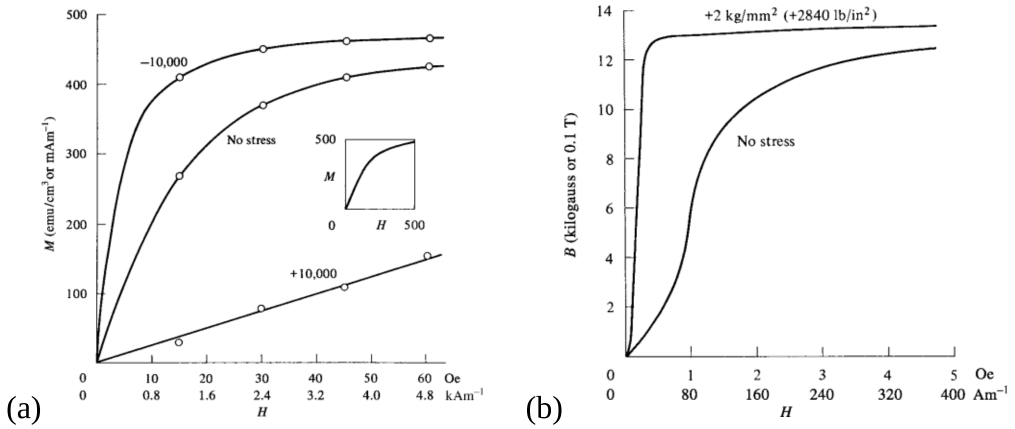

Figure 1.21. (a) Effect of applied tensile (+) and compressive (-) stress on the magnetization curve of polycrystalline Ni. (b) Effect of applied tensile stress on the magnetization curve of 68 permalloy [30].

There is a close connection between the magnetostriction λ of a material and its magnetic behavior under stress. As a result, the effect of stress on magnetization is sometimes called the inverse magnetostrictive effect, but more commonly is referred to simply as a magneto-mechanical (or magnetoelastic) effect. These results could have been anticipated by a general argument based on Le Chatelier's principle. For example, a material having positive λ will elongate when magnetized, and in turn, applied tensile stress which tends to elongate it will increase the magnetization and applied compressive stress will decrease it. These conclusions are valid whether or not a magnetic field is acting, as long as M is not zero. Thus, in Fig. 1.22, if a field H_1 produces a magnetization of A at zero stress, the application of a stress $+\sigma_1$ will raise the magnetization to B at a constant field. The magnetization in the remanent state at zero stress is C, and the same stress $+\sigma_1$ will increase this to D. But stress applied to a demagnetized specimen will not produce any magnetization, as shown by the intersection of the full-line and dashed curves at the origin.

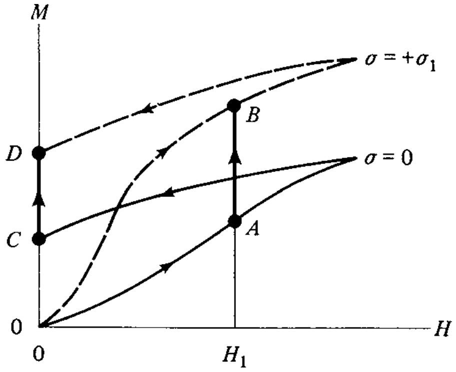

Figure 1.22. Effect of tension on the magnetization of a material with positive magnetostriction.

So far, we have implicitly assumed that H, M (or B), and σ are all parallel, but, in general, M and σ may not be parallel. We know that the amount of magnetostrictive strain exhibited by a crystal in a particular direction depends on the direction of the magnetization. If we impose an additional strain by applying stress, we expect that the direction of the magnetization will change. We therefore need a general relation between the direction of M_s within a domain and the direction and magnitude of σ. But, in the absence of stress, the direction of M_s is controlled by magnetic anisotropies including crystalline anisotropy, as characterized by the first anisotropy constant K_1. Therefore, when stress is acting, the direction of M_s is controlled by both σ and K_1. These two quantities are therefore involved in the expression for the energy which depends on the direction of M_s. For a cubic crystal,

$$E = K_1({\alpha_1}^2{\alpha_2}^2 + {\alpha_2}^2{\alpha_3}^2 + {\alpha_3}^2{\alpha_1}^2) - \frac{3}{2}\lambda_{100}\sigma({\alpha_1}^2{\gamma_1}^2 + {\alpha_2}^2{\gamma_2}^2 + {\alpha_3}^2{\gamma_3}^2)$$

$$- 3\lambda_{111}\sigma(\alpha_1\alpha_2\gamma_1\gamma_2 + \alpha_2\alpha_3\gamma_2\gamma_3 + \alpha_3\alpha_1\gamma_3\gamma_1),$$

where α_1, α_2, α_3 are the direction cosines of M_s, and γ_1, γ_2, γ_3 are the direction cosines of the stress σ. The units of E are erg/cm^3 if σ is expressed in dyne/cm^2 or J/m^3 if σ is expressed in Pa = N/m^2.

The first term of the equation is the crystalline anisotropy energy. The next two terms, which involve the magnetostrictive strains and the stress, comprise what is usually called the magnetoelastic energy E_{me}. The direction which makes E a minimum becomes an equilibrium of M_s, and this direction seems to be a complicated function of K_1, λ_{100}, λ_{111}, and σ, for any given stress direction γ_1, γ_2, γ_3. But we can qualitatively consider that the direction of M_s will be determined largely by crystalline anisotropy when K_1 is much larger than $\lambda_{100}\sigma$ and $\lambda_{111}\sigma$; when this inequality is reversed, the stress will control the M_s direction.

When the magnetostriction is isotropic, so that $\lambda_{100} = \lambda_{111} = \lambda_{si}$, the last two terms of the above equation reduce to a very simple form for the magnetoelastic energy:

$$E_{me} = -\frac{3}{2}\lambda_{si}\sigma cos^2\theta$$

where ɵ is the angle between M_s and σ. As before, we can substitute (1 - $\sin^2$ ɵ) for $\cos^2$ ɵ, drop an angle-independent term, and write the energy as

$$E_{me} = \frac{3}{2}\lambda_{si}\sigma sin^2\theta$$

Stress alone can create an easy axis of magnetization. Therefore, when stress is present, stress anisotropy must be considered along with any other anisotropies that may exist. If it is a uniaxial anisotropy, and the relation which governs will be the same form as the uniaxial crystalline anisotropy or the shape anisotropy. We therefore write for the stress anisotropy energy or magnetoelastic energy as

$$E_{me} = K_\sigma sin^2\theta$$

,where the magnetoelastic anisotropy constant K_σ is given by $\frac{3}{2}\lambda_{si}\sigma$. The axis of stress is an easy axis if $\lambda_{si}\sigma$ is positive. If this quantity is negative, the stress axis is a hard axis and the plane normal to the stress axis is an easy plane of magnetization.

1.3 Dissertation Overview

The focus of this dissertation is to develop high-quality and functional magnetoelastic materials and to study the underlying mechanisms coupling magnetism to strain. On the basis of the topics covered in the introduction, Chapter 2: Magnetostrictive Terfenol-D Thin Film and XMCD Investigation will begin with the material development of high-quality Terfenol-D thin films having giant magnetoelastic properties (Chapter 2.2). The chapter will move on to the elemental magnetic analysis of the films by using the XMCD technique (Chapter 2.3). Then, by using the sum rule analysis it will focus on the elemental spin and orbital magnetic moments and their correlation with the magnetic anisotropies (Chapter 2.4). Prior to this research work, Chapter 2.1 will provide a solid background on magnetoelastic materials and XMCD technique.

Chapter 3: Strain-Modulated Exchange Spring Magnet will focus on the development of magnetoelastic TbFe films which can enable an in-plane 180° switching by applied strain. This will begin with the fabrication and material characterization of amorphous TbFe films (Chapter 3.2). Then, this chapter will describe the magnetic properties of the TbFe films including exchange spring magnetic (ESM) behavior (Chapter 3.3) and their strain-applied switching (Chapter 3.4). For a better understanding of this topic, the key features on the ESM and amorphous ferrimagnetic alloys are introduced in Chapter 3.1.

Chapter 4: TbFe Thin Films Having Perpendicular Magnetic Anisotropy (PMA) will focus on the magnetoelastic TbFe films showing PMA which are more useful to be applied to practical devices. This chapter will first show the fabrication of PMA TbFe films (Chapter 4.2). Then, the parameters affecting the PMA of TbFe films will be discussed (Chapter 4.3). Prior to show this work, the usefulness, and origin of PMA are covered to emphasize the importance of this topic and provide its background in Chapter 4.1.

Finally, Chapter 5 will summarize the three different topics on magnetoelastic materials and indicate what potential advances will become possible with these high-quality and functional magnetoelastic materials.

1.4 Chapter References

1] Actel Power Matters, “Total System Power – Evaluating The Power Profile of FPGAs” (2008)

2] T. H. Lee, and S. H. Lim, Phys. Stat. Sol. (c), **4**, 4341 (2007)

3] J. K. Han, J. H. NamKoong, and S. H. Lim, J. Phys. D: Appl. Phys. **41**, 232005 (2008)

4] C. W. Han, J. K. Han, and S. H. Lim, J. Appl. Phys. **106**, 094508 (2009)

5] K. J. Lee, A. Deac, O. Redon, J. P. Nozières, and B. Dieny, Nat. Mater. **3**, 877–881 (2004)

6] S. Yakata, H. Kubota, Y. Suzuki, K. Yakushiji, A. Fukushima, S. Yuasa, and K. Ando, J. Appl. Phys. **105**, 07D131 (2009)

7] C. J. Lin et. al., 2009 IEEE International Electron Devices Meeting (IEDM), 1-4 (2009)

8] P. K. Amiri, and K. L. Wang, 2014 IEEE 6th International Memory Workshop (IMW), 1-4 (2014)

9] J. Domann, T. Wu, T. K. Chung, and G. Carman, MRS Bulletin, **43**(11), 848-853 (2018)

10] J. M. Hu, Z. Li, L. Q. Chen, and C. W. Nan, Nat. Comm. **2**, 553 (2011)

11] W. Eerenstein, N. D. Mathur, and J. F. Scott, Nat. **442**, 759 (2006)

12] M. Bibes, and A. Barthelemy, Nat. mater. **7**, 425 (2008)

13] J. Domann, and G. Carman, J. Appl. Phys. **121**, 044905 (2017)

14] Z. Yao, Y. E. Wang, S. Keller, and G. P. Carman, IEEE Antennas Propag. Mag. **63**, 3335 (2015)

15] M. M. Vopson, Critical Reviews in Solid State and Materials Sciences, **40**, 223 (2015)

16] J. T. Heron et al., Nat. **516**, 370–373 (2014)

17] Y. Wang, J. Hu, Y. Lin, and C. W. Nan, NPG Asia mater. **2**, 61 (2010)

18] J. Ryu, A. V. Carazo, K. Uchino, and H.-E. Kim, Jpn. J. Appl. Phys. **40**, 4948 (2001)

19] G. Srinivasan, E. T. Rasmussen, B. J. Levin, and R. Hayes, Phys. Rev. B, **65**, 134402 (2002)

20] D. A. Pan, S. G. Zhang, A. A. Volinsky, and L. J. Qiao, J. Phys. D: Appl. Phys. **41**, 172003 (2008)

21] H. K. D. Kim, L. T. Schelhas, S. Keller, J. L. Hockel, S. H. Tolbert, and G. P. Carman, Nano Lett. **13**, 884−888 (2013)

22] J. Cui, J. L. Hockel, P. K. Nordeen, D. M. Pisani, C. Liang, G. P. Carman, and C. S. Lynch, Appl. Phys. Lett. **103**, 232905 (2013)

23] T. H. Lee, H. C. Koo, H. Kim, S. H. Han, and S. H. Lim, Met. Mater. Int. **17**, 509 (2011)

24] T. Lee, M. K. Panduranga, C. W. Han, V. Ortalan, and G. P. Carman, Phys. Rev. Appl. **8**, 024024 (2017)

25] B. D. Culity, and C. D. Graham, Introduction to Magnetic Materials, Second Edition, Wiley (2008)

26] E. C. Stoner, and E. P. Wohlfarth, Phil. Trans. R. Soc, **A-240**, 599 (1948)

27] T. H. Lee, H. C. Koo, K. H. Kim, H. Kim, J. Chang, S. H. Han, J. Hong, and S. H. Lim, J. Magn. Magn. Mater. **321**, 3795 (2009)

28] J. P. Joule, The London, Edinburgh, and Dublin Philosophical Magazine and Journal of Science, University of London (1842)

29] E. du Trémolet de Lacheisserie, D. Gignoux, M. Schlenker, Magnetism – Materials and Applications, Springer (2005)

30] R. M. Bozorth, Ferromagnetism, IEEE Press (1993)

2. Magnetoelastic Terfenol-D Thin Film and XMCD Investigation

2.1 Introduction

2.1.1 Magnetoelastic Materials and Terfenol-D

All magnetic materials exhibit magnetostriction to some degree and can be regarded as magnetoelastic materials. However, giant (or practically applicable) magnetostriction occurs in a small number of materials containing rare earth elements since they have a strong magnetoelastic coupling or magnetoelasticity.

In the rare earth elements, the unbalanced spins are sheltered in an inner orbital shell which has essentially no overlap with orbitals on neighboring atoms and no participation in the bonding. This occurs because in the rare earths the 4f orbital shell is filled in an “abnormal” order. Two or three valence electrons occupy the 6s and 5d states before the more tightly bound 4f shell is filled. The typical rare earth atomic configuration is $[Xe]4f^n5d^{(1or0)}6s^2$. The 4f subshell has seven orbital states which can hold a total of 14 electrons. For simplicity, only 3+ ions are considered here. Gd, in the middle of the rare earth series, has 7 4f electrons which exactly half-fill the available states ($n_+=7$ and $n_-=0$) giving it the largest of the rare earth spin moments ($\mu_s=7\mu_B$). The heavy rare earths (Gd-Yb) have a full component of 7 (+)-spin electrons plus some (-)-spin electrons which act to cancel part of the spin moment. For example, Tb has $n_+=7$ and $n_-=1$, so $\mu_s=6\mu_B$ [1].

In addition to the spin imbalance, the partially filled 4f shell has an orbital imbalance which gives both an orbital contribution to the magnetic moment and an anisotropic physical shape to the ion. Figure 2.1 shows the calculated ionic shapes for the rare earth series. Gd, with each 4f orbital state occupied by one electron, is spherical. Tb, with one 4f orbital doubly occupied and six singly occupied, is oblate. The orbital contribution to the magnetic moment adds to the spin moment for the heavy rare earths. The heavy atoms have more positively charged protons in the nucleus, and thus, stronger centripetal forces. This fact makes their electrons move faster in a given orbit than do light atoms. The spin directions of the rapidly moving 4f electrons are strongly coupled to the orientations of their orbits. This strong spin-orbit coupling of the individual electrons leads to a strong magnetocrystalline anisotropy and a giant magnetoelastic coupling of the rare earth elements or their compounds [1].

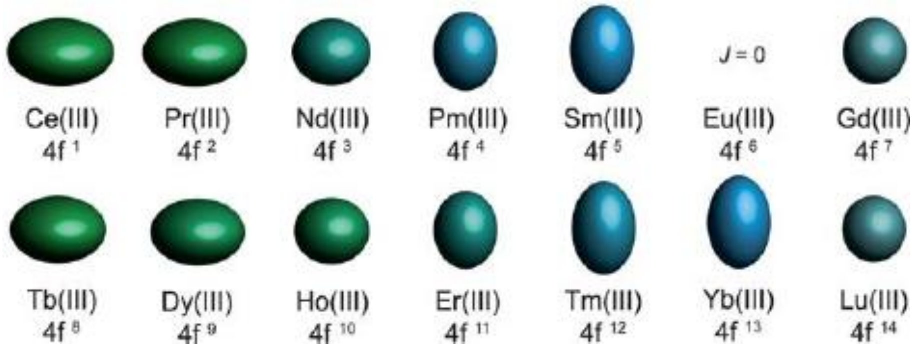

Figure 2.1. 4f electron charge cloud density for the rare earth elements [2]

The magnetization and giant magnetoelastic coupling of rare earth elements, however, cannot be seen at room temperature due to their low Curie temperatures. So, a search was begun for alloys or compounds with high magnetostriction at room temperature. The magnetic transition metals all have strong exchange interactions leading to high Curie temperatures and alloys of these elements with rare earths were investigated for magnetostriction at room temperature. Finally, magnetostriction exceeding 10^{-3} is measured in $TbFe_2$ in 1972 [3]. This compound has high Curie temperature (~700 K) and was considered to be prime candidates for use in devices operating over a wide temperature range. $TbFe_2$, Terfenol, became the overwhelming choice for development for use as drive elements in transducers in the 1980s and 1990s. These RFe_2 compounds crystallize in the cubic Laves phase (C_{15}) structure as shown in Fig. 2.2.

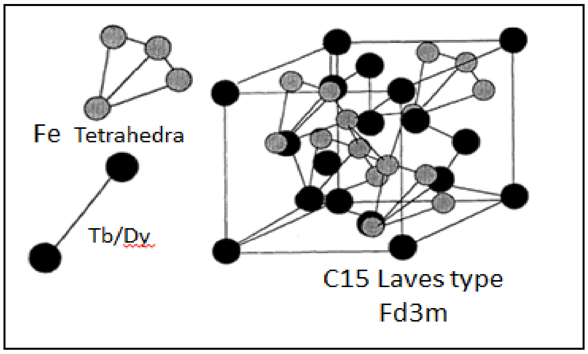

Figure 2.2. The cubic Laves phase structure. The rare earth atoms are represented by the large black spheres and the Fe atoms are represented by the smaller gray spheres.

The magnetostrictions and Curie temperatures for various crystalline RFe_2 compounds are shown in Fig. 2.3. Large magnetostrictions persist in these compounds up to and higher than room temperature. This can be understood by two reasons. First, the rare earths' magnetoelasticity is associated with the inner shell electrons which do not participate in the bonding. Second, in the RFe_2 compounds, the rare earth ions are strongly exchange coupled to the Fe ions so that the rare earth sublattice remains ordered, with a large sublattice magnetization up to high temperatures.

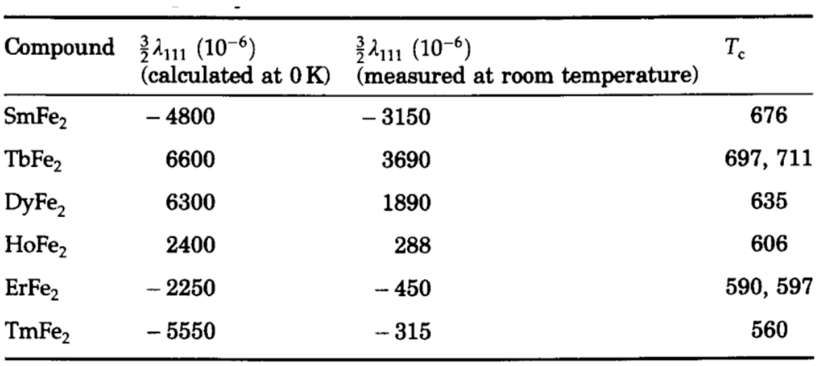

Compound	$\frac{3}{2}\lambda_{111}$ (10^{-6}) (calculated at 0 K)	$\frac{3}{2}\lambda_{111}$ (10^{-6}) (measured at room temperature)	T_c
$SmFe_2$	−4800	−3150	676
$TbFe_2$	6600	3690	697, 711
$DyFe_2$	6300	1890	635
$HoFe_2$	2400	288	606
$ErFe_2$	−2250	−450	590, 597
$TmFe_2$	−5550	−315	560

Figure 2.3. Magnitudes of single crystal magnetostriction in rare earth-Fe_2 compounds [1].

However, it was recognized that the magnetic anisotropy of $TbFe_2$, which has the highest magnetostriction at room temperature, is huge. This means that large, impractical magnetic fields are required to realize the magnetostrictive strains in $TbFe_2$. Fortunately, the magnetic anisotropy can be totally compensated by substitution of other rare earths with same-sign magnetostriction and opposite-sign anisotropy constants of those for $TbFe_2$ (see Fig. 2.4). The candidates to accomplish this anisotropy minimization in $TbFe_2$ (Terfenol) are Ce, Pr, Nd, Dy, and Ho. The selection of which candidate to use has a significant impact on the solidification of the final alloy.

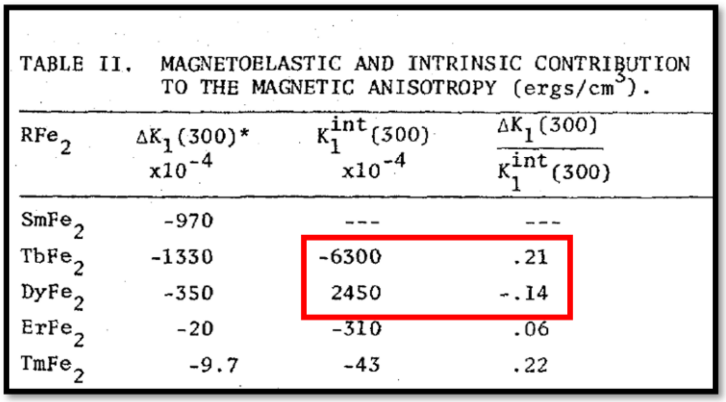

TABLE II. MAGNETOELASTIC AND INTRINSIC CONTRIBUTION TO THE MAGNETIC ANISOTROPY (ergs/cm^3).

RFe_2	$\Delta K_1(300)^*$ $\times 10^{-4}$	$K_1^{int}(300)$ $\times 10^{-4}$	$\frac{\Delta K_1(300)}{K_1^{int}(300)}$
$SmFe_2$	-970	---	---
$TbFe_2$	-1330	-6300	.21
$DyFe_2$	-350	2450	-.14
$ErFe_2$	-20	-310	.06
$TmFe_2$	-9.7	-43	.22

Figure 2.4. Magneto anisotropy constants of various rare earth-Fe_2 compounds.

Dy was found to be the most effective rare earth (R) to reduce the magnetization anisotropy in Terfenol while producing a minimal reduction in strain. Consequently, the pseudobinary family of alloys Terfenol-D, $Tb_xDy_{1-x}Fe_2$, became the giant magnetostrictive material for further development in the 1980s and 1990s. For x=0.27, the anisotropy is minimized and the sacrifice in strain, for example, 3690 ppm for $TbFe_2$ and 2460 ppm for $Tb_{0.27}Dy_{0.73}Fe_2$, is justified since the fields required to produce these strains are reduced from the impractical 25 kOe for $TbFe_2$ to a practical drive field of < 2 kOe for $Tb_{0.27}Dy_{0.73}Fe_2$ [3-9]. Dy is the immediate neighbor of Tb in the rare earth series and nearly of the same atomic size. Tb and Dy from a complete solid solution with a linear relationship between both the melting points. Terfenol-D can be considered a pseudobinary intermetallic compound for all values of x in $Tb_xDy_{1-x}Fe_2$ and can be represented as RFe_2. Reasonably accurate pseudobinary phase diagrams can be constructed for these R-Fe systems, where $R=Tb_xDy_{1-x}$.

To realize advanced nano/micro strain-mediated multiferroic systems, thin film deposition techniques of the magnetoelastic materials are of special interest because they are capable of cost-effective mass production compatible to nano/micro process technologies. Terfenol-D thin films have been produced by the DC magnetron sputtering technique, either from a single alloy target or multiple targets. Several fabrication and characterization studies on sputter deposition of thin film Terfenol-D have been conducted during the last three decades. In 1994, P. I. Williams et al. showed composition dependence in the properties of $(Tb_{1-x}Dy_x)Fe_2$ polycrystalline thin films and observed in-plane magnetostriction coefficient ($\lambda_{\parallel}$) of 500×10^{-6} and a saturation magnetization (M_s) of 550 emu/cc in $Tb_{0.3}Dy_{0.7}Fe_2$ polycrystalline thin film as shown in Fig. 2.5.

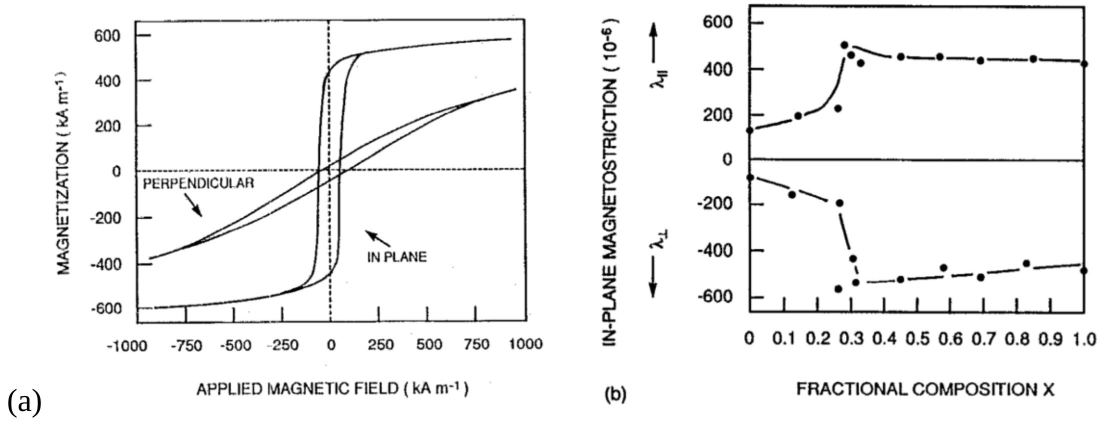

Figure 2.5. (a) In-plane and perpendicular M-H loops for a polycrystalline $(Tb_{0.3}Dy_{0.7})Fe_2$ film. (b) $\lambda_{\parallel}$ and $\lambda_{\perp}$ as a function of x for $(Tb_xDy_{1-x})Fe_2$ films [9].

In 1997, A. Speliotis et al. investigated the effect of substrate temperature (T_s) during deposition on Curie temperature (T_c) and magnetostriction. Figure 2.6(a) shows the relation between T_s and T_c. As T_s increases, higher T_c is measured. Especially, beyond T_s = 400 ℃, T_c sharply increases. This is related to the fact that Terfenol-D films deposited higher than 400 ℃ start to show crystalline phases. And, the higher T_s samples show larger magnetostriction values up to 800 ppm as shown in Fig. 2.6(b).

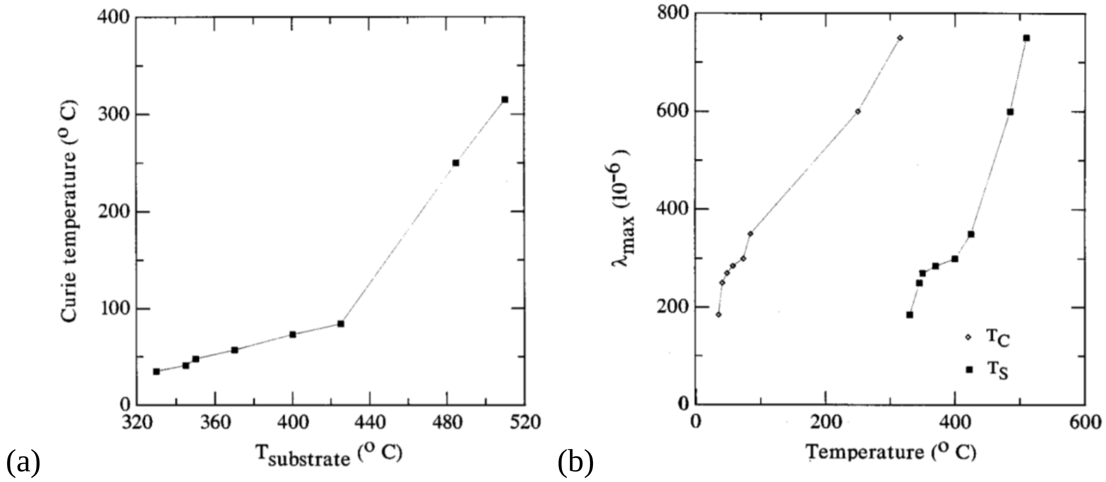

Figure 2.6. (a) The dependence of the Curie temperature T_C on the substrate temperature T_S of amorphous and partially crystalline TbDyFe thin films (b) The dependence of the magnetostrictive coefficient λ at the maximum applied field, 4 kOe, on T_S and T_C [4].

Figure 2.7 presents the magnetic field dependence on the magnetostriction of Terfenol-D films, amorphous samples in (a) and partially crystalline samples in (b). Among the amorphous samples, 400 ℃ film records the magnetostriction of 400 ppm. On the other hand, partially crystalline samples show mostly higher magnetostriction values than the ones of amorphous samples; 750 ppm is measured at the 511 ℃ film. Other than the maximum magnetostriction values, an important difference in the magnetostriction curves between amorphous and crystalline samples is the existence of hysteresis. The sweep-up and sweep-down curves in Fig. 2.7(b) follow different trajectories making the curves broader than ones in Fig. 2.7(a). This is because the partially crystalline Terfenol-D samples have higher coercive field > 1kOe as they crystallize.

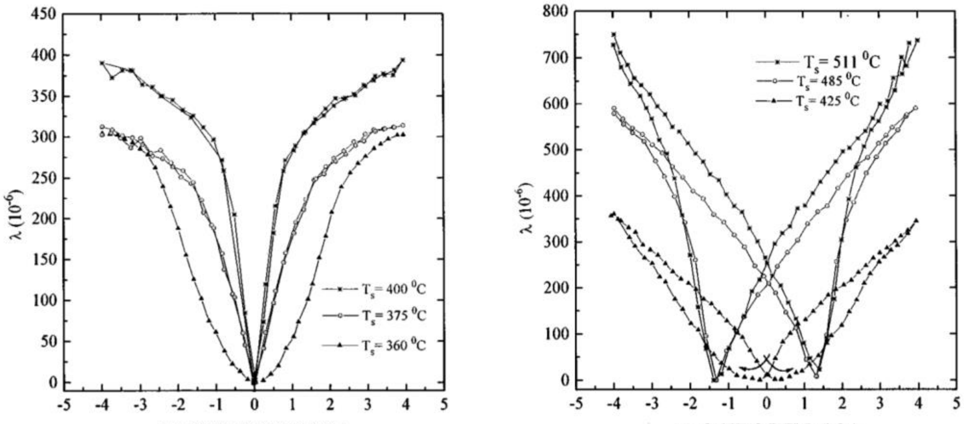

(a) (b)

Figure 2.7. The magnetostriction curves of (a) amorphous TbDyFe films deposited at temperatures 360, 375 and 400 °C and (b) partially crystalline films deposited at temperatures 425, 485 and 510 °C [8].

To sum up, as in the introduced literature, as-deposited films are always amorphous with relatively poor magnetic properties. The thin films must be crystallized to obtain mechanical and magnetic properties close to bulk Terfenol-D. This can be achieved either by depositing the film on a heated substrate or by post-annealing. Furthermore, the film's atomic compositions, crystallinity, magnetic and mechanical properties are strongly influenced by processing parameters which in turn greatly influence the film's magnetoelastic properties. Hence, it is required to understand the process parameters in order to obtain the properties close to bulk Terfenol-D.

2.1.2 X-ray Msuagnetic Circular Dichroism (XMCD)

X-ray absorption spectroscopy (XAS) has become one of the fundamental and most used techniques by the biochemistry and materials science communities to study the local structure and oxidation states in catalysts and other chemical complexes. In XAS, an incoming photon interacts with a deep-core electron, which is then promoted to some unoccupied state above the Fermi energy. The deep-core electron propagates away and leaves behind a core-hole. A short time later (1 or 2 femtoseconds), a higher-lying electron decays into the core-hole and emits a photon. Alternately, the energy from the higher-lying electron can be used to emit an Auger electron [10]. Since each element has a characteristic set of excitation and fluorescence energies, we can detect the elements on samples and the valence states of the elements as represented in Fig. 2.8.

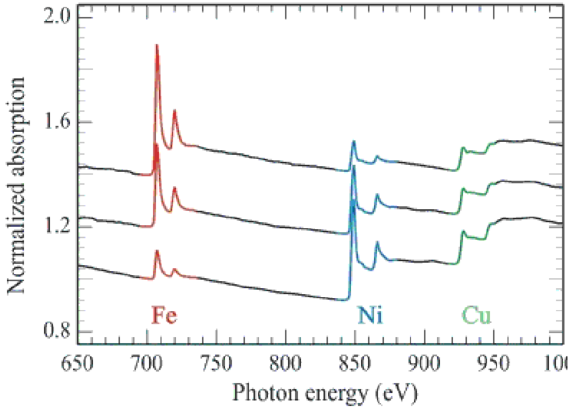

Figure 2.8. Typical XAS spectrums shown for transition metals (Fe, Ni, and Cu).

On the top of the XAS technique, the X-ray magnetic circular dichroism (XMCD) spectrum is obtained as the difference between the two XAS spectra with the circular polarization vector parallel and antiparallel to the magnetic moments of the samples. Hence, the technique resemblances the magneto-optical phenomena in the visible region, such as the Faraday effect.

Unlike the latter, the XMCD arises from the excitation of a core electron, instead of a valence electron, into the unoccupied conduction states.

Figure 2.9(a) represents a simple picture of a two-step process of XMCD with an example of a 3d transition metal, Co. The 2p core state of a 3d metal is split in a j = 3/2 level (L_3 edge) and j = 1/2 level (L_2 edge), where spin and orbit are coupled parallel (j=l+s) and antiparallel (j=l-s), respectively. In the first step, a circularly polarized photon excites a spin-polarized electron from the spin-orbit split 2p level. The emission with the light helicity vector parallel (antiparallel) to the 2p orbital moment results in excited electrons of preferred spin up (down) direction. In the second step the excited electron has to find its place in the unoccupied 3d valence band, and if there are less spin-up than spin-down holes available, the XMCD spectrum has a net negative L_3 and positive L_2 peak. Figure 2.9(b) shows the resultant XAS signal at the Co $L_{2,3}$ for the right (μ^+) and left (μ^-) circular polarization together with the difference spectrum: the XMCD [10].

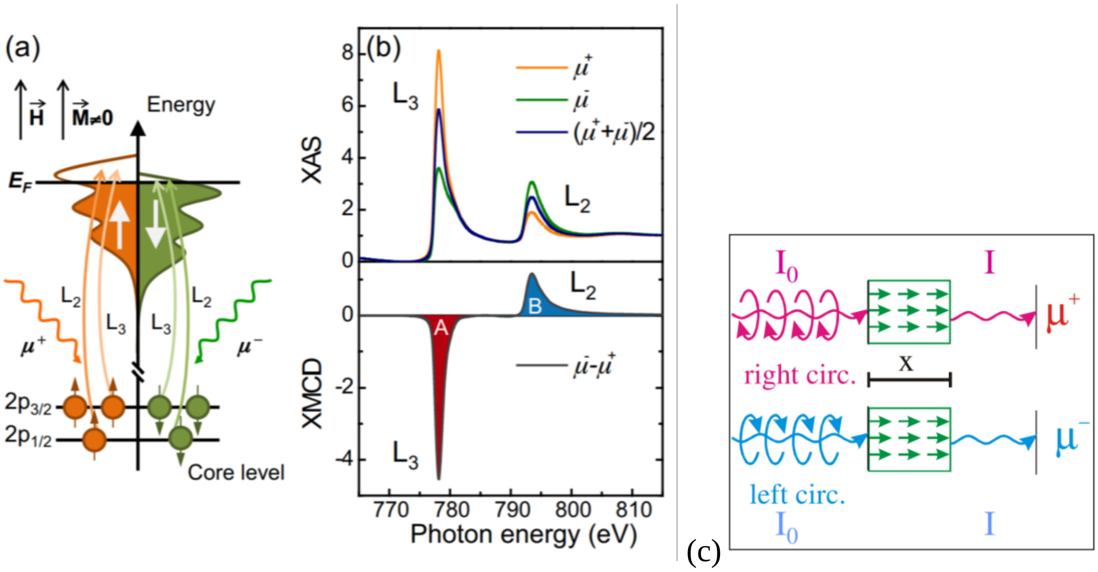

Figure. 2.9. (a) Diagram of the two-step picture of XMCD for a single-electron in the resonant excitation process for a magnetic material (b) XAS at the Co $L_{2,3}$ for right (μ^+) and left (μ^-) circular polarization together with the difference spectrum: the XMCD [10].

For maximum XMCD effect, the magnetization direction M of the sample and the photon spin or angular momentum L_{ph} are chosen to be collinear as depicted in Fig. 2.9(c). The dichroism effect is then given by the difference of the p → d transition (X-ray absorption) intensities, measured for photons with positive angular momentum ($q=+1$, L_{ph} points in direction of wavevector k) and negative angular momentum ($q=-1$, L_{ph} points in direction of $-k$) aligned along the fixed magnetization direction M of the sample. An equivalent way is to fix the X-ray photon spin direction and switch the magnetization directions [11].

Denoting the magnetization M and photon angular momentum L_{ph} directions by arrows, the dichroism effect is only dependent on the relative alignment of the two arrows. The convention adopted by the XMCD community is to plot the dichroism intensity of the 3d transition metals Fe, Co, and Ni so that the L_3 dichroism is negative. According to Fig. 2.9 this corresponds to the definition,

$$\Delta I = I^{\uparrow\downarrow} - I^{\uparrow\uparrow}.$$

Note that the minority electron spin direction (= majority hole spin direction) is the same as that of the sample magnetization. The XMCD difference intensity, defined as the white-line intensity difference between antiparallel and parallel orientations of the sample magnetization and the incident photon spin is directly proportional to the atomic magnetic moment.

$M_{4,5}$ edges of rare earths have been the first test case for the XMCD theory. Edges are dominated by 3d → 4f transitions which have very large absorption cross sections and are fairly independent on the local chemistry of the ion. The atomic description of 3d → 4f transitions relies on the strong localization of the 4f electrons with respect to 5d and 6s electrons. These edges are calculated for a trivalent ion that has lost the outermost (5d6s)3 electrons. Electronic levels are determined by Coulomb interactions, then by spin-orbit (SO) coupling [12].

Using XMCD, the absorption becomes sensitive to the magnetic polarization of the atoms, which offers a method for element-specific magnetometry. Element-specific hysteresis curves can be recorded by sweeping the field. This is important for the understanding of ferrimagnetic materials or their composite structures where minor-spin element's magnetic behavior and their interactions become crucial in some cases but are hard to be detected other than the XMCD and corresponding element-specific hysteresis curves.

Since the light interacts only with the orbital and not with the spin part of the wave function, the XMCD can be used to distinguish between the spin and orbital part of the magnetic moment. The sum rules, derived in the early 1990s, relate the integrated intensities over the absorption edges of the XMCD to the spin and orbital moments of the ground state [13,14]. The discovery of the sum rules has transformed XMCD into the powerful standard technique that it is today. The angular dependence can be employed to deduce the microscopic origin of anisotropic magnetic properties, such as the magneto-crystalline anisotropy energy, easy direction of magnetization, magnetostriction, and coercivity. Sum rules are valid for both localized and itinerant electron systems—they are in fact theory independent. The XMCD sum rules complement the earlier sum rules for the isotropic XAS, which relate the total integrated intensity to the number of valence holes, and relate the core-level spin-orbit split branching ratio to the angular part of the spin-orbit interaction [15,16].

The decay of the created core holes results in an avalanche of electrons, photons, and ions emitted from the sample surface. Detection of any of these emitted particles can be used to measure samples of arbitrary thickness. For soft X-rays the common detection method is transmission or total electron yield (TEY) where Auger is the dominant decay process, cascading into secondary electron emission. Figure 2.10 shows schematic features for transmission and TEY modes for XMCD detection [17]. Detailed explanations of the two modes are specified in the following paragraphs.

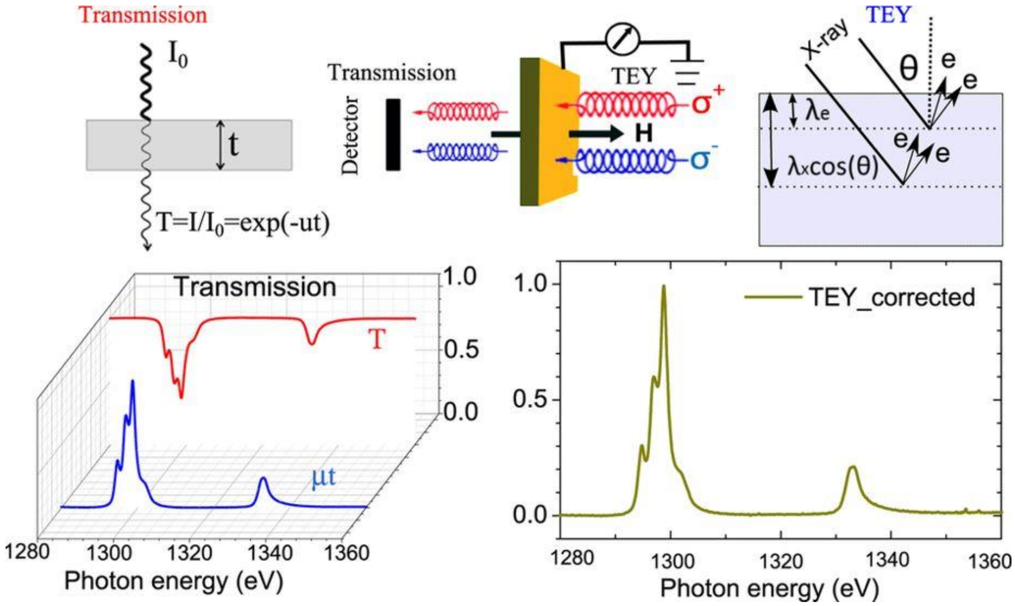

Figure 2.10. (Up) XMCD measurements of transmission and TEY mode, the transmitted x-ray intensities and total electron yield from the sample are recorded. (Down)The XAS was extracted as the logarithm of the ratio of the transmitted x-ray intensities, or the drain current from the sample after the correction of the saturation effect. [17]

Only transmission measurements can give absolute absorption cross sections. The transmitted intensity of X-rays, at incident angle ɵ with respect to the normal, passing through a sample of thickness x is given by the Lambert-Beer law,

$$I(\omega) = I_0 e^{-\mu(\omega)x/cos\theta}$$

where I_0 is the incident intensity and μ the linear absorption coefficient, which depends on the photon energy ω. The X-ray attenuation length or absorption depth is defined as $\Lambda(\omega) \equiv \mu(\omega)^{-1}$. Because of the short absorption depth of soft X-rays, samples for transmission measurements have to be very thin and need to be spatially homogeneous to avoid non-linear effects. Thick or porous samples may show suppressed absorption features due to ‘leakage’ effects, and consequently a diminished XMCD, especially if higher harmonics are present in the incident beam. Except for nanoparticles, the particle size of most samples will be larger than the sampling depth at resonance. For soft X-rays, samples can be fabricated in the form of thin films or multilayers, grown on, e.g., boron nitride, Kapton, or parylene [18]. Thin films, grown on MgO or sapphire, can be measured in transmission by using the luminescence signal from the substrate, which is excited by the X-rays that pass through the sample [19].

The strong secondary electron emission renders TEY as the preferred detection method in the soft X-ray region. The TEY can be measured either using a channeltron electron multiplier (CEM) or as the drain current flowing from ground to the sample to compensate the electron emission current. TEY detection shows a high surface sensitivity due to the short electron escape depth, which makes it rather sensitive to oxidation. Such oxidation effects in the XAS show up as extra features usually a few eV above the main peak, while the intensity of the XMCD is reduced when the oxidized atoms are non-magnetic. Therefore, samples prone to oxidation necessitate a special treatment, such as in situ preparation (evaporation, cleaving, ion sputtering) or alternatively the sample should be capped with a few nm thick layer of an inert material, such as Al, Au, Pt, or MgO, although this can give a proximity effect on the magnetic layer. TEY detection is ideal for monolayer coverages or magnetic adatoms, capable of measuring the XMCD of 0.005 of a monolayer coverage [20].

2.2 Thin film Terfenol-D

2.2.1 Fabrication of Polycrystalline Terfenol-D Films

Terfenol-D films have been produced using an alloy target, $Tb_{0.3}Dy_{0.7}Fe_{1.92}$, procured from Etrema Products Inc., by DC magnetron sputtering in a high vacuum sputtering system with a load lock chamber. Parametric studies were conducted to evaluate the influence of sputtering powers (150 to 350 Watts), Argon pressures (1.5 to 20 mTorr), substrate-to-target distances (d), (4.0 to 8.0 cm) (see Fig. 2.11) [21,22]. The film was deposited on a heated substrate at 250 ℃ and this temperature represents a lower bound on enhanced nucleation as determined from testing. Following this deposition, the film was post-annealed in-situ at CMOS-compatible temperature 450 ℃ for 4 hours at chamber pressure below 5×10^{-6} Torr [22]. After annealing, a thin (4 nm) Ta capping layer was deposited in-situ to prevent oxidation. Films were deposited onto 100 cm diameter (100) Silicon wafers or Al_2O_3 (Sapphire) single crystals. In all cases, the chamber's base pressure was kept below 7×10^{-8} Torr. The deposition process was adjusted to produce a nominal film thickness of 100 nm in all samples studied. 10 nm-thick Ta adhesive barrier layer was deposited prior to Terfenol-D deposition on all the substrates as depicted in Fig. 2.11.

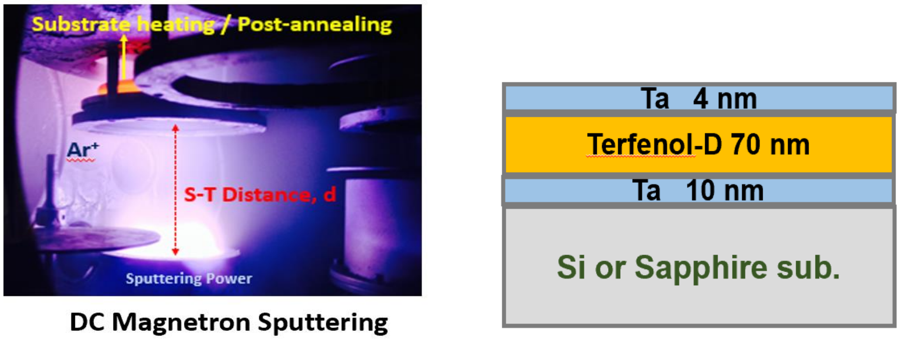

DC Magnetron Sputtering

Figure 2.11. (Left) Inside the sputtering chamber during the deposition. (Right) Schematic for the Terfenol-D sample layers from substrate to Ta capping.

A composition of the films largely depends on sputtering power. Sputtering powers were varied from 150 to 350 Watts in increments of 25 Watts while keeping Ar pressure constant at 5 mTorr and substrate to target distance of 5.5 cm. To determine the as-deposited film's composition, 5 mm×5 mm diced specimens were taken from the center of the wafer. The diced pieces were coated with a thin carbon layer prior to placing them on a sample holder of JEOL JXA-8230 SuperProbe, Wavelength Dispersive Spectrometer (WDS). The thin carbon layer prevents surface charge accumulation which otherwise influences the composition measurement. The use of WDS is required due to the overlap in the energy spectra of Tb, Dy, and Fe. Figure 2.12 shows the composition results measured by WDS. The average composition of the film at sputtering powers between 175 to 250 Watts was 10.3 at% of Tb, 23.7 at% of Dy and 66 at% of Fe which are close to that of the Terfenol-D target with minimal variations. For all subsequent films discussed here, a 250 Watts sputtering power was selected to produce the Terfenol-D thin films [21].

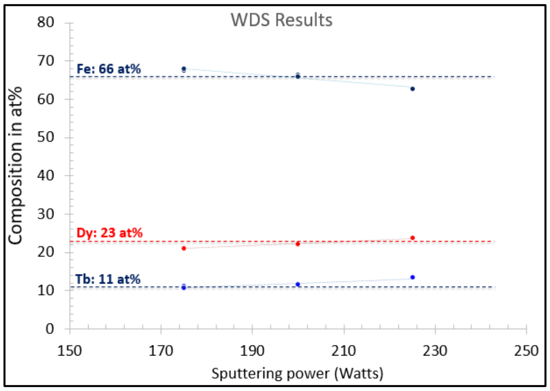

Figure 2.12. Atomic composition variations of Fe, Dy, and Tb in Terfenol-D films deposited with different sputtering power.

Residual stress is an important property of deposited Terfenol-D films. Residual stresses strongly influence the magnetic anisotropy of the film and its magneto-mechanical properties. The deposition parameters which contribute to residual stresses include Ar gas pressure, a substrate to target distance and mismatches in thermal expansion coefficients between the film and substrate. The mismatches in thermal expansion coefficient, α, between the film and substrate are Terfenol-D ($\alpha = 18\times10^{-6}$ /°C) film, Si ($\alpha = 2.6\times10^{-6}$ /°C), and Sapphire ($\alpha = 3.4\times10^{-6}$ /°C) at room temperature. To evaluate Ar gas pressure contributions, studies were conducted at a sputtering power of 250 Watts with a constant substrate to target distance of 5.5. Following the deposition, residual stress of both the amorphous and crystalline film was measured using a wafer curvature technique employing a dual wavelength (λ_1 = 670 nm and λ_2 = 750 nm) Tencore Flexus 2024 system. The average film stress, σ, was calculated using Stoney's equations cm and the results are presented in Fig. 2.13 [21].

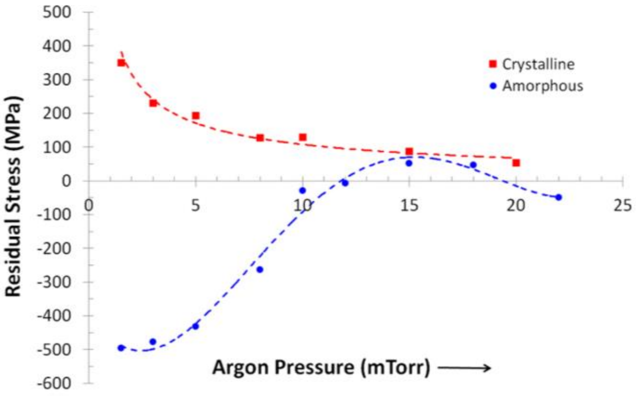

Figure 2.13. Variation of residual stresses with Argon gas pressure in amorphous and crystalline Terfenol-D thin films.

To examine the crystallinity and crystal orientation of the film, X-ray diffraction (XRD) was used with conventional θ-2θ reflection geometry using Bruker AXS Discover D8 X-ray diffractometer with fixed Cu-K_α radiation. Figure 2.14(a) shows simulated XRD patterns of single crystal Terfenol-D provided by Mercury Cambridge Structural Database (CSD) software for validation purposes. Figure 2.14(b) shows the X-ray diffraction pattern for Terfenol-D films post-annealed at three different temperatures: 250 °C, 400 °C, and

450 ℃. The post-annealed film at 250 ℃ does not show any prominent XRD peaks indicating an amorphous film. The film post-annealed at 400 ℃ exhibits weak XRD peaks corresponding to Terfenol-D indicating partial crystallization. Furthermore, the films annealed at both 250 ℃ and 400 ℃ show broad peaks at 2θ around 30 degrees corresponding to oxides of capping material. The film post-annealed at 450 ℃ shows prominent X-ray peaks at (111), (022), (311) and (222) planes corresponding to face-centered cubic (FCC) polycrystalline Terfenol-D. These results indicate that 450 ℃, i.e., CMOS compatible temperature, post-annealing produces polycrystalline Terfenol-D. The average grain size (D) of the 450 ℃ film is estimated from the Scherrer formula [23] given by

$$D = \frac{0.94\,\lambda}{(\beta - b)cos\theta}$$

, where β is the full width at half maxima (FWHM) of the diffraction peak, b is standard instrumental broadening, λ is the Cu-K_α X-ray radiation wavelength and θ is the Bragg diffraction angle. The average grain size of the 450 ℃ post-annealed films is ∼30 nm [22].

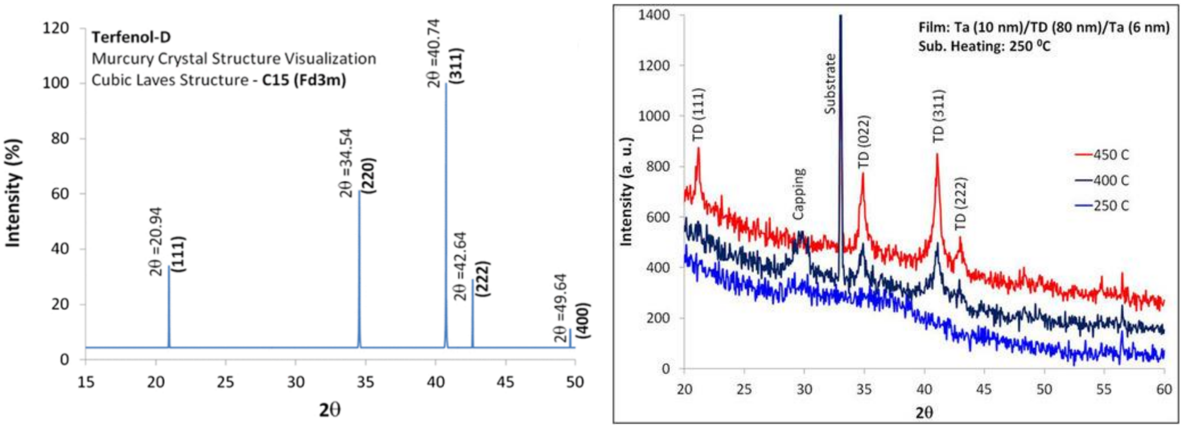

Figure 2.14. (a) Simulated XRD pattern of Terfenol-D single crystal (b) X-ray diffraction pattern of Terfenol-D thin films deposited on heated substrates at 250 ℃ and post-annealed for 4 hours at 250 ℃, 400 ℃ and 450 ℃.

The local microstructure of the film was imaged with a Scanning Transmission Electron Microscope (STEM) Titan (FEI) operating at 300 kV. Cross-sectional TEM samples were prepared by lift-off technique from films deposited on Silicon wafers using a Nova 600 dual beam Focused Ion Beam /Scanning Electron Microscope (FIB/SEM) which utilizes gallium ions at 0.5 nA current and an accelerating voltage of 10 kV. Prior to ion beam milling of the TEM samples, layers of Pt, both e-beam and ion-beam, were deposited to protect the film surface from high-energy ion beam damage. Figure 2.15 shows cross-sectional TEM micrographs of the 450 ℃ post-annealed films. The bright field image, shown in Fig. 2.15(a), clearly indicates a Si substrate, barrier Ta, Terfenol-D, capping Ta, and e-beam Pt from left to right. The Terfenol-D layer shows somewhat uniformly distributed crystalline grains throughout the thickness. The layer also exhibits regions of twinning commonly observed in strained FCC crystals. The micrograph also indicates a smooth Terfenol-D surface and the roughness of the film measured through Bruker Dimension Icon Scanning Probe Microscope is found to be ∼1 nm.

Figure 2.15(b) shows a dark field image of the sample obtained by selecting one of the strong Terfenol-D crystal spots from the selective area electron diffraction (SAED). This figure shows several strongly diffracting crystals oriented along the selected crystal direction. The average grain size is ∼30 nm, which is in good agreement with XRD results. Figure 2.15(c) shows high-resolution TEM (HRTEM) image taken at one crystal orientation. The Inset of Fig. 2.15(c) shows the diffraction pattern produced by Fast Fourier Transformation (FFT) of the selected area in the HRTEM image indicating reflections from several crystal planes, (111), (331) and (420), corresponding to FCC lattice of the Terfenol-D film. These results indicate that the films produced with substrate heating combined post-annealing are polycrystalline with FCC structures and relatively smooth surface [22].

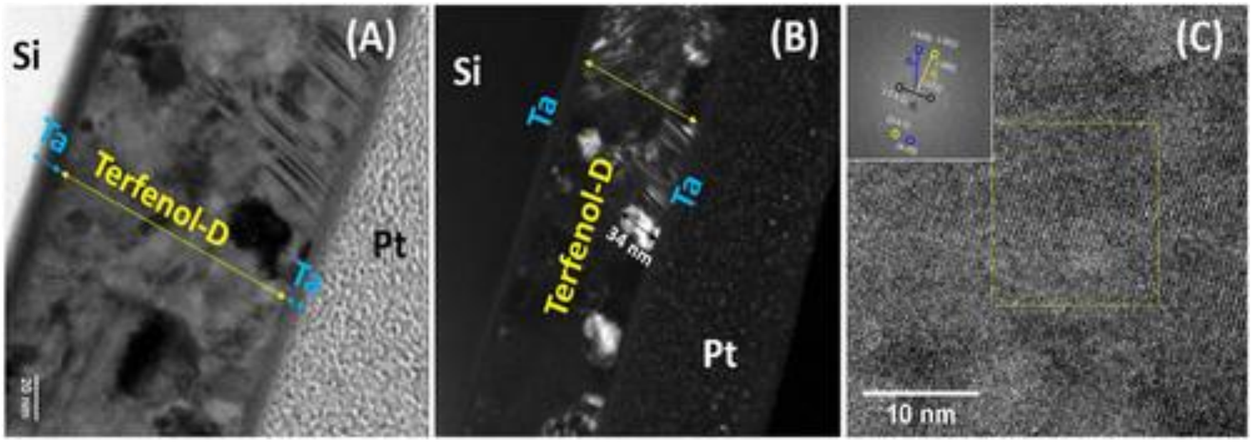

Figure 2.15. Cross sectional TEM micrographs of Terfenol-D thin film post annealed at 450 °C. (a) Bright field (b) Dark field and (c) HRTEM micrographs. FFT image is shown

2.2.2 Magnetic Characterization

The magnetic properties of the films are measured with Superconducting Quantum Interference Device (SQUID) from Quantum Design. The magnetoelastic response of the film is measured with a magneto-optic Kerr effect (MOKE) set-up combined with an ASTM standard four-point bending fixture producing both compressive and tensile loading.17 A bonded metallic strain gauge with 120 Ohm resistance is attached on the back of the substrate to measure the bending strain.

Figure 2.16 shows a room temperature in-plane magnetization versus applied magnetic field plot for the Terfenol-D film post-annealed at 450 ℃ using SQUID magnetometer. The measurements are made by sweeping the magnetic field from +8000 Oe to -8000 Oe and back. The saturation magnetization of the film is ~700 emu/cc close to the bulk Terfenol-D's M_s, 800 emu/cc [1] suggesting the hybrid crystallization process produces reasonable M_s. The slight differences may be caused by some intermixed regions at the Ta interfaces. The squareness of the hysteresis loop (M_r/M_s) is 0.85. The coercive field value is 2300 Oe suggesting a relatively hard magnetic material which is not representative of the soft bulk Terfenol-D. The large coercivity and remanence values are largely attributed to the intrinsic residual stresses that arise during the deposition process. While there is a small contribution from the thin film's shape anisotropy, this is insufficient to produce the large values measured. The residual stresses produce a large magnetoelastic induced in-plane easy plane producing both high coercivity and high remanence. While not shown here, the magnetic response is isotropic in the plane of the wafer while the out-of-plane direction is represented by a hard direction.

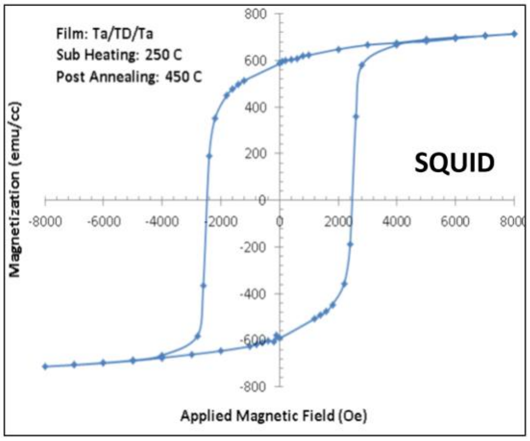

Figure 2.16. Magnetization vs. in-plane applied field plot of polycrystalline Terfenol-D film.

Figure 2.17 represents a temperature dependence of the magnetic properties of the polycrystalline Terfenol-D film. Multiple M-H curves are measured at 5 different temperatures (100, 150, 200, 250, 300 K) using SQUID. As the temperature decreases, the coercive field as well as the saturation magnetization increase. The coercive field changes from 2300 Oe at 300 K to 6200 Oe at 100 K and the saturation magnetization alters from 650 emu/cc at 300 K to 1000 emu/cc at 100 K. The right panel of Fig. 2.17 shows the variation of magnetization as a function of temperatures from 5 K to 400 K. For this measurement, the Terfenol-D sample is cooled from room temperature to 5 K without any magnetic field, and then, the magnetic moment under 300 Oe in-plane magnetic field is recorded as heating the sample from 5 K to 400 K. From ~40 K, the magnitude of magnetization linearly decreases as temperature increases. This linear change of magnetic moment as a function of temperature is a typical feature of ferrimagnetic materials [24].

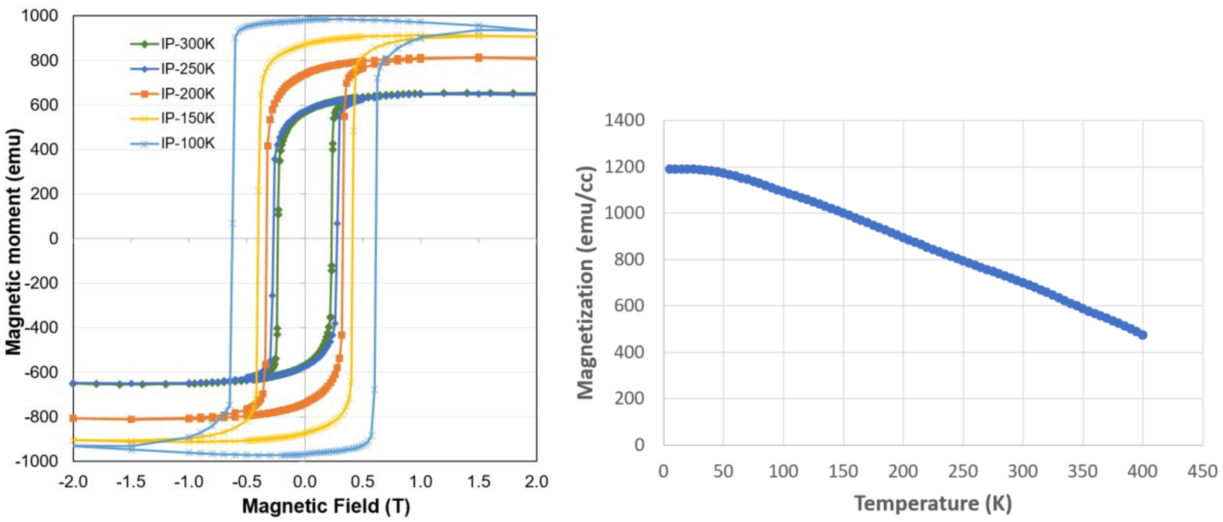

Figure 2.17. (Left) In-plane M-H curves measured at different temperatures from 100 K to 300 K. (Right) Magnetization versus temperature curve measured during heating from 5 K to 400 K under 300 Oe magnetic field after zero-field cooling from room temperature.

Figure 2.18 shows the MOKE hysteresis loops for the 450 ℃ post-annealed Terfenol-D film measured under both tensile and compressive strains. The hysteresis loop without an external strain (0 microstrain) shows a response similar to the SQUID data in Fig. 2.16. The right panel of Fig. 2.18 depicts the two different configurations of tensile or compressive strain applied through a 4-point bending fixture along with the magnetic field direction. The results show a tensile 600 microstrain increases the coercive field from 2300 Oe to 2700 Oe. Figure 2.18 also shows that the application of compressive strains produces opposite trends, i.e. the coercive field reduces and the remanent magnetization decreases. For the largest compressive strain (-1050 microstrain), the coercive field changes from 2300 Oe to 1700 Oe and the remanent magnetization changes from 0.83 to 0.55. This coercive field increase/decrease along with remanent magnetization changes are related to changes in the magnetoelastic energy which is proportional to $E = -\frac{3}{2}\lambda_S\sigma$, where σ is the applied stress along the magnetization direction. For tensile stresses, this increases the relative magnetic anisotropy energy while for compressive stresses it decreases the energy for this configuration. This is because Terfenol-D has a positive magnetostrictive constant. The coercivity change ΔH_c, applied strain ε, and saturation magnetostriction coefficient λ_s, can also be related by the energy balances defined by $\lambda_S \approx \frac{2\mu_0 M_S \Delta H_C}{3Y\Delta\varepsilon}$ [21,25] Where, μ_0 is the relative permeability, M_s and Y are the saturation magnetization and Young's modulus of the Terfenol-D film, respectively. This equation is obtained by equating the magnetoelastic energy with stress-induced uniaxial anisotropic energy, $\frac{H_K M_S}{2}$ and substituting $H_K = 2H_C$. Using the -1050 microstrain value, the calculated λs is 880 microstrains, i.e., a value similar to polycrystalline Terfenol-D.

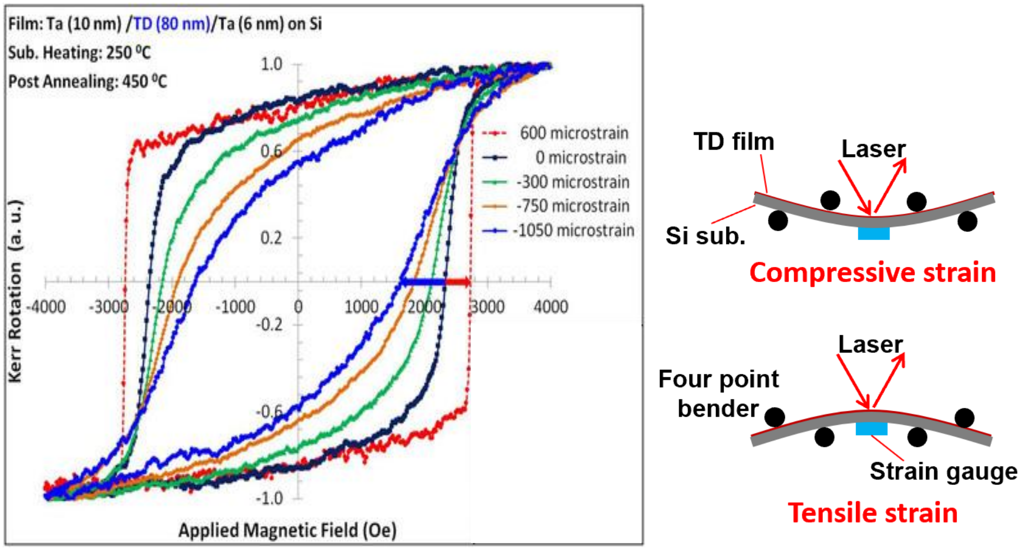

Figure 2.18. (Left) MOKE magnetization curves of the Terfenol-D thin film at different applied strains, both tensile and compressive (Right) A schematic of the four-point bending jig capable of applying tensile or compressive strains depending upon the film orientation. Strain gauges are attached to the backside of the sample measured the applied strain.

2.3 XMCD Measurement and Results

The polycrystalline Terfenol-D films deposited on single crystalline Sapphire substrates are used for X-ray absorption spectroscopy (XAS) and XMCD measurements. The tests are performed at a bend magnet beamline 6.3.1 at the Advanced Light Source (ALS) at Lawrence Berkeley National Laboratory (LBNL). Figure 2.19 shows the beamline facilities, the samples mounted on luminescence holder, and the CCD image of the samples installed in the vacuum chamber. The Terfenol-D films deposited on Sapphire are chosen since the transmission (luminescence) mode is used in this investigation to reflect the properties of full film stack (~70 nm) (see Fig. 2.10). Sapphire substrates emit visible light when exposed to X-ray and the emission from the back-side of the samples is recorded. The samples are cut into small pieces (6-8 mm × 6-8 mm) and mounted on the luminescence holder of which photo detectors are installed on the back side (see Fig. 2.19(a)). Then, the holder is installed between two magnet poles in the vacuum chamber. A small hole is placed at the center of the magnet pole to allow an incident X-ray beam coming (see Fig. 2.19(c)).

The X-ray with a spot size of ~150 × 60 μm is incident on the Terfenol-D film surface. For the XAS & XMCD measurements, the incident light energies are scanned from 690 to 750 eV for Fe $L_{2,3}$ edges, from 1210 to 1290 eV for Tb $M_{4,5}$ edges, and from 1280 to 1360 eV for Dy $M_{4,5}$ edges and the corresponding luminescence yield signals from the backside of the samples are recorded. During the scans, +1 or -1 T magnetic fields are applied in-plane to saturate the films and the polarization of the incident light was fixed. In the measured M-H curves of the Terfenol-D films (see Fig. 2.17), the coercive fields are ~2400 Oe at room temperature and ~6200 Oe at 100 K, which is way below than 1 T. So, the XMCD measurements can be reasonably assumed that the films magnetic moments are saturated in each positive or negative direction. Each scan is repeated 8 times and normalized by the corresponding I0ES data to exclude any time-dependent scanning errors. The average of the scans under positive and negative magnetic fields is taken as XAS and the difference of them as XMCD. The chamber temperature is controlled using a liquid Nitrogen and heating unit, and the measurements are performed in five different temperatures down to 100 K.

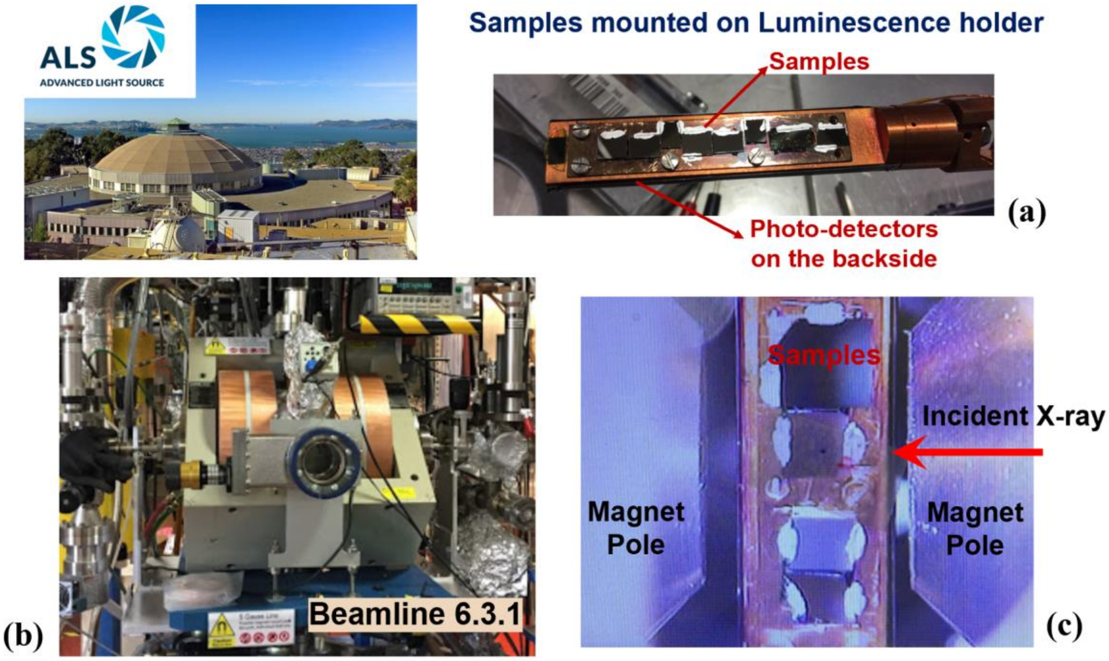

Figure 2.19. Beamline 6.3.1 facilities at Advanced Light Source (ALS) at Lawrence Berkeley National Laboratory (LBNL) and the samples mounted on the luminescence holder.

Figure 2.20 represents one of XAS & XMCD results measured in Dy $M_{4,5}$ edges at 100 K. There are two main peaks on XAS curve (blue line) and two main dips on XMCD curve (orange line). Each peak (dip) is corresponding to the M_5 and M_4 edges. The energy level occurring the M_5 (1294 eV) and M_4 (1329 eV) edges are characteristic for 3d → 4f transitions in Dy element. The

XMCD dips represent the Dy elements in the Terfenol-D films are magnetic and the dip intensity is relative to the magnitude of the Dy elemental magnetic moment.

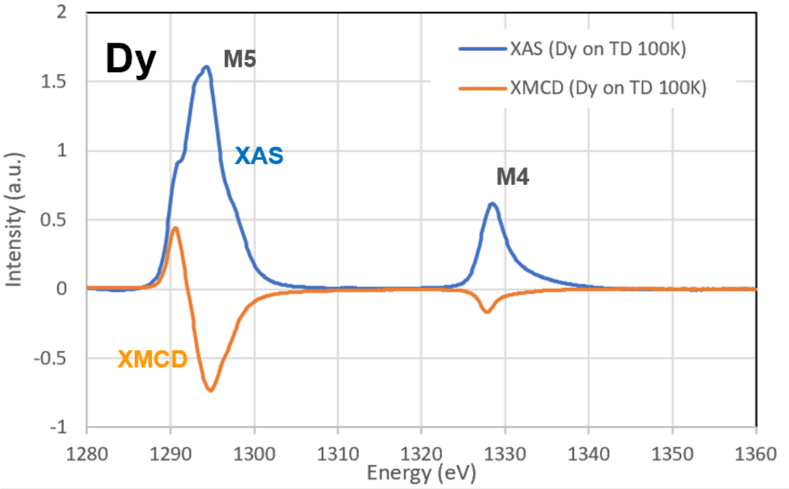

Figure 2.20. A representative XAS & XMCD data measured for Dy $M_{4,5}$ edges at 100 K.

While the XMCD measurements are performed under two saturating magnetic fields (+1 T & -1 T), the magnetic fields can be swept, and the X-ray energy can be fixed at the characteristic level (i.e. M_5 or M_4). Then, thanks to the relativeness between the XMCD dip intensity and the elemental magnetic moment, the element-specific magnetic hysteresis loops can be acquired. The elemental M-H loops are recorded for Tb, Dy, and Fe edges. In this measurement, two specific energies are selected to get the prominent difference in XMCD (i.e. one dip & one peak, or one dip & one pre-edge). Then, the magnetic field is swept in each energy level from -1.8 T to +1.8 T and the signal difference between two energy levels are taken to plot the elemental hysteresis loop. The representative elemental hysteresis loops (Tb, Dy, and Fe) measured at 100 K are shown in Fig. 2.21 with an alloy M-H curve measured in SQUID for comparison.

As can be seen in the figure, the M-H loops from Dy and Tb elements measured by XMCD look almost the same as the one by a SQUID, showing similar coercive field and remanence magnetic moment values. On the other hand, the curve for Fe is completely reversed to the opposite direction. This feature indicates two important things. The first is the ferrimagnetic property of the Terfenol-D film with antiferromagnetic coupling between Tb/ Dy and Fe. The second is that Tb/ Dy atoms have a major magnetic contribution to the alloy material, and Fe a minor one (rare earth-dominant ferrimagnet). This can be confirmed because the polarity of Tb and Dy M-H curves follow the polarity of the net alloy curve.

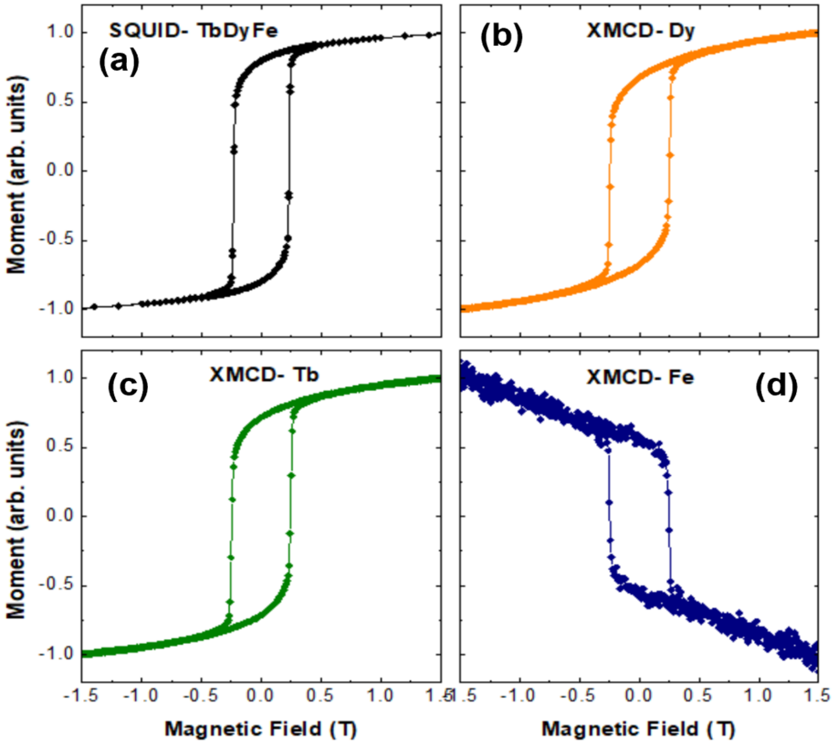

Figure 2.21. (a) M-H result of Terfenol-D film measured by SQUID magnetometer.
(b-d) Element specific M-H loops measured by scanning magnetic field at each element’s (Dy, Tb, and Fe) characteristic peaks on XMCD.

Figures 2.22, 2.23. and 2.24 show the XAS and XMCD curves measured at different temperatures for Dy, Tb, and Fe, respectively. The blue lines in (a-e) are XAS, averaged curves of the positive and negative magnetic field measurements. The orange lines in (a-e) are XMCD, the difference of the XAS under the positive and negative magnetic fields. The last panels of the figures (Figs. 2.22(f), 2.23(f), and 2.24(f)) are the plots for the XMCD peaks' intensity over the XAS peaks, which represents relatively how much elemental magnetic moments exist in the Terfenol-D film as a function of temperature.

The Dy XMCD signal at the M_5 and M_4 edges both show the dips in Fig. 2.22. This means that the XAS responses from the magnetic fields are along the same polarity in two edges, which is different from the XMCD in $L_{2,3}$ edges of usual transition metals [17,26]. In Fig. 2.22(f), the Dy M_5 and M_4 XMCD peak intensities divided by the corresponding XAS peaks decrease as temperature goes up. The ratio between M_5 and M_4 is fairly maintained through the temperature range. On the other hand, the Tb XMCD signal in Fig. 2.23 shows one prominent dip and one small bump through all temperatures. For the XMCD peak intensities in Fig. 2.23(f), M_4 edge bump heights are much smaller than the M_5 edge dip depths. And unlike Dy, the changes in peaks depending on temperature are very small. A rare change in magnetic moments of Tb is expected as a function of temperature.

The Fe XAS curves in Fig. 2.24 have a quite different shape from the previous rare earth elements. The levels of the horizontal baseline at pre-edge and post-edge are not matched with each other. This is neither from a measurement error or from a structural peculiarity, but from white line X-ray intensity, which is a typical characteristic of 3d transition metals [11]. The XMCD signals for Fe seem very small relative to Tb and Dy ones. The reason for this weakness is not understood yet, but the fact that Fe magnetic moments are minor in this Terfenol-D film might bring into the weak signals.

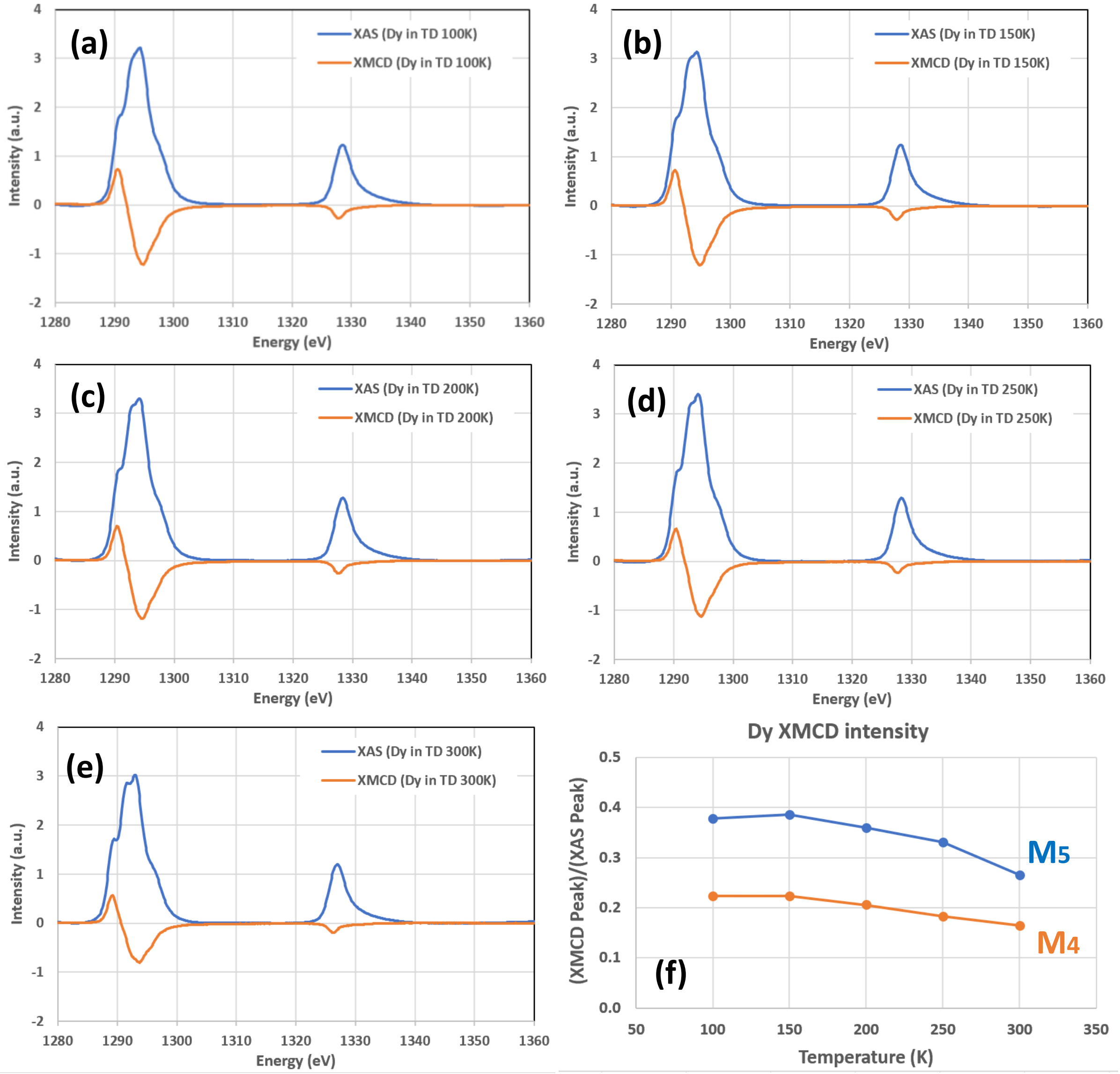

Figure 2.22. (a-e) XAS and XMCD results measured in the energy range to cover Dy M$_5$ and M$_4$ edges (1280 – 1360 eV) at 5 different temperatures; 100, 150, 200, 250, and 300 K, respectively. (f) M$_{4,5}$ XMCD peak intensities over the XAS peaks as a function of temperature.

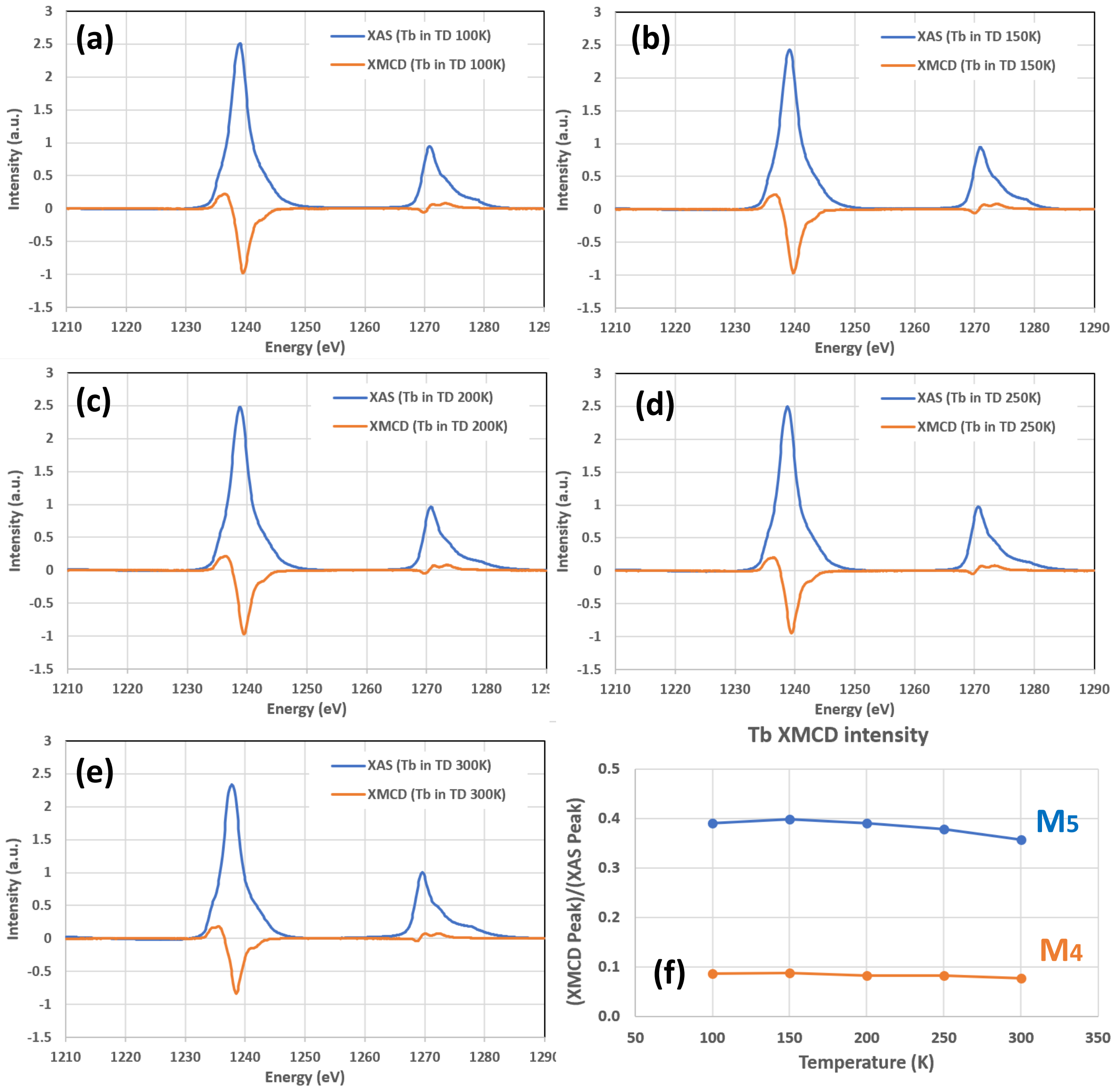

Figure 2.23. (a-e) XAS and XMCD results measured in the energy range to cover Tb M_5 and M_4 edges (1210 – 1290 eV) at 5 different temperatures; 100, 150, 200, 250, and 300 K, respectively. (f) $M_{4,5}$ XMCD peak intensities over the XAS peaks as a function of temperature.

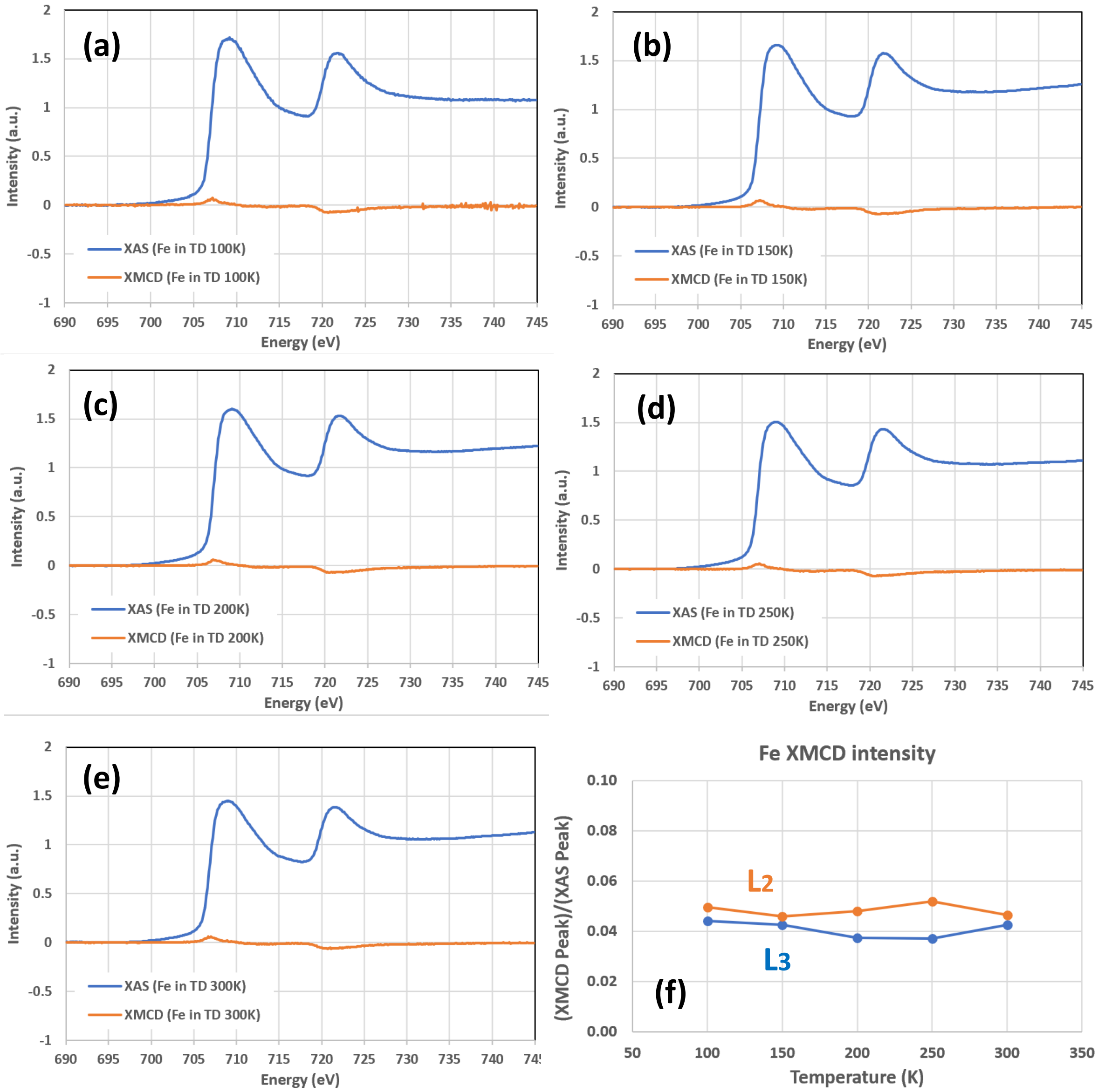

Figure 2.24. (a-e) XAS and XMCD results measured in the energy range to cover Fe L_3 and L_2 edges (690 – 745 eV) at 5 different temperatures; 100, 150, 200, 250, and 300 K, respectively. (f) $L_{2,3}$ XMCD peak intensities over the XAS peaks as a function of temperature.

2.4 Sum Rules Analysis : Orbital & Spin Magnetic Moment

Optical sum rules, in general, are very useful theoretical results. In 1992, Thole et al. found a sum rule that could be applied to X-ray magnetic circular dichroism (XMCD) signals in ferromagnets [13]. This first magnetic sum rule states that the integrated dichroic signal is proportional to the ground-state expectation value of the operator L_z acting on the shell that receives the photoelectron in the final state. In 1993, a second sum rule, the spin sum rule, was proposed [14]. It relates a linear combination of the XMCD signals at the core split edges to the average values of two operators (S_z and T_z) acting on the shell that receives the photoelectron in the final state.

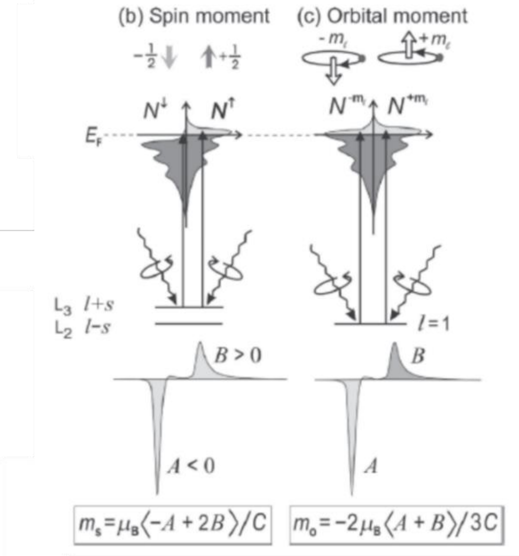

Figure 2.25. Schematic of processes, spectra, and intensities underlying the quantitative determination of valence band properties such as the spin moment m_s and orbital moment m_o [4].

Figure 2.26 shows the representative XAS and XMCD curves for Dy and Tb $M_{5,4}$ edges measured at 100 K, and the orange curves on each panel are their integration curves drawn for the sum rules calculation. As can be seen, the signs of Dy XMCD peaks at $M_{5,4}$ edges are the same (both negative) while the signs of Tb are opposite each other (negative for M_5 and positive for M_4). Hence, the corresponding integral curves of the XMCD also look different. This different XMCD results directly influence in the elemental orbital and spin moments calculated by sum rules.

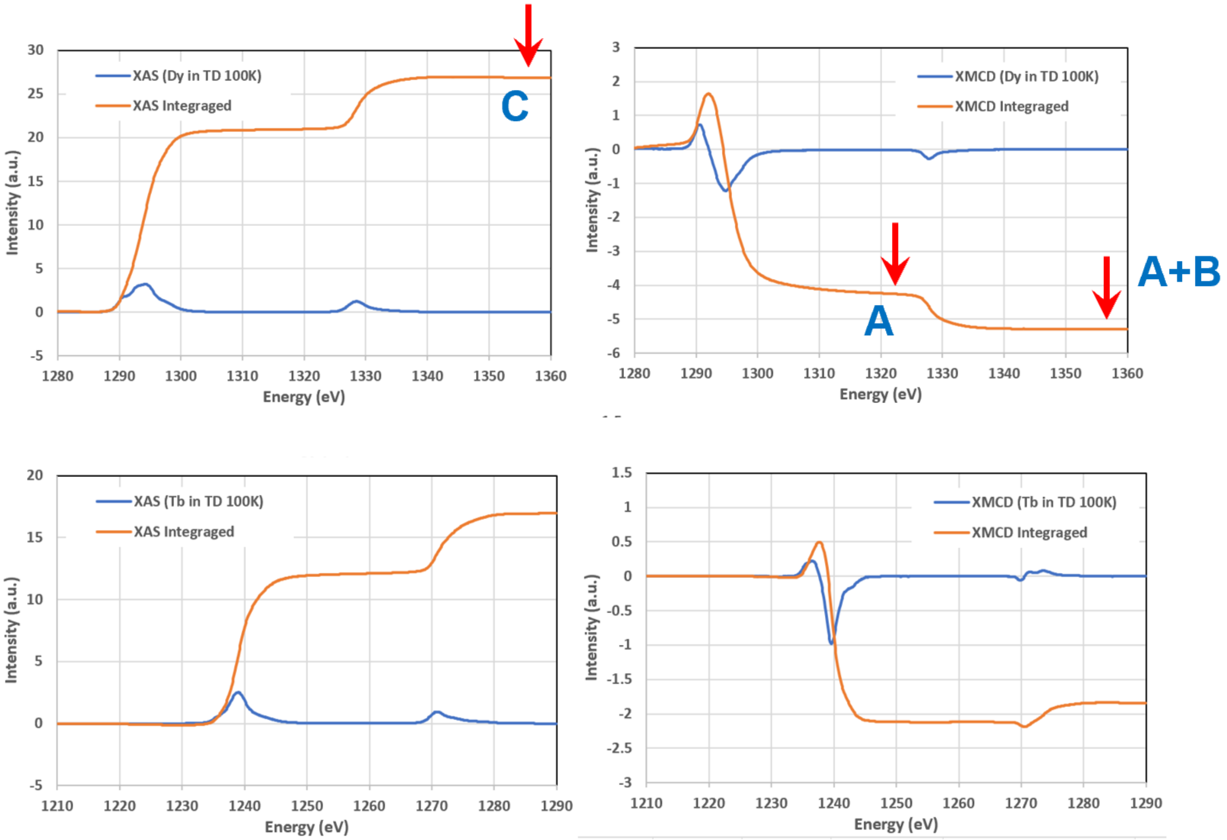

Figure 2.26. (Left) Representative XAS (blue) and its integral plots (orange) for Dy (top) and Tb (bottom) measured at 100 K. (Right) Representative XMCD (blue) and its integral plots (orange) for Dy (top) and Tb (bottom) measured at 100 K. The definition of integrals of A, A+B, and C is marked with arrows for easy understanding.

The sum rule equation for an orbital moment from the original reference appeared like below.

$$\rho \equiv \frac{\int_{edge}\big(\mu_+(\omega) - \mu_-(\omega)\big)d\omega}{\int_{edge}\big(\mu_+(\omega) + \mu_-(\omega) + \mu_0(\omega)\big)d\omega} = \frac{1}{2}\frac{c(c+1) - l(l+1) - 2}{l(l+1)(4l+2-n)}\langle L_z\rangle$$

, where (4l+2-n) is the number of holes in the valence shell, c denotes a core hole, and $\langle L_z \rangle$ is an orbital operator [13]. The equation for a spin moment from the reference, which is modified for 4f rare earth elements is represented by

$$X_I(M_5) - \frac{3}{2} X_I(M_4) = \frac{2}{3(14-n)} \langle S_z \rangle + \frac{2}{14-n} \langle T_z \rangle$$

, where $I = \int_{M_5+M_4} \big(\mu_+(\omega) + \mu_0(\omega) + \mu_-(\omega)\big) d\omega,$

$$X_I(M_5)\big(or\ X_I(M_4)\big) = \frac{\int_{M_5\ (or\ M_4)} \big(\mu_+(\omega) - \mu_-(\omega)\big) d\omega}{I}$$

, $\langle S_z \rangle$ and $\langle T_z \rangle$ is spin and dipole operators, respectively [14]. Then, the corresponding parameters are plugged into the equations, and some simplifications are followed by to make it easier to be understood on the XMCD and XAS plots in Fig. 2.26. The simplified equation for orbital (m_{orb}) and spin moments (m_{spin}) are

$$m_{orb} = \langle L_z \rangle = \frac{-2(A+B)}{C} (14 - n_{4f})$$

$$m_{spin} = 2\langle S_z \rangle = \frac{-5A + 3(A+B)}{2C} \big(14 - n_{4f}\big) - 3\langle T_z \rangle$$

, where n_{4f} is the number of electrons on 4f orbital of trivalent rare earth ions. A, B, C and (A+B) are the parameters that can be extracted from the integrated XMCD and XAS peaks like below equations, and they are marked on the XMCD & XAS data in Fig. 2.26 for easy understanding.

$$A = \int_{M_5} (\mu_+(\omega) - \mu_-(\omega)) d\omega, \qquad B = \int_{M_4} (\mu_+(\omega) - \mu_-(\omega)) d\omega$$

$$A + B = \int_{M_5+M_4} (\mu_+(\omega) - \mu_-(\omega)) d\omega$$

$$C = \int_{M_5+M_4} (\mu_+(\omega) + \mu_-(\omega))d\omega$$

For this sum rule expressions, the isotropic XAS term, $\mu_0(\omega)$ is assumed as $\frac{1}{2}(\mu_+(\omega) + \mu_-(\omega))$. And, note that the sum rule equations for orbital and spin moments are modified for rare earth from the originally proposed ones [13,27,28]. The corresponding number of 4f orbital electrons is determined as 9 for Dy^{3+} and 8 for Tb^{3+}, and the estimated value of dipole operator $\langle T_z \rangle$ is 0.128 for Dy^{3+} and 0.243 for Tb^{3+} as summarized in Fig. 2.27 [27].

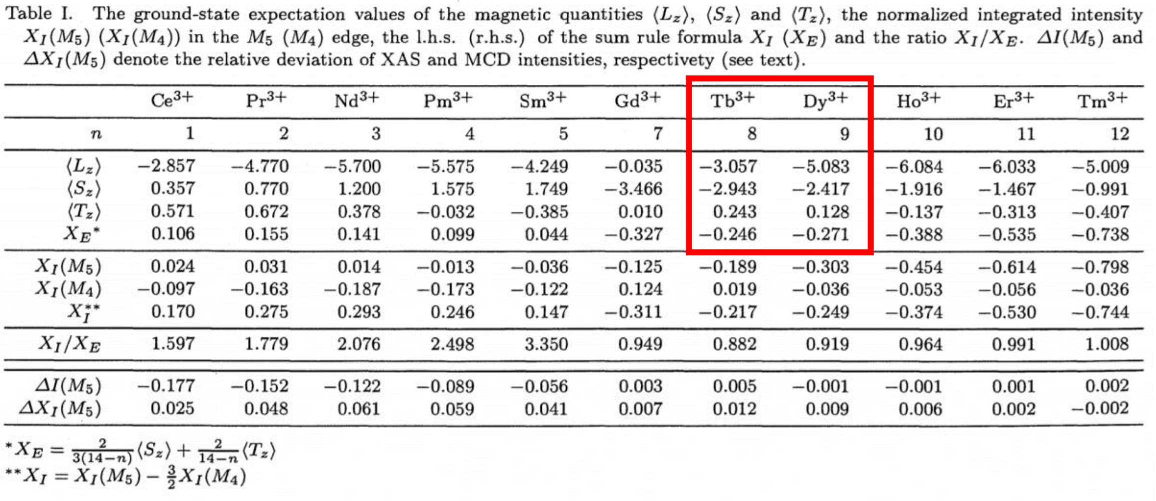

Table I. The ground-state expectation values of the magnetic quantities $\langle L_z \rangle$, $\langle S_z \rangle$ and $\langle T_z \rangle$, the normalized integrated intensity $X_I(M_5)$ ($X_I(M_4)$) in the M_5 (M_4) edge, the l.h.s. (r.h.s.) of the sum rule formula X_I (X_E) and the ratio X_I/X_E. $\Delta I(M_5)$ and $\Delta X_I(M_5)$ denote the relative deviation of XAS and MCD intensities, respectivety (see text).

	Ce^{3+}	Pr^{3+}	Nd^{3+}	Pm^{3+}	Sm^{3+}	Gd^{3+}	Tb^{3+}	Dy^{3+}	Ho^{3+}	Er^{3+}	Tm^{3+}
n	1	2	3	4	5	7	8	9	10	11	12
$\langle L_z \rangle$	−2.857	−4.770	−5.700	−5.575	−4.249	−0.035	−3.057	−5.083	−6.084	−6.033	−5.009
$\langle S_z \rangle$	0.357	0.770	1.200	1.575	1.749	−3.466	−2.943	−2.417	−1.916	−1.467	−0.991
$\langle T_z \rangle$	0.571	0.672	0.378	−0.032	−0.385	0.010	0.243	0.128	−0.137	−0.313	−0.407
$X_E{}^*$	0.106	0.155	0.141	0.099	0.044	−0.327	−0.246	−0.271	−0.388	−0.535	−0.738
$X_I(M_5)$	0.024	0.031	0.014	−0.013	−0.036	−0.125	−0.189	−0.303	−0.454	−0.614	−0.798
$X_I(M_4)$	−0.097	−0.163	−0.187	−0.173	−0.122	0.124	0.019	−0.036	−0.053	−0.056	−0.036
X_I^{**}	0.170	0.275	0.293	0.246	0.147	−0.311	−0.217	−0.249	−0.374	−0.530	−0.744
X_I/X_E	1.597	1.779	2.076	2.498	3.350	0.949	0.882	0.919	0.964	0.991	1.008
$\Delta I(M_5)$	−0.177	−0.152	−0.122	−0.089	−0.056	0.003	0.005	−0.001	−0.001	0.001	0.002
$\Delta X_I(M_5)$	0.025	0.048	0.061	0.059	0.041	0.007	0.012	0.009	0.006	0.002	−0.002

$^*X_E = \frac{2}{3(14-n)}\langle S_z \rangle + \frac{2}{14-n}\langle T_z \rangle$

$^{**}X_I = X_I(M_5) - \frac{3}{2}X_I(M_4)$

Figure 2.27. Key parameters used in sum rule calculations [27].

The calculated results from the sum rules are shown in Fig. 2.28. Total, spin, and orbital moments for Dy and Tb as a function of temperature are plotted in Fig. 2.28(a) and (b), respectively. The total moments of Dy and Tb at low temperature (3.69 μ_B/atom and 4.56 μ_B/atom) are measured smaller than them from pure Dy and Tb crystals. But, at room temperature, the total moments still have finite values (2.89 μ_B/atom and 4.04 μ_B/atom) while pure Dy and Tb crystals have no magnetic moments (i.e. T_c < 300 K). The split between orbital and spin moments shows quite different results between Tb and Dy. For Tb, spin moments definitely have major contributions to the total moments (orbital moment: 25~29 %) at all temperatures. For Dy, the contributions from spin and orbital moments (orbital moment: 48~54 %) are comparable through the temperature. Upon that most ferromagnetic transition metals have only up to 10 % of orbital moment contribution, the orbital moments on Dy are remarkable results attributed to the strongly bounded 4f orbital and corresponding large spin-orbit coupling.

Figure 2.28(c,d) shows orbital and spin moments change depending on the temperature for Dy and Tb. As mentioned previously, Dy shows higher orbital moment than Tb at all temperatures while the spin moments of Dy are much smaller than Tb. For the temperature dependence, only the Dy orbital moment shows a noticeable change from 2.10 μ_B/atom to 1.39 μ_B/atom. This orbital moment change will have an impact on the magnitude of spin-orbit coupling in Dy and eventually magnetic properties in Terfenol-D.

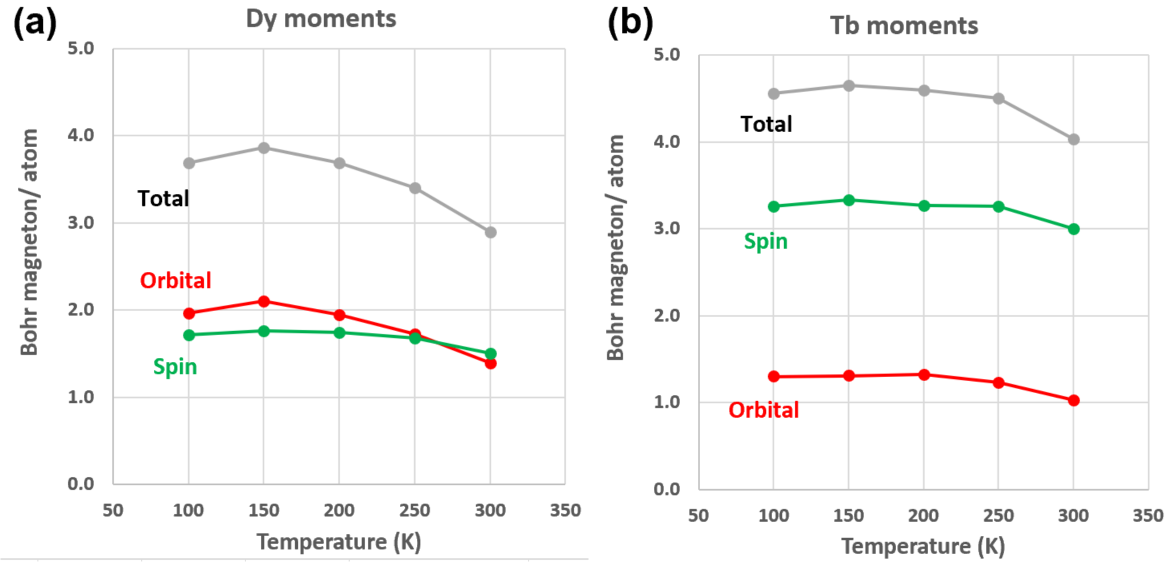

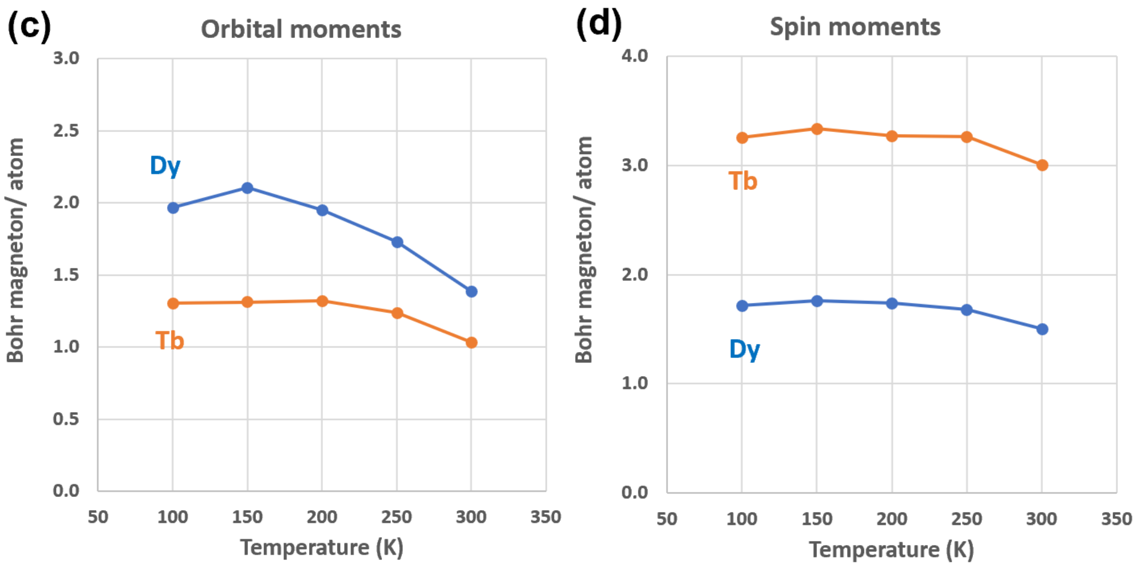

Figure 2.28. The elemental magnetic moments of the Terfenol-D film as a function of temperature calculated using XMCD sum rules. (a,b) Total, spin, and orbital magnetic moments for Dy and Tb, respectively (c) Orbital moments for Dy and Tb. (d) Spin moments for Dy and Tb.

In order to figure out the connection between the change of Terfenol-D property and the elemental orbital moments, the coercive field change as a function of temperature is plotted in Fig. 2.29. Since four different sets of M-H loops are available from Terfenol-D (by SQUID), Tb, Dy, and Fe (element-specific ones from XMCD), there are four plots for the coercive field change in Fig. 2.29. As expected, the four plots have the same tendency and almost overlap each other. The plots show that as temperature decreases, the coercive field exponentially increases, which means that the magnetic anisotropy of Terfenol-D film enormously increases. However, it cannot be presumed that the anisotropy change of the Terfenol-D film is purely attributed to the crystalline anisotropy change.

Another factor that affects on the coercive field (or anisotropy) is the thermal expansion mismatch between the Sapphire substrate and Terfenol-D film. As temperature decreases from room temperature, both of Sapphire substrate and Terfenol-D film will shrink based on their own coefficients of thermal expansion (CTE). Since the CTE of Terfenol-D (14 × 10^{-6} Ɛ/K) is larger than Sapphire (0.3~3.4 × 10^{-6} Ɛ/K), the thin film Terfenol-D (~70 nm) on thicker (0.5 mm) Sapphire substrate experiences tensile strain as temperature goes down. This tensile strain, induced by thermal expansion mismatch, will add magnetoelastic anisotropy to the Terfenol-D film (λ_S = 880 μƐ). The estimated coercive field change from the thermally induced magnetoelastic anisotropy is calculated using the below equations.

$$\varepsilon_{th} = (\alpha_{Sap}(T) - \alpha_{TD}) \cdot \Delta T$$

$$E_{me} = \frac{3}{2}\lambda_S \cdot Y \cdot \varepsilon_{th} \cong \Delta H_C \cdot M_S(T) \qquad (\because H_K \cong 2H_C)$$

, where ε_{th} is the strain induced by thermal expansion mismatch, α_{Sap} and α_{TD} are the CTE of Sapphire and Terfenol-D, respectively, E_{me} is the induced magnetoelastic anisotropy energy, and Y is Young's modulus of Terfenol-D. The calculation results are plotted (pink solid line) along with the experimentally measured coercive field change in Fig. 2.29. As can be seen, even after ruling out the effect from thermally induced magnetoelastic anisotropy, there seems large coercive field change as temperature decreases.

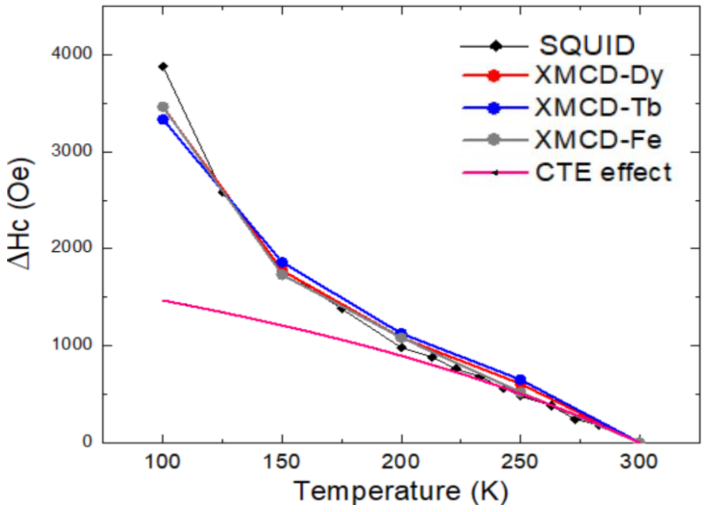

Figure 2.29. Coercive field change from room temperature. SQUID data measured in Terfenol-D film and Tb, Dy, Fe-XMCD data extracted from their element-specific M-H loops. The estimated coercive field change by thermal expansion mismatch is calculated and plotted as a pink line.

Now, it can be assured that the remaining change of coercive field (or magnetic anisotropy) of Terfenol-D film is originated from the orbital moment change as a function of temperature. Remind that the only noticeable change in orbital moment appeared in Dy. So, the increased Dy orbital moment at low-temperature results in a higher spin-orbit coupling and enhanced magneto-crystalline anisotropy of Terfenol-D film eventually. Figure 2.30 plots the orbital moment difference between Dy and Tb (i.e. m_{orb}(Dy)–m_{orb}(Tb)). The difference linearly increases as temperature decreases. This plot explains the temperature dependence of the crystalline anisotropy of Terfenol-D film. The difference in orbital moments is minimized at room temperature, which confirms that the crystalline anisotropies from $TbFe_2$ and $DyFe_2$ are successfully compensated each other as intended. As temperature goes down, Dy orbital moment increases while Tb relatively stays still. As a result, the uncompensated crystalline anisotropy (and coercive field) of Terfenol-D film is enormously increased at low temperature due to the enhanced spin-orbit coupling of Dy.

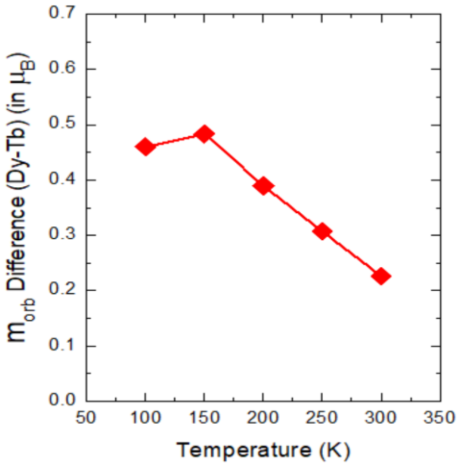

Figure 2.30. The orbital moment difference between Dy and Tb as a function of temperature.

2.5 Chapter References

1] G. Engdahl, Handbook of Giant Magnetostrictive Materials, Academic Press (2000)

2] J. D. Rinehart, and J. R. Long, Chemical Science **2**, 2078 (2011)

3] A. E. Clark, and H. S. Belson, Phys. Rev. **B5**, 3642 (1972)

4] A. Speliotis, O. Kalogirou, and D. Niarchos, J. Appl. Phys. **81**, 5696 (1997).

5] E. Quandt, B. Gerlach, and K. Seemann, J. Appl. Phys. **76**, 7000 (1994).

6] L. Rebouta, P. Martins, S. Lanceros-Mendez, J. M. Barandiaran, J. Gitoerrez, L. C. Alves, and E. Alves, Trans Tech Publications, Switzerland, J Nano R **18-19**, 235 (2012)

7] F. Schatz, M. Hirscher, M. Schnell, G. Flik, and H. Kronmuller, J. Appl. Phys. **76**, 5380 (1994).

8] A. Speliotis and D. Niarchos, Sensors and Actuators A, **106**, 298 (2003).

9] P. I. Williams, D. G. Lord, and P. J. Grundy, J. Appl. Phys. **75**, 5257 (1994)

10] G. van der Laan, and A. I. Figueroa, Coordination Chemistry Reviews, **277–278**, 95 (2014)

11] J. St¨ohr and H.C. Siegmann, Magnetism: From Fundamentals to Nanoscale Dynamics, Springer (2006)

12] S. Pizzini, Ecole Franco-Roumaine : Magnétisme des systèmes nanoscopiques et structures hybrids, **V.5**, 1 (2003)

13] B. T. Thole, P. Carra, F. Sette, G. van der Laan, Phys. Rev. Lett. **68**, 1943 (1992)

14] P. Carra, B. T. Thole, M. Altarelli, X. Wang, Phys. Rev. Lett. **70**, 694 (1993)

15] B. T. Thole, G. van der Laan, Phys. Rev. B, **38**, 3158 (1988)

16] G. van der Laan, B.T. Thole, Phys. Rev. Lett. **60**, 1977 (1988)

17] K. Chen, D. Lott, F. Radu, F. Choueikani, E. Otero, and P. Ohresser, Sci. Rep. **5**, 18377 (2015)

18] C. T. Chen, Y. U. Idzerda, H. J. Lin, N. V. Smith, G. Meigs, E. Chaban, G. H. Ho, E. Pellegrin, and F. Sette, Phys. Rev. Lett. **75**, 152 (1995)

19] C.A.F. Vaz, C. Moutafis, M. Buzzi, J. Raabe, J. Electron Spectrosc. Relat. Phenom. **189**, 1 (2013)

20] L. R. Shelford, T. Hesjedal, L. Collins-McIntyre, S. S. Dhesi, F. Maccherozzi, and G. van der Laan, Phys. Rev. B, **86**, 081304(R) (2012)

21] K. P. Mohanchandra, S. V. Prikhodko, K. P. Wetzlar, W. Y. Sun, P. Nordeen, and G. P. Carman, AIP Advances, **5**, 097119 (2015)

22] K. P. Mohanchandra, T. Lee, A. Chavez, S. V. Prikhodko, and G. P. Carman, AIP Advances, **8**, 056404 (2018)

23] P. Scherrer and G. Nachrichten, Math. Phys. **2**, 98 (1918).

24] B. D. Culity, and C. D. Graham, Introduction to Magnetic Materials, Second Edition, Wiley (2008)

25] A. Bur, T. Wu, J. Hockel, C.-J. Hsu, H. K. D. Kim, T.-K. Chung, K. Wong, K. L. Wang, and G. P. Carman, J. Appl. Phys. **109**, 123903 (2011).

26] C. T. Chen, Y. U. Idzerda, H.-J. Lin, N. V. Smith, G. Meigs, E. Chaban, G. H. Ho, E. Pellegrin, and F. Sette, Phys. Rev. Lett. **75**, 152 (1995)

27] Y. Teramura, A. Tanaka, B. T. Thole, and T. Jo, J. Phys. Soc. Jpn, **65**, 3056 (1996)

28] F. Bondino, C. Cepek, N. Tagmatarchis, M. Prato, H. Shinohara, and A. Goldoni, J. Phys. Chem. B, **110**, 7289-7295 (2006)

3. Strain-Modulated Exchange Spring Magnet

3.1 Introduction

3.1.1 Exchange Spring Magnet

An exchange spring magnet (ESM) means a system which comprises both hard and soft magnetic materials, which take advantage of high coercivity and high saturation magnetization simultaneously to enhance the $(BH)_{\max}$ value for the permanent magnet application [1]. This behavior can be achieved through the ferromagnetic exchange coupling between the hard and soft magnetic layers as schematically explained in Fig. 3.1. The magnetic moments near the interface in the soft magnetic layer are pinned by the moments of the hard magnetic layer and pointing the opposite direction to the applied magnetic field direction. The moments far from the interface, on the other hand, follow to the magnetic field direction, making the moments in soft magnetic layer look like a rotating "spring".

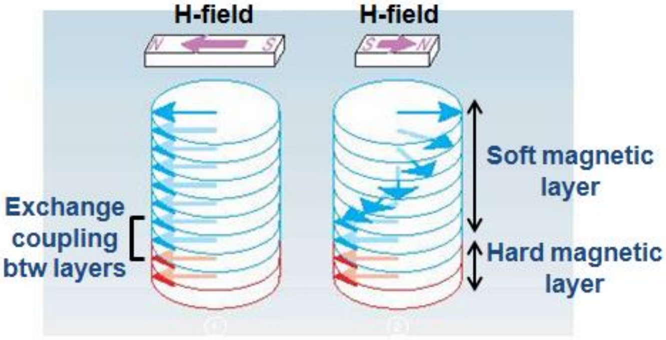

Figure 3.1. Schematic figure of exchange spring magnet behavior. The soft and hard magnetic layers are exchange coupled at the interface to enhance $(BH)_{\max}$ values.

Other than this initial purpose, the unique negative coercive-field *M-H* behavior results can be observed by using the antiferromagnetically exchange-coupled ferrimagnet-ferromagnet multilayer system, i.e. DyFe$_2$/YFe$_2$, [2]. The negative coercivity behavior represents that a magnetic layer is already switched to the opposite direction to the previously saturated one before a magnetic field reaches zero. This abnormal feature is used in this research to achieve a magnetic switching by applying strain to the system.

The first paper, which named ESM is published in 1991 by Kneller and Hawig. The initial purpose was to enhance $(BH)_{\mathrm{max}}$ value for the permanent magnet. They made hard magnetic Nd$_2$Fe$_{14}$B precipitate inside the soft magnetic Fe$_2$B$_6$ matrix to take advantage of both high M_S of a soft matrix and high H_C of a hard precipitate. The results are M_S= 1356 emu/cc, M_r/M_S= 0.76, H_C= 3637 Oe, and $(BH)_{\mathrm{max}}$= 105 kJ/m^3 [1]. Besides this, another peculiarity of exchange spring magnet is their reversible demagnetizing behavior before the hard magnetic component switching. In the schematic *M-H* loops in Fig. 3.2, the solid line represents a reversible minor loop and the dotted line represents the irreversible minor loop. As we can see, in exchange spring, the reversible region expands up to the certain negative magnetic field.

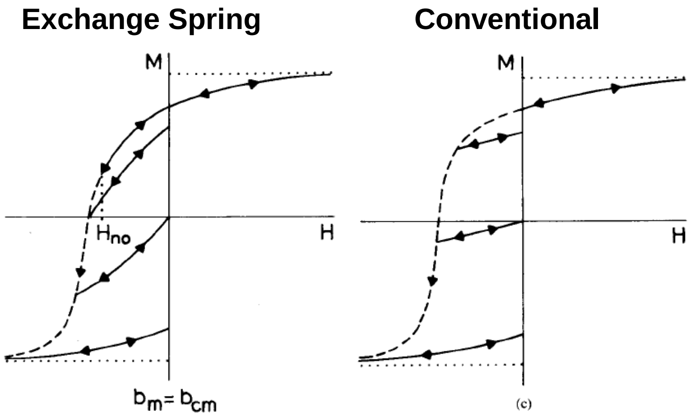
Exchange Spring **Conventional**

Figure 3.2. The schematic demagnetization curves and several minor loops representing the difference between exchange spring and conventional ferromagnet appeared in the first paper of exchange spring magnet. The solid lines represent a reversible demagnetizing behavior, and the dotted lines represent an irreversible one [1].

Since the first exchange spring magnet paper, many related papers have been published for the permanent magnet application. Fullerton has been showing a thin-film type exchange spring magnet with using SmCo/Fe(Co) bilayer system since 1998. He first used a ferromagnetically exchange-coupled SmCo/Fe bilayer system to increase $(BH)_{\max}$ value for the permanent magnet application, and at a proper range of Fe thickness, the $(BH)_{\max}$ value increased about five times than a SmCo single layer as you can see in the left graph of Fig. 3.3 [3]. The reference paper, shown in the right panel of Fig. 3.3, also talked about enhancing $(BH)_{\max}$ with using thin-film bilayer structure, but they tried to understand the exchange spring magnet mechanism as changing soft magnetic layer thickness [4]. In the thicker Fe sample, Fe moment rotation starts earlier from 0.09 T. So, two-step demagnetization behavior appeared as shown in Fig. 3.3. This can be analyzed by the ferromagnetic exchange coupling restricted near the interface region [5].

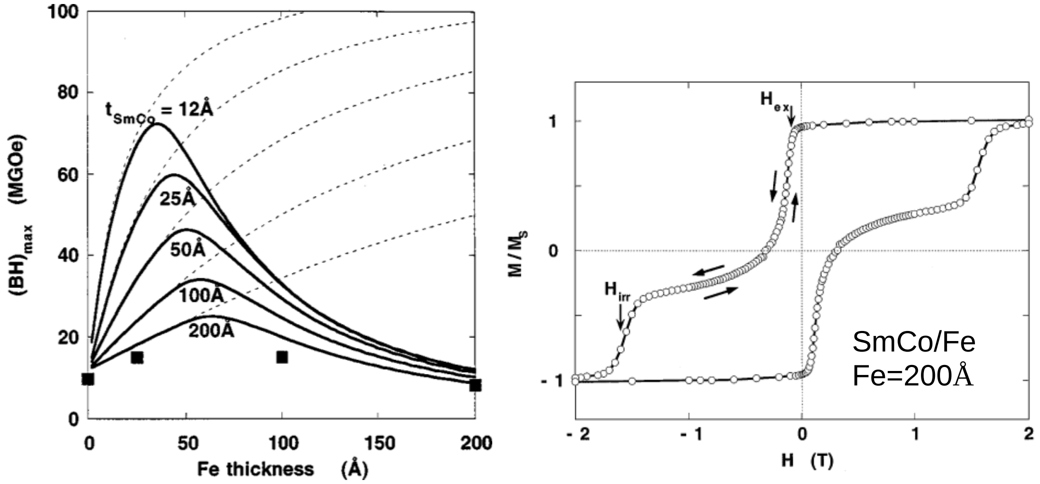

Figure 3.3. (Left) The $(BH)_{max}$ values as a function of Fe thickness in SmCo/Fe bilayers. Till a proper Fe thickness, $(BH)_{max}$ increased about five times by the ferromagnetic exchange coupling at the interface. (Right) Measured *M-H* loop in SmCo/Fe (200 Å) bilayer. The two-step demagnetizing behavior is shown in thicker Fe sample [3].

The referred papers on exchange spring magnet, which have been discussed up to now, have used the ferromagnetic exchange coupling at the interface of hard and soft magnetic layers. However, in 2000 Groot et al. published a paper showing antiferromagnetically exchange-coupled multilayer system [2]. Here, they used crystalline $DyFe_2/YFe_2$ ferrimagnet multilayers in which the dominant magnetic moment of each layer is different. In $DyFe_2$, Dy moments are dominant, and in YFe_2, Fe moments are dominant.

In Fig. 3.4, the antiferromagnetic exchange coupling behavior and the corresponding magnetic configurations are schematically represented in this crystalline $DyFe_2/YFe_2$ structure. First of all, inside the ferrimagnetic $DyFe_2$ layer, there is antiferromagnetic exchange coupling between Dy and Fe moments. Besides that, there is also ferromagnetic exchange coupling between Fe-Fe moments at the interface between $DyFe_2$ and YFe_2 layers. After all, the overall coupling between $DyFe_2$ and YFe_2 seems to be antiferromagnetic. At the large negative magnetic field, the edge part of the YFe_2 layer is pinned to the positive direction due to the Fe-Fe ferromagnetic exchange interaction at the interface. The middle part of YFe_2 moments, however, will follow the direction of the external magnetic field (see Fig. 3.4(a)). At the remanent state or small positive field, Dy moments in $DyFe_2$ are still pointing the negative direction due to its strong crystalline anisotropy, but Fe moments in YFe_2 are pointing the positive direction because of the interface Fe-Fe ferromagnetic coupling (see Fig. 3.4(b)). As a result, the two-step demagnetization and negative coercivity are obtained as shown in the right panel of Fig. 3.4. To sum up, all the competing energy terms in this structure are E_{ex} (Antiferromagnetic between Dy and Fe moments), E_{ex} (Ferromagnetic at the interface), E_{Zeeman}, and E_{aniso}.

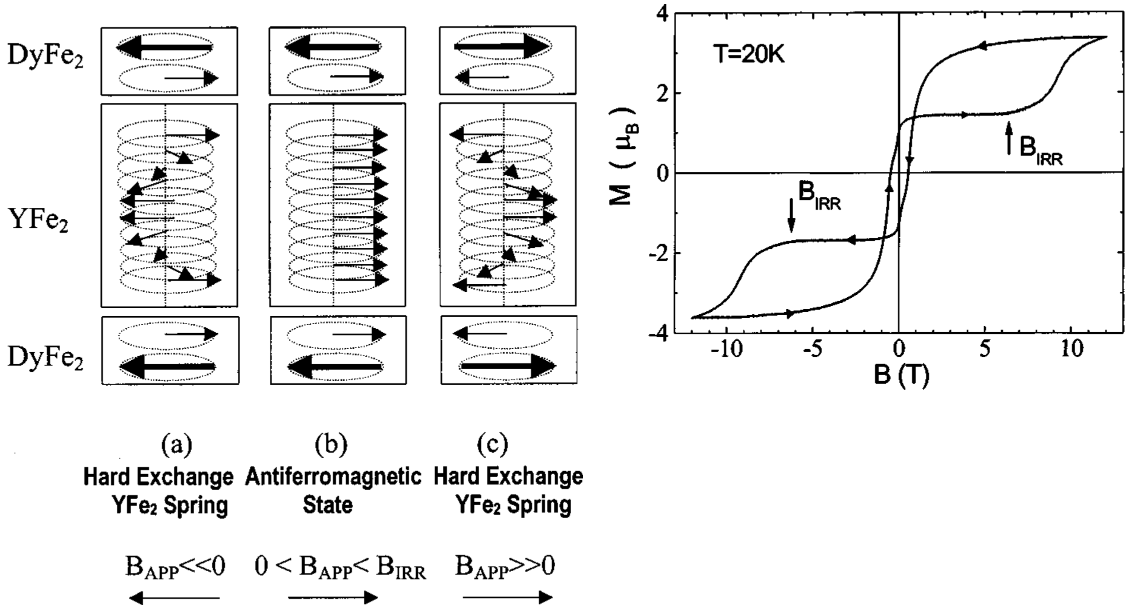

Figure 3.4. (Left) Schematic explanation of the antiferromagnetically exchange coupled spring magnet behavior. Dy magnetic moments in $DyFe_2$ are strongly pinned due to their crystalline anisotropy, but Fe moments in YFe_2 are gradually bent from the Fe-Fe ferromagnetic interaction direction to the external magnetic field direction. (Right) *M-H* behavior measured in the antiferromagnetically exchange coupled crystalline $DyFe_2/YFe_2$. A two-step demagnetization and negative coercivity behaviors appeared [2].

The same group who published the previous paper also investigated the temperature dependence of exchange spring magnet behavior in the same structure of crystalline $DyFe_2/YFe_2$ multilayer [6]. In this result, as the temperature increases, the H_C of a hard magnetic component as well as the M_S decreased as indicated in Fig. 3.5. The decreased M_S is attributed to the lowered Curie temperature of $DyFe_2$, and the decreased H_C (and weakened two-step demagnetization) can be analyzed as the decreased crystalline anisotropy energy of $DyFe_2$ layer. In this work, I will only focus on room temperature operations, but even at the room temperature, I will be able to manipulate this anisotropy energy by using strain, not by temperature.

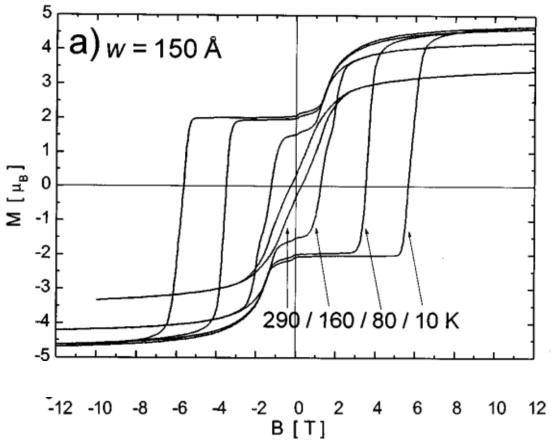

Figure 3.5. The *M-H* loops in various temperature from 10 K to 290 K. The temperature dependence of antiferromagnetically coupled exchange spring magnet behavior can be obtained [6].

Then, in 2004 Dumesnil and Mangin firstly used XMCD (X-ray magnetic circular dichroism) analysis technique to confirm the exchange spring magnet mechanism. In 2005, they published a paper using the XMCD analysis technique to firmly understand the mechanism of antiferromagnetically coupled exchange spring magnet with the crystalline $DyFe_2$/YFe_2 multilayers [7]. With this technique, each atomic magnetic moment component can be separately detected as shown in Fig. 3.6 (b, d). Based on this XMCD data, the micromagnetic configurations are depicted as arrows in Fig. 3.6 (a, c). As we can recognize in this figure, the switching behaviors at 100 K and 200 K are different. At 200 K, Dy moments in $DyFe_2$ switched earlier than the remanent state. This opposite switching behavior is attributed to the decreased hardness of $DyFe_2$. This overall magnetization behavior is corresponding to the individual XMCD component change.

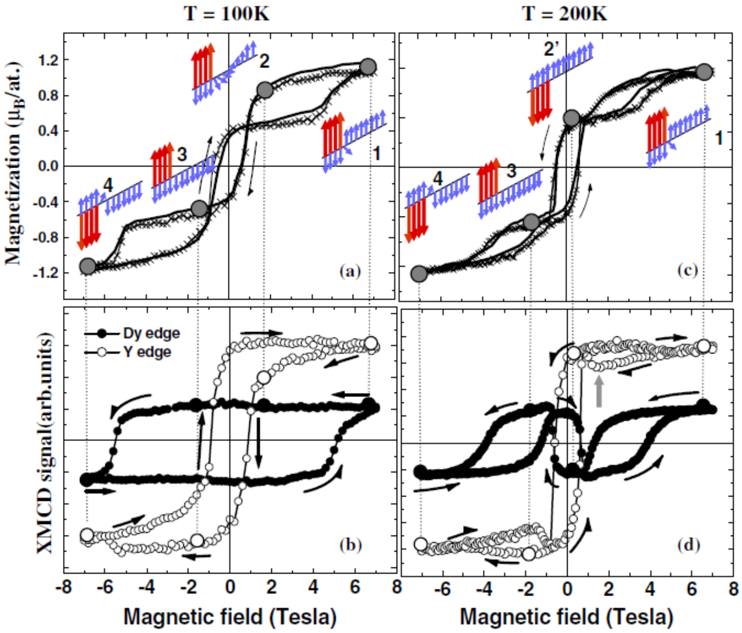

Figure 3.6. Measurements performed in 100 and at 200 K for the superlattice [$DyFe_2$(5 nm)/YFe_2(20 nm)]$_{13}$. Top curves (a, c) are macroscopic magnetization measurements. Bottom loops (b, d) are XMCD results measured at the Dy and Y edges. Long arrows correspond to Dy moments, short ones to Fe moments [7].

3.1.2 Amorphous Ferrimagnetic Alloys

The exchange spring magnets containing negatively coupled soft and hard magnetic phases have been extensively studied due to their abnormal magnetic behavior and high potential in spintronic applications. The Most ESM systems, however, have major shortcomings such as an immovable magnetic response, low-temperature operation, and high coercivity. The ESM properties are modified by changing the layer's thickness ratio or selecting a material with a different magneto-crystalline anisotropy. This selection produces ESM materials whose magnetic response is fixed and cannot be modified once fabricated.

Therefore, new ESM studies focusing on controlling in-situ magnetic properties are needed. For this, magnetoelastic ferrimagnetic alloys in an amorphous phase are studied in this work. In general, amorphous rare earth-transition metal (R-T) ferrimagnetic alloys have much lower coercive fields than their crystalline counterparts. And, their magnetic properties sensitively vary depending on temperature and relative composition. First, the meaning and common properties of ferrimagnetic materials are stated, and the sensitive dependences of amorphous ferrimagnetic materials on the temperature and composition are followed by.

A ferrimagnetic material is defined as one in which the magnetic dipole of the atoms on different sublattices are opposed as in antiferromagnetism, but in ferrimagnetic materials, opposing moments are unequal and a spontaneous net magnetization remains. Figure 3.7 shows the schematic diagram of the atomic dipole configuration for a ferrimagnetic material. The magnetic dipole moments in a ferrimagnetic material are divided into sublattices and are classified as a subset of antiferromagnetic materials. Each sublattice can be treated as ferromagnetic material and the difference between the magnetic dipole moments for the sublattices results in the net magnetization for the ferrimagnetic materials. This happens when the sublattices consist of different materials or ions [8].

Ferrimagnetic materials are like ferromagnets in that they hold a spontaneous magnetization below the Curie temperature and show no magnetic order above this temperature. However, there is sometimes a temperature, below the Curie temperature, at which the two sublattices have equal moments, resulting in a net magnetic moment zero; this is called the magnetization compensation point. This compensation point is observed easily in garnets and rare earth-transition metal (R-T) alloys. Furthermore, ferrimagnets may also exhibit an angular momentum compensation point at which the angular momentum of the magnetic sublattices is compensated. This compensation point is a decisive point for achieving high-speed magnetization reversal in magnetic memory devices. Below the magnetization compensation point, ferrimagnetic material is magnetic. At the compensation point, the magnetic components cancel each other and the total magnetic moment is zero [8].

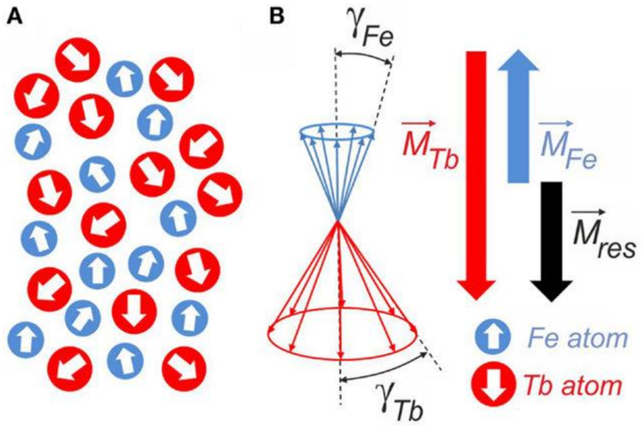

Figure 3.7. (a) Magnetic moment distribution in an amorphous ferrimagnetic Tb-Fe material with two preferred antiparallelly oriented magnetic sublattices. (b) Averaged distribution of the magnetic moments [9].

The sensitive composition and temperature dependences of the magnetic properties in amorphous R-T ferrimagnetic alloys are well researched by Hensen et al. in 1989 [10]. The room-temperature composition dependence of M_S is shown in the left panel of Fig. 3.8 for some amorphous ferrimagnetic R-Fe and R-Co alloys prepared by evaporation. The temperature dependence of M_S at several compositions of $Tb_{1-x}Fe_x$ is shown in the right panel of Fig. 3.8 [10,11]. For small x range, complete saturation cannot be reached because extremely rare earth-dominant alloys require so high magnetic field to saturate, but the available applied field was limited to 1.6 × 10^6 A/m. For the intermediate x range, there are parabolic-shape curves with relatively low M_S values, which means that they are still rare earth-dominant, but there is a combinational effect with transition metal moments having high M_S. Then, all the alloys have a certain composition at which M_S becomes zero between x=0.7~0.8, which indicates the compensation composition, x_{comp}. Beyond this composition, MS values abruptly increase due to the high-M_S transition metal-dominant configuration.

The temperature dependence, shown in the right panel of Fig. 3.8, also shows a similar tendency as composition dependence having a certain compensation point. The compensation appears in different temperatures depending on the relative composition even in the same material, TbFe. The magnetic compensation for composition and temperature are defined by

$$M_R(x_{comp}, T_{comp}) - M_T(x_{comp}, T_{comp}) = 0$$

, where x_{comp} and T_{comp} are the compensation composition and the compensation temperature, respectively. For amorphous $Gd_{1-x}Fe_x$, T_{comp}= 295 K was found when x = 0.745 [10]. The room temperature x_{comp} values for most alloys prepared under the same conditions appear in range 0.7 < x_{comp} < 0.8 as shown in Fig. 3.8 except for Er-T alloys.

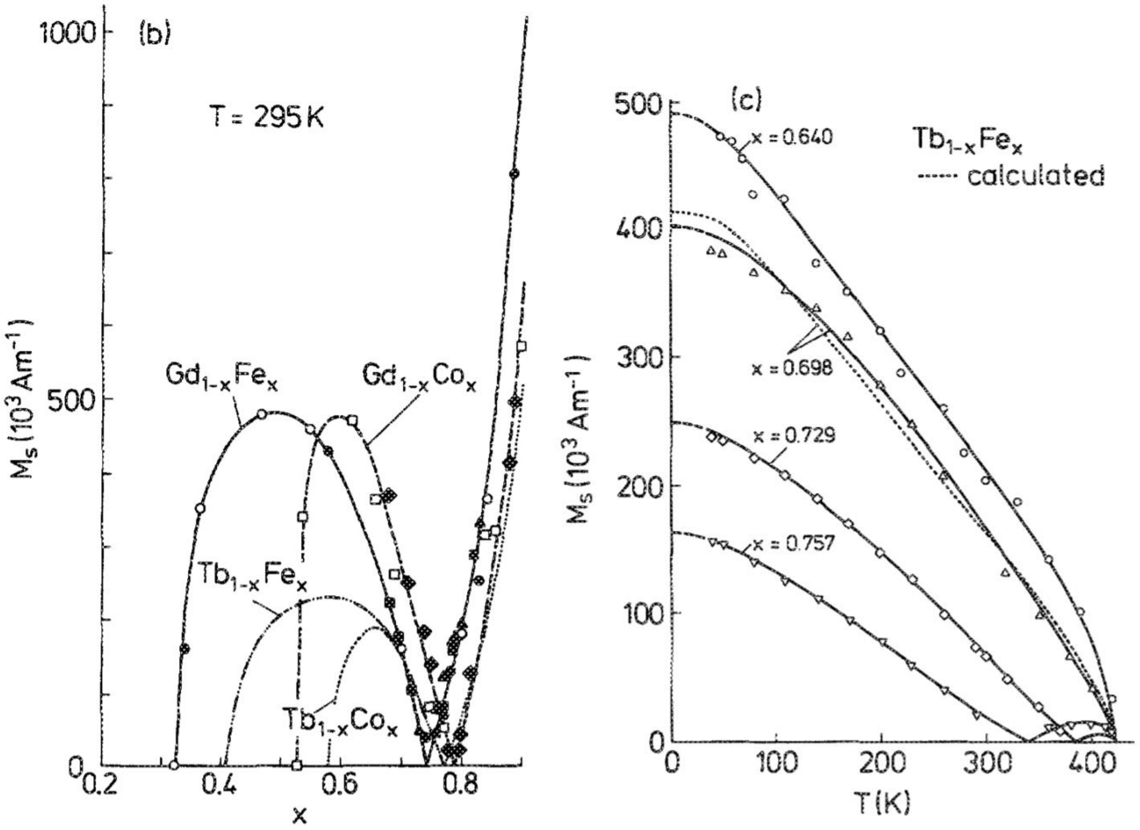

Figure 3.8. Compositional variation of the room-temperature saturation magnetization for amorphous $R_{1-x}T_x$ films prepared by evaporation [10,11].

The variation of T_{comp} with composition is presented in Fig. 3.9 for some binary and ternary amorphous alloys [10]. The plots yield a T_{comp} shift of 40 K/at.% for Tb-T alloys and 100 K/at.% for Gd-Fe alloys which demonstrates the high sensitivity of T_{comp} on composition. The compositional variation of T_{comp} for Dy- and Ho-based alloys shows smaller shifts of the order of 20 K/at.% [11]. Therefore, any changes on the R or T moment and the exchange interaction by small additions of nonmagnetic atoms, the presence of impurities, oxidation effects, thermal treatments or structural changes lead to drastic variations in T_{comp}.

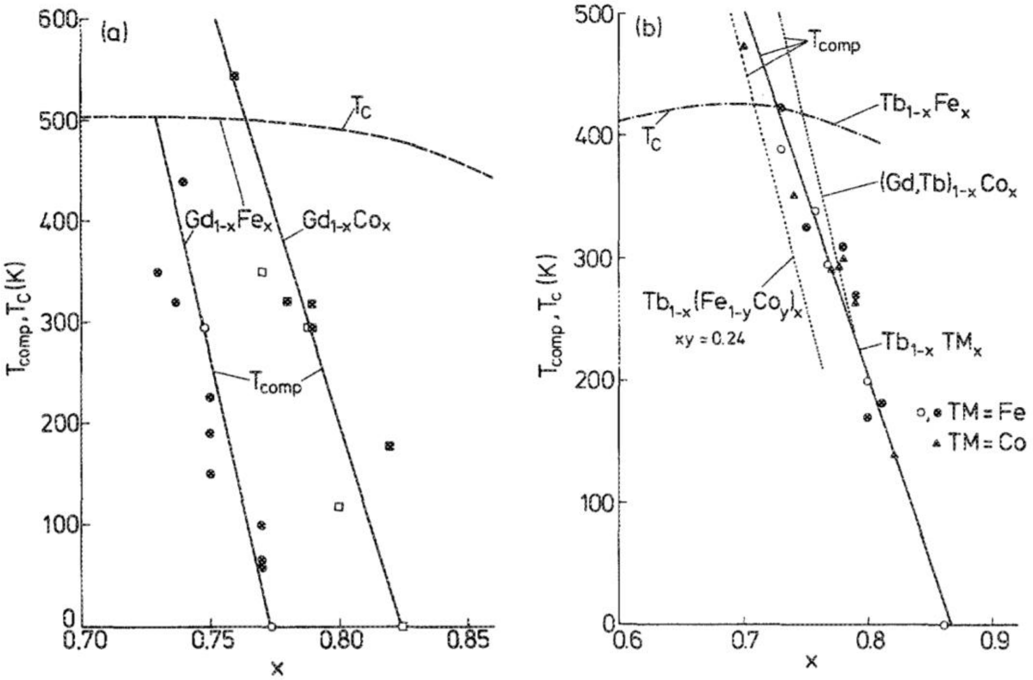

Figure 3.9. Compositional variation of the compensation temperature for amorphous $R_{1-x}T_x$ alloys prepared by evaporation [10].

Several studies have evaluated TbFe(Co) thin films and bulk TbFe material properties near the compensation composition. These studies show the magnetostriction coefficients (λ_s), as well as the saturation magnetization, are strongly dependent on the composition [9,10,12,13]. The saturation magnetization of amorphous Tb_xFe_{1-x} thin-film samples is plotted as a function of composition in Fig. 3.10. We can see that at 28 %Tb, the magnetization goes to zero. It is known that the saturation magnetization of R-T alloys is determined by a strong R-T exchange interaction which gives rise to an antiparallel coupling of the R and T spins [12,14]. Figure 3.10 confirms this and indicates that the composition of 28 %Tb is a compensation composition of the material.

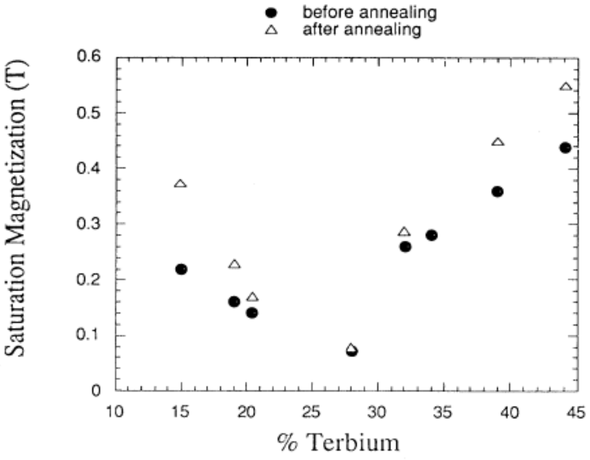

Figure 3.10. Tb composition dependence of saturation magnetization of amorphous TbFe alloys. The magnetization vanishes at ~28 Tb at%, which represents compensation composition of amorphous TbFe alloy [12].

Figure 3.11 shows the magnetostriction values as a function of Tb composition before and after annealing. The magnetostriction coefficients (λ_S) after annealing present a similar behavior with the saturation magnetization. At the compensation composition, 28 %Tb, λ_S becomes minimum. Based on the compensation, there seems clear asymmetry on the λ_S values. In the Tb-dominant range, λ_S significantly increases while in Fe-dominant range, it moderately increases. Note that the y-axis of the plot is in a log scale. As a result, Tb-dominant range produces much higher λ_s than Fe-dominant compositions by a few atomic % difference [12]. This λ_s difference provides an opportunity to control an ESM material using the induced magnetoelastic anisotropy.

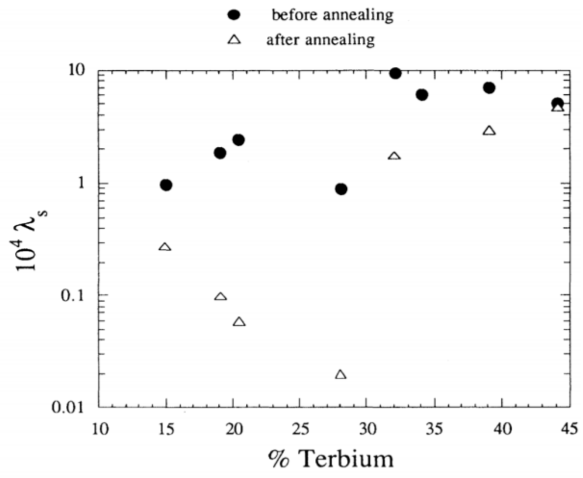

Figure 3.11. The magnetostriction of amorphous Tb_xFe_{1-x} (0.10 < x < 0.45) thin films as a function of Tb atomic composition [12].

In this chapter 3, a room temperature ESM behavior is demonstrated in a compositionally graded TbFe thin film near the compensation composition. The Tb-dominant and Fe-dominant phases, formed by the composition gradient in TbFe film, act as hard and soft magnetic layers in ESM structure. The *M-H* behavior of this ESM structure is explained using the major and minor spins present in the respective phases and their coupling states. When subjected to a mechanical load, the film′s separated switching steps and negative coercive behavior are modulated and eliminated due to the higher magnetostriction present in the Tb-dominant layer.

3.2 Thin Film TbFe

3.2.1 Fabrication of Amorphous TbFe Films

Amorphous TbFe films were deposited on 4-inch diameter Si(100) substrates using a dc sputtering technique. Figure 3.12 shows the outside (left) and inside (right) of the vacuum chamber of the Denton sputtering tool used for the deposition. This tool is installed inside of a class 1000 HEPA filtered cleanroom at UCLA. A 3-inch diameter $TbFe_2$ alloy target, manufactured by Princeton Scientific, is mounted at one of dc power gun of the sputtering system. As shown in Fig. 3.12, the dc power gun is facilitated having an angle with the substrate holder in order to allow a uniform deposition through the entire 8-inch diameter substrate holder. For the uniformity, the holder rotates during deposition with a constant speed that users set up in advance. The base pressure inside the chamber is maintained below 2×10^{-6} Torr.

Figure 3.12. Denton sputter deposition tool. (Left) Exterior of the tool installed in the class 1000 HEPA filtered cleanroom facility (Right) Inside of the vacuum chamber showing the angled sputtering guns and rotating substrate holder.

The sputtering power is controlled by the electric current values that users set up for the dc power depositions. Figure 3.13 shows the correlation between the controlling parameter, electric current, and the corresponding output sputtering power. A wide range of current parameters (0.25 ~ 0.75 A) are tested, and a completely linear relation is acquired between two parameters indicating that the power and sputtering process are done in a pure dc mode.

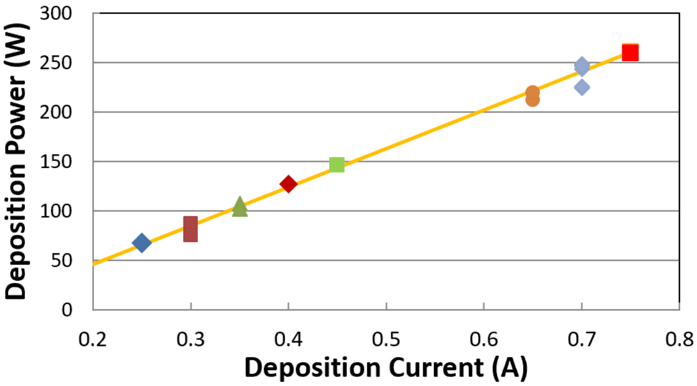

Figure 3.13. Linear dc power variation depending on the deposition current which is a controlling parameter in this sputtering system.

Keeping a sputtering power stable throughout a deposition is important to confirm the consistent film properties. For this, every deposition is begun after enough pre-sputtering, over 300 seconds, giving time to reach the targeted power. Especially, since the power of this sputtering tool is controlled by the current flow value, there is a risk for the power to fluctuate during the deposition. Hence, checking the sputtering power during the deposition in real time is required, and the records are plotted in Fig. 3.14. Note that all the plotted deposition time started after the pre-sputtering of over 300 seconds. Most of the deposition events kept a stable sputtering power through the deposition time, except for one sample. The red dotted lines will be explained later in chapter 3.3.

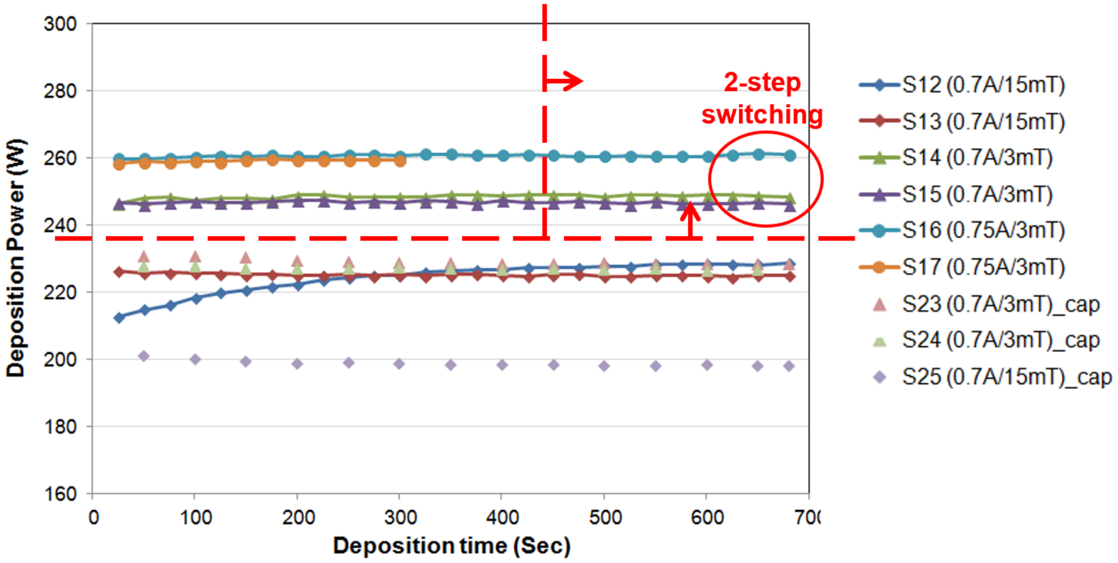

Figure 3.14. dc power variation during the deposition of the selected TbFe films. The red dashed lines and arrows represent the condition to show a two-step switching behavior. Certain degree of high power and long enough deposition time are required to show the two-step switching.

The Ar gas pressure and dc power are controlled to have TbFe alloy films with the targeted relative compositions. Note that the alloy films' composition can be tuned within a certain range even if the fixed-composition alloy targets are used [15]. This is because the required energy to kick off the atoms from the target is depending on the elemental species. To know the relative composition of TbFe films, energy dispersive X-ray spectroscopy (EDS) is used, and the representative result is shown in Fig. 3.15. The characteristic energy peaks depending on the elemental species in the film appeared in the plot. Unfortunately, the K-lines of Fe and L-lines of Tb are quite close resulting in incorrect absolute numbers for the composition. However, they are enough to know the relative change of the composition depending on the process parameters (i.e. sputtering power and Ar gas pressure). The exact compositional analysis is performed later on the selected films by using a wavelength dispersive X-ray spectroscopy (WDS), inductively coupled plasma mass spectrometry (ICP-MS), and EDS having a higher resolution.

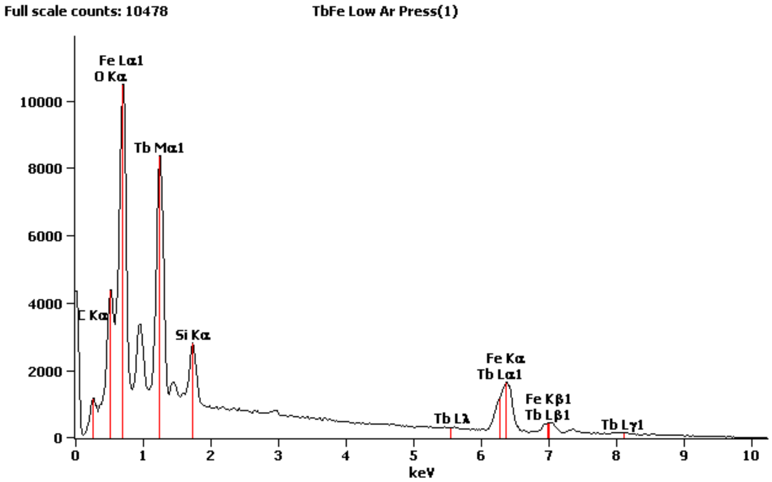

Figure 3.15. A representative compositional analysis result of TbFe film measured by energy dispersive X-ray spectroscopy (EDS)

Figure 3.16 presents the measured Fe composition (in at%) of TbFe films as a function of the sputtering power (in W) used in the deposition. It shows a clear trend that as power increases, the Fe composition also increases. The several points deviating the trendline indicate the films deposited at a very high Ar gas pressure (15 mTorr). Although the absolute Fe compositions can be shifted from the numbers in the y-axis, the sputtering power dependence and the controllable range of composition (~6 at%) are obtained from this set of measurements.

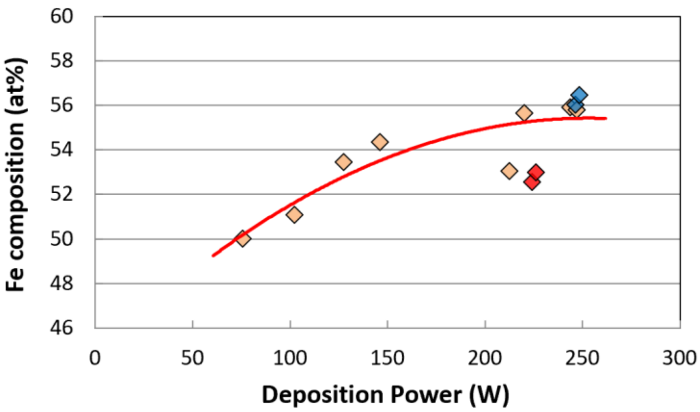

Figure 3.16. Correlation plot between relative Fe composition and the deposition power at 7 mTorr of Ar pressure (red symbols for 15 mTorr, blue symbols for 3 mTorr)

Figure 3.17 plots the Fe composition (in at%) as a function of the Ar gas pressure (in mTorr) during the depositions. This indicates that as Ar pressure increases, the Fe composition decreases. There is a rare deviation from the trendline in this correlation, and the controllable range of the Fe composition by the Ar pressure (~4 at%) is smaller than the sputtering power.

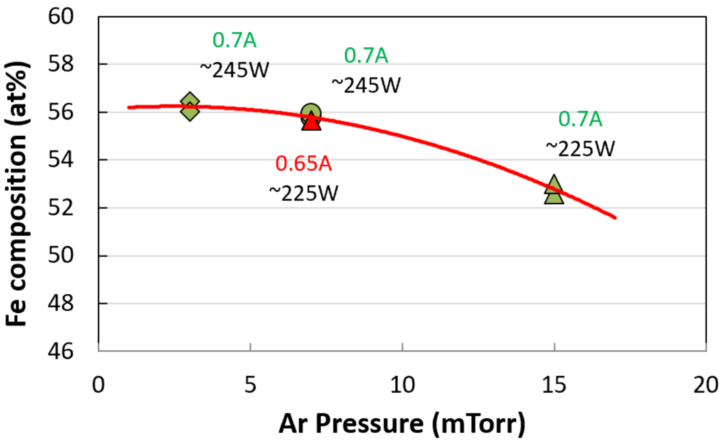

Figure 3.17. Correlation plot between Fe composition and the Ar pressure at 0.7 A, ~240 W (red symbol for 0.65 A).

3.2.2 Material Characterization

The amorphous TbFe film fabricated with 3 mTorr Ar gas pressure and 250 W sputtering power was selected, and the material properties were further characterized. Firstly, the film's amorphous state was confirmed with a Bruker D8 Discovery X-ray Diffractometer (XRD) showing the absence of any peaks in a range of 2-theta from 15° to 60° as shown in Fig. 3.18.

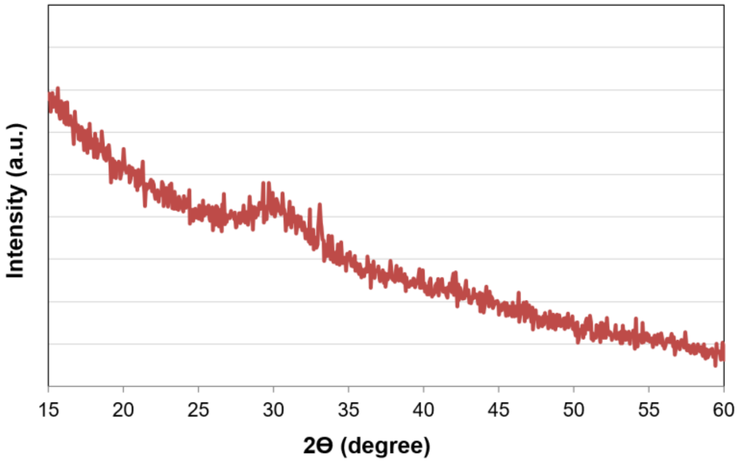

Figure 3.18. XRD measurement data from the TbFe film, which represents no prominent peak and amorphous phase of the film.

Cross-sectional transmission electron microscopy (TEM) samples were prepared by the *in-situ* lift-out method using an FEI Nova 600 Dual Beam microscope. Figure 3.19 shows SEM images taken during the TEM sample preparation. The left image shows that the vertical profile from Si substrate to Pt cap is revealed by a dual beam etching. The right image clearly indicates the three different layers for Si substrate, amorphous TbFe, and Pt cap, from bottom to top. So, the amorphous TbFe sample is ready to be analyzed for the vertical composition profile as well as the TEM images.

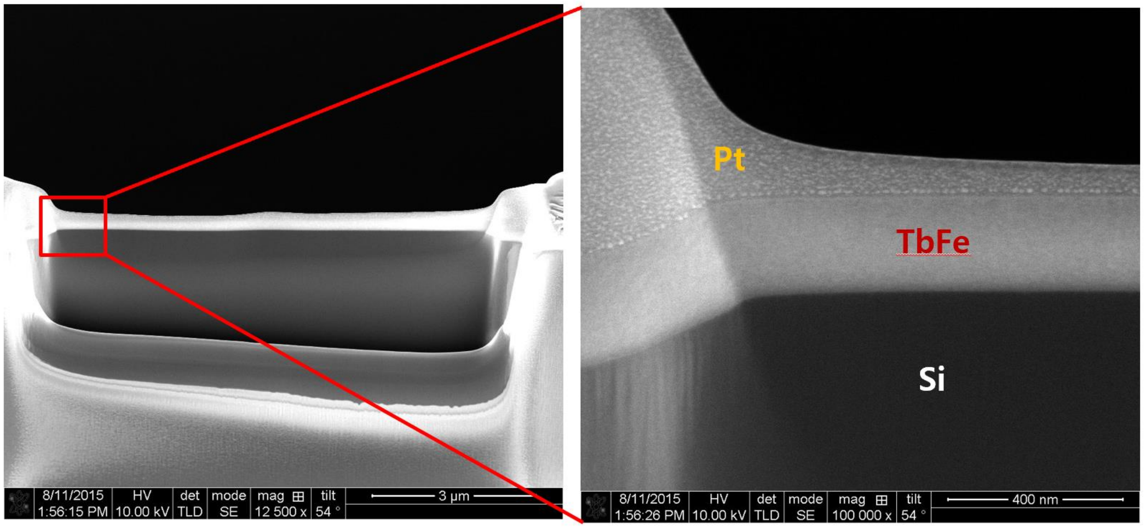

Figure 3.19. SEM images taken during TEM sample preparation by an FEI Nova 600 Dual Beam microscope.

Figure 3.20 shows representative TEM images taken on the cross-section of the TbFe film. The left image of Fig. 3.20 is the high-resolution TEM image, but any specific crystalline lattice structure cannot be seen in it. The right image is the diffraction pattern measured on the cross-section of the film and shows no crystalline pattern. Both images tell us that the deposited film is in an amorphous phase along with the XRD pattern in Fig. 3.18.

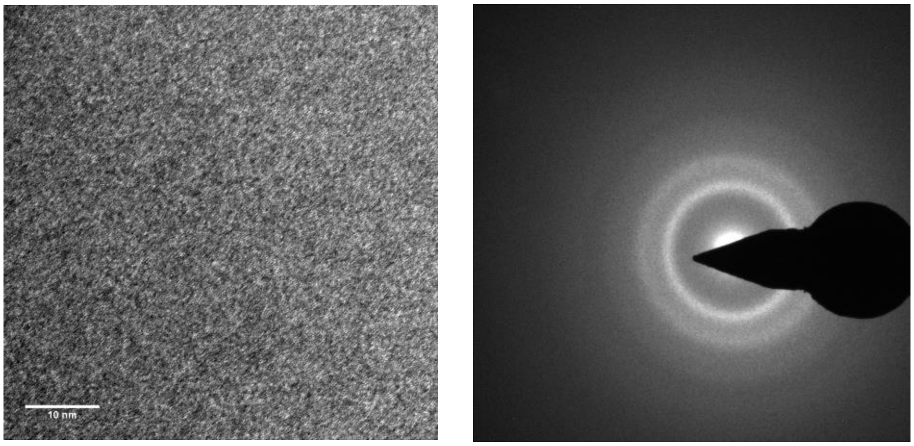

Figure 3.20. TEM images from the TbFe sample, which shows no crystalline lattice or regularity.

Compositional analysis on the cross section was conducted using an Oxford XMAX 80T EDS equipped within an FEI Titan 80-300 STEM. EDS line profiles were obtained with an annular-dark field (ADF)-STEM mode and the relative atomic composition profiles along the film thickness was determined by the Cliff-Lorimer method [16], which is implemented in Oxford Aztec software.

Figure 3.21 shows the variation of Tb and Fe atomic composition as a function of film thickness [17]. The 0.09 μm location represents the TbFe/Si substrate interface while the 0.38 μm represents Pt/TbFe interface. The spurious data at distances < 0.09 μm or > 0.38 μm are quantification errors due to the negligible Tb and Fe X-ray counts from the Si substrate or Pt capping. For the TbFe alloy film, the Tb atomic percent decreases from 29.1 at% (bottom) to 24.9 at% (top) while the Fe increases from 70.9 at% (bottom) to 75.1 at% (top) in a fairly linear fashion. The composition variation is caused by target heating during deposition producing different sputtering yields for each atomic component [18]. The dotted line and arrows will be used to explain the ESM behavior of the film in chapter 3.3.

In addition to the EDS composition analysis, ICP-MS is also used to verify the composition of TbFe films. The thinner samples fabricated with the same process parameters (3 mTorr, 250 W) are used for the composition analysis. The compositions of 29.1 ~ 29.7 Tb at% are measured in 20 ~ 40 nm-thick amorphous TbFe films, which is very close to the Tb composition of the bottom part (near Si substrate) of thick TbFe film shown in Fig. 3.21.

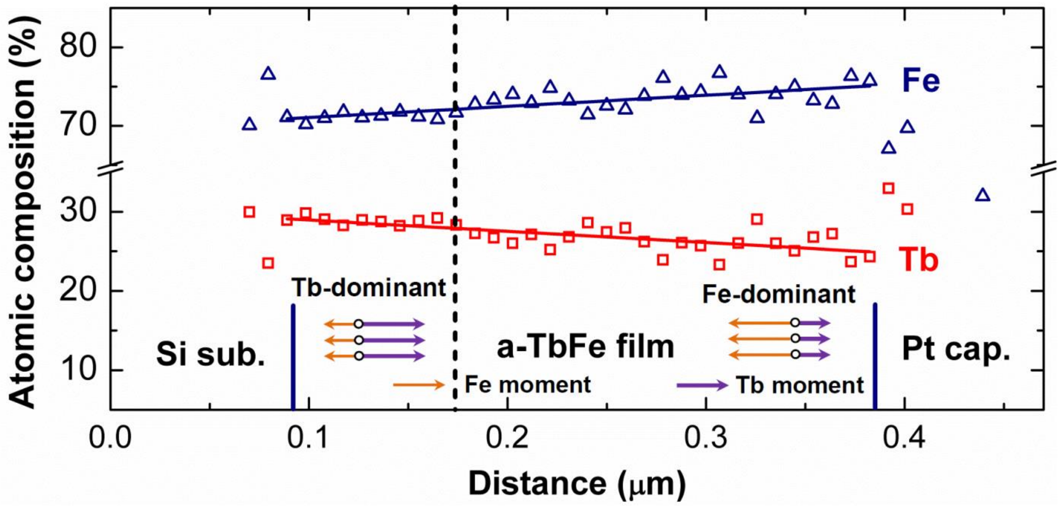

Figure 3.21. Atomic composition variation of Tb and Fe as a function of film thickness. Amorphous TbFe film ranges from 0.09 μm (bottom) to 0.38 μm (top). A dashed vertical line marks the compensation composition of TbFe film, and arrow schematics represent Tb and Fe-dominated regions based on the compensation composition [17].

3.3 Exchange Spring Magnetic Behavior

SQUID (superconducting quantum interference device) and MOKE (magneto-optic Kerr effect) systems were used to measure the in-plane magnetic hysteresis curves of the TbFe film. Room temperature SQUID measurements provided magnetization and coercive field values under 2 T fields. MOKE magnetic hysteresis loops in the longitudinal mode were measured in the presence of mechanical strain. For this test, a 2.5 cm × 0.5 cm sample was diced from the TbFe film on a 4 inch Si wafer and placed in a four-point bending jig capable of applying tensile or compressive strains depending upon the film orientation (see Fig. 3.25) [19]. Strain gauges attached to the backside of the sample measured the applied strain.

Figure 3.22 shows SQUID data for magnetization *M* versus magnetic field *H* measured along the in-plane direction of the film [17]. Figure 3.22 represents truncated hysteresis cycles (± 1200 Oe) for measurements between ± 2 T with arrows representing decreasing *H* values or the "sweep-down" curve. The magnetization at 2 T, while not shown, is 108 emu/cc. The smaller magnetization value 50 emu/cc at 1200 Oe is attributed to the relatively large high-field susceptibility of amorphous TbFe [20]. Figure 3.22 clearly shows two-step switching for decreasing *H* values (sweep-down) as well as increasing values (sweep-up). During sweep down, the first switching (marked as S1) occurs at +90 Oe producing a negative coercivity of -80 Oe and negative remanence of -9 emu/cc. The second switching (marked as S2) occurs at -750 Oe. When the sweeping direction is reversed from negative saturation (i.e. -2 T), similar two steps are observed including negative coercive field and negative remanence values.

The physics producing the two-step switching and negative coercive/remanence behavior are discussed with the use of Fig. 3.21. TbFe is a rare earth (RE)-transition metal (TM) ferrimagnetic material with two antiparallelly aligned Tb and Fe spins. The alloy's composition, as well as the operating temperature, dictates the effective magnetic moment. The compensation composition, represented by the alloy's net magnetic moment vanishing, is depicted by a dashed vertical line (28 Tb at%) in Fig. 3.21 [12]. The corresponding magnetic property variation across this vertical line is relatively sharp creating two separate regions with either Tb-dominant or Fe-dominant magnetic moments. This is contrasted with conventional systems where the magnetic properties change across an atomically sharp interface [6,7,21]. The illustrations in Fig. 3.21 show two regions magnetically dominated by either the Tb or Fe spins. The Tb atomic magnetic moment is represented with a darker arrow compared to the Fe moment and the arrow's length identifies the Fe-dominated region (adjacent to Pt) or the Tb-dominated region (adjacent to Si). These two regions produce the magnetic response observed in Fig. 3.22.

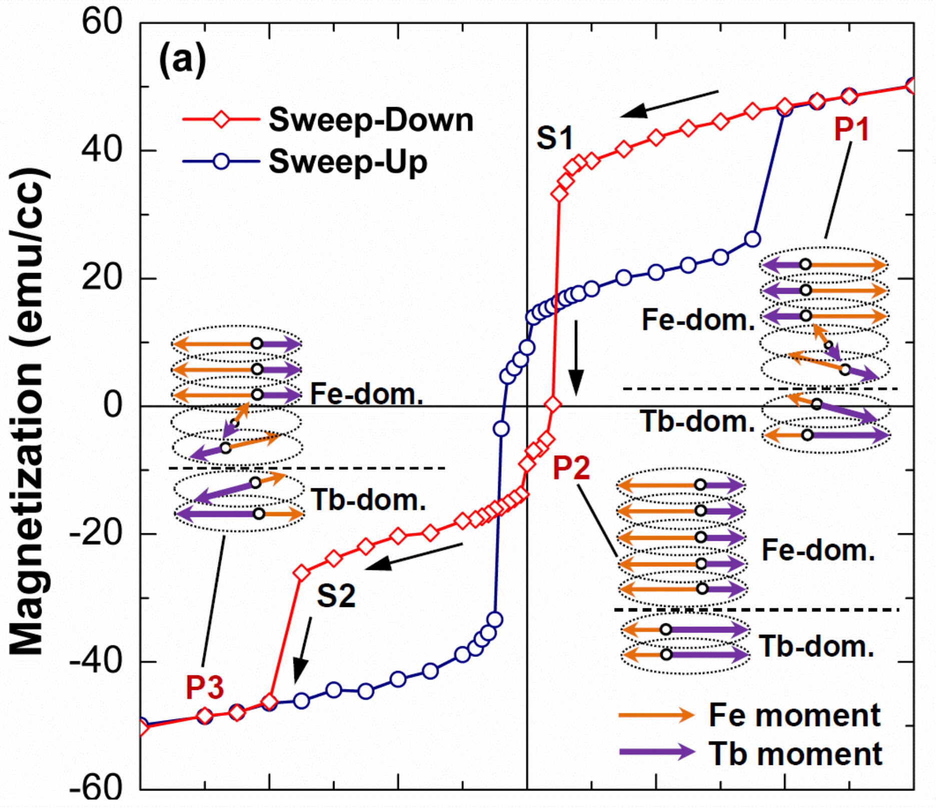

Figure 3.22. M-H curves for TbFe film. H field is swept between ±2 T, but truncated to show ±1200 Oe. Two switching steps (S1 and S2) are marked on a sweep-down curve. Arrow schematics show the Tb and Fe spin configuration at the corresponding points (P1-P3) in a sweep-down curve [17].

The two-step switching and negative coercive field, shown in Fig. 3.22, is caused by the presence of both Fe and Tb-dominated regions as well as the exchange coupling between them. The interface exchange coupling for three points (P1-P3) along the sweep-down portion of the *M-H* curve is illustrated with arrows in the schematics of Fig. 3.22. The exchange coupling at the interface derives from ferromagnetic Fe-Fe spin interaction between the Fe and Tb-dominant regions [22]. When a magnetic field is applied to the material, the exchange coupling between the Tb-dominant region and the Fe-dominant region has competition with the applied magnetic field energy. Specifically, The Tb spin in the Tb-dominant region, as well as the Fe in the Fe-dominant region, tends to align with the magnetic field which is in direct competition with the Fe-Fe spin interaction between the two regions. All the schematic spin arrows (Fig. 3.22) represent in-plane orientations with any deviations from the horizontal, signifying in-plane canting angles of interface spins.

At P1 in Fig. 3.22, the spins furthest from the interface (i.e. either Tb or Fe-dominant) wind to align towards the magnetic field direction. However, the interface spins in the Tb and Fe dominant layers cant (i.e. in-plane of the film) to accommodate the competition between the magnetic field aligning the net magnetic moment and the ferromagnetic Fe-Fe spin interaction. This competition creates a transition region between the canted spins and wound spins. The transition region thickness in the Fe-dominant region is larger than the Tb-dominant one due to the magnetically softer Fe-dominant region properties as compared to Tb-dominant.

As the magnetic field is decreased from P1 toward P2, the Fe-dominant transition region grows and at ~90 Oe (S1) all the Fe spins (see P2 illustration) in the Fe-dominated region flip. This point represents where the exchange coupling energy dominates the applied *H*-field energy resulting in a complete reversal of the Fe spins in the Fe dominated region. At $H = 0$, the flipped Fe spins produce a negative remanence value. As the field approaches P3, the Tb-dominant region flip in the presence of a sufficiently large negative field which overcomes the intrinsic magnetic anisotropy of the Tb-dominated region. At P3 the magnetic moments are 180 degrees out of phase with spin orientations illustrated by P1. This process represents an ESM with antiferromagnetic exchange coupling as described in previous ferrimagnetic multilayers [6,7,21].

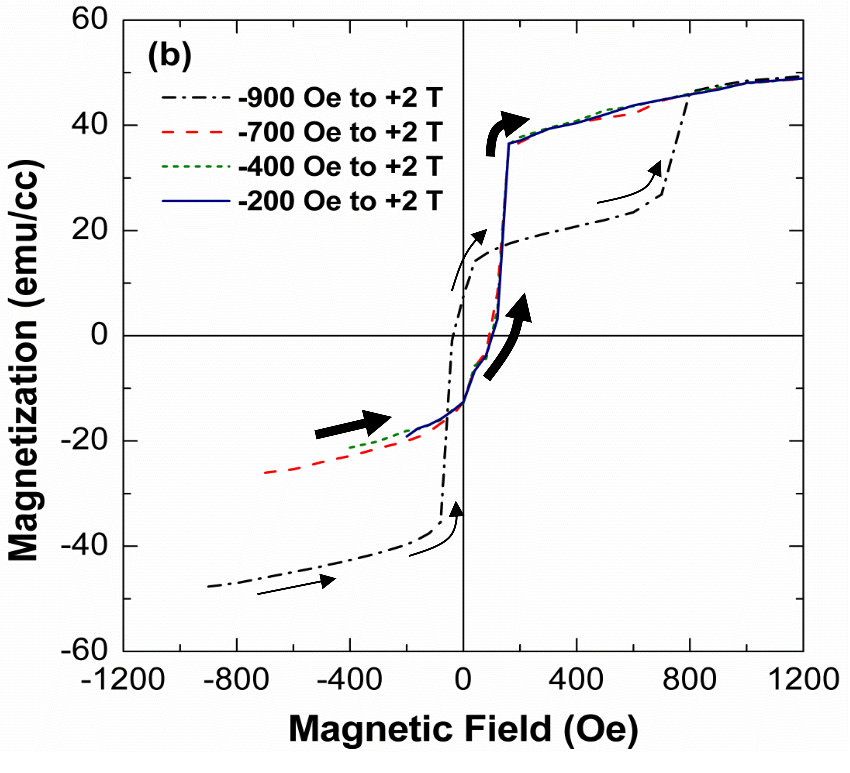

Figure 3.23. Sweep-up curves from 4 different H fields (i.e. -200, -400, -700, and -900 Oe) of minor loops. Sweep-down curves, which are identical to the one in Fig. 3.15, are not shown. Thicker and thinner arrows are marked to show different trajectories [17].

Generally, there are other mechanisms that could produce a negative coercive field such as an exchange bias and/or dual magnetic anisotropy. However, these possibilities are ruled out with experimental tests conducted on the sample. Firstly, in some cases, high magnetic fields can cause the exchange-bias field to change directions [23]. This directional change may result in an apparent negative coercive field in a symmetric manner. Fig. 3.23 shows minor sweep-up *M-H* curves for the same film presented in Fig. 3.22 [17]. The minor curves are measured by first saturating the film to +2 T and then reducing the field (i.e. sweep-down) to one of four values (i.e. -200, -400, -700, and -900 Oe), while not shown in the figure. The *M-H* curves in Fig. 3.23 show data for increasing *H* field from one of these four values, i.e. sweep-up curves.

As can be seen, three of these minor loops (i.e. -200, -400, and -700 Oe thicker arrows) overlap and follow the path of the sweep-down curve presented in Fig. 3.22. These overlaps arise due to the reversible rotation of Fe moments in the Fe-dominant region after passing through S1. On the other hand, Fig. 3.23 sweep-up curve from -900 Oe shows an entirely different trajectory (marked with thinner arrows) from the other curves. This difference is produced by the irreversible flip of the hard magnetic Tb-dominant region at S2. The reversible minor loop behavior for -200, -400, and -700 Oe while absent for -900 Oe (i.e. before reaching a hard magnetic phase switching) ensures that the first switching reflects the unwinding of the spins in the Fe-dominant region by exchange coupling [1]. This reversible behavior at relatively small applied magnetic fields rules out the possibility that this is an exchange bias mechanism and thus this is excluded as an explanation for the observed response.

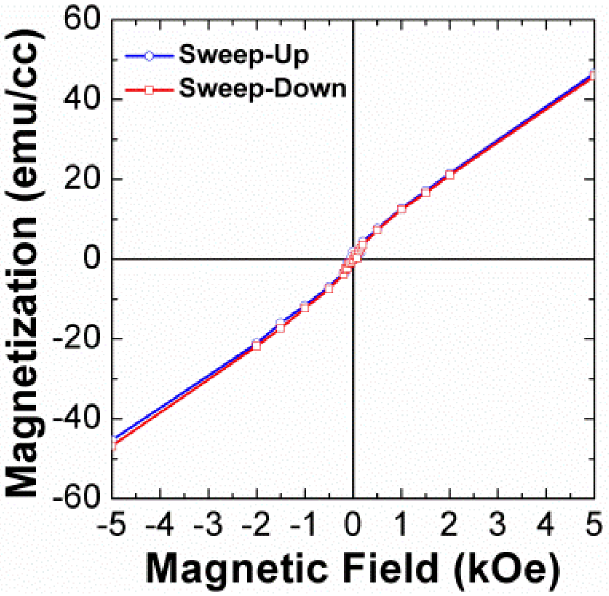

Figure 3.24. M-H loop of the TbFe thin film with a magnetic field applied normal to the film plane [17].

One must also consider the possibility that two different anisotropies may be present to produce an apparent negative coercive field [24]. This is a concern because some studies report a perpendicular magnetic anisotropy in amorphous TbFe films which is attributed to deposition parameters [25,26]. To eliminate the dual magnetic anisotropy from consideration, we measured *M-H* loops in different in-plane directions as well as the out-of-plane direction. All in-plane *M-H* measurements show similar results presented in Fig. 3.22 revealing that the film is magnetically isotropic in-plane. The *M-H* loop measured out-of-plane, presented in Fig. 3.24, shows a linear hard axis curve without hysteresis clearly indicating the magnetic moments are all in-plane [17]. Therefore, this rules out the dual magnetic anisotropy explanation for the negative coercive field. This leads us to conclude with reasonable certainty that the origin of the negative coercive field is the exchange coupling between Fe and Tb-dominant regions which can be controlled with an applied mechanical strain.

3.4 Strain-Applied Switching

Figure 3.25 presents MOKE *M-H* loops (i.e. in-plane measurements) measured at three different mechanical strains, i.e. 0, -820, and +540 με [17]. Since the 290 nm-thick TbFe film is much thinner than ~500 μm Si substrate, the film's strain is essentially uniform through the thickness. All strain values are discussed in terms of the film's strain rather than the Si substrate's. Figure 3.25(a), measured at 0 με, resembles the SQUID results shown in Fig.3.22 including the two-step and negative coercive behavior. The small differences in switching field values are caused by the MOKE measurement's limited sampling area (1-2 mm spot size) as well as penetration depth. Figure 3.25(b) *M-H* loop, measured at -820 με (i.e. compressive strain), eliminates the two-step switching and the negative coercive field. Figure 3.25(c), measured at +540 με (i.e. tensile strain), slightly enhances the two-step switching with absolute magnitudes of switching fields increasing by 28% (for S1) and 3% (for S2) compared to Fig. 3.25(a).

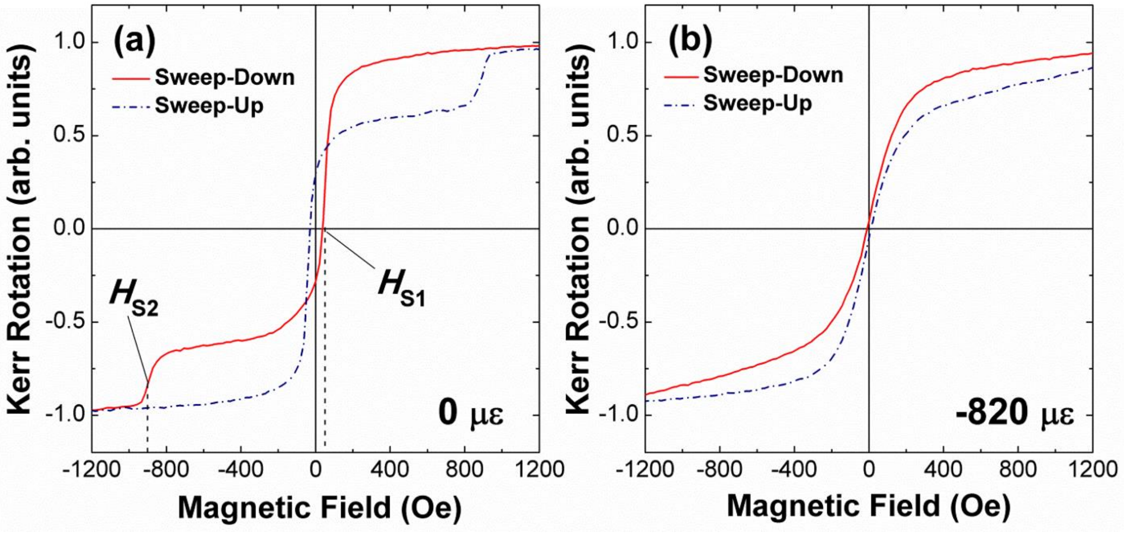

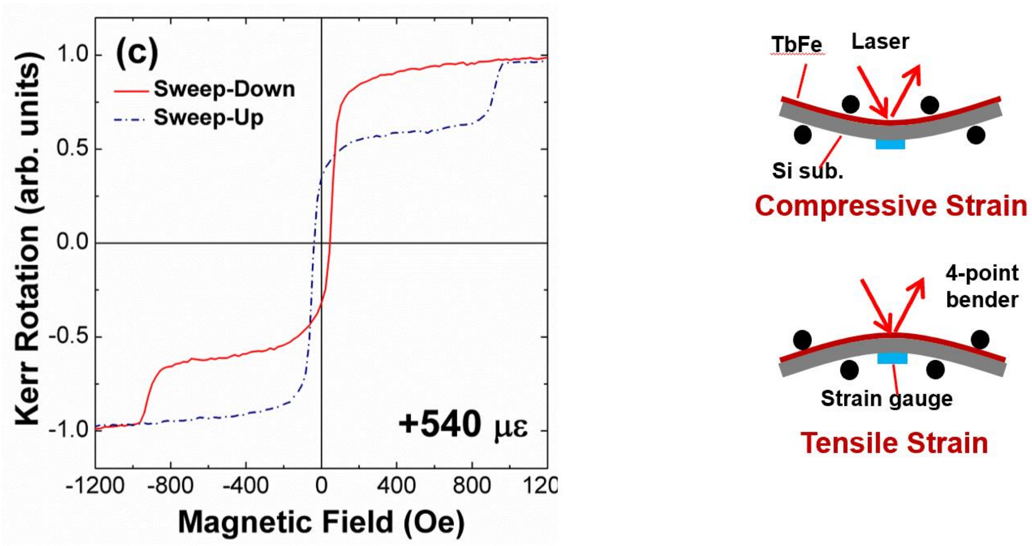

Figure 3.25. MOKE M-H curves measured at 3 different mechanical strains, i.e. 0, -820, and +540 με. The schematics in the right bottom indicate the four-point bending fixture used to apply mechanical strain [17].

Figure 3.26 plots the first and second switching fields (see H_{S1} and H_{S2} in Fig. 3.25(a)) as a function of mechanical strain [17]. As the applied compressive strain increases from zero, the H_{S1} value becomes less negative and switches to positive (-32 Oe to +10 Oe) values. On the other hand, H_{S2} becomes less positive, i.e. linearly decreasing from 913 Oe to 784 Oe. For increasing tensile strain values, H_{S1} becomes more negative (-32 Oe to -45 Oe) while H_{S2} becomes more positive (913 Oe to 941 Oe).

The functional dependence of H_{S1} and H_{S2} on strain is attributed to the induced magnetoelastic anisotropy. The strain-induced magnetic anisotropy is defined to be $K = \frac{3}{2}\lambda_S \cdot E \cdot \varepsilon$, where E is Young's modulus, λ_s is the magnetostriction coefficient, and ε is the strain applied. The λ_s values are a function of the relative Tb/Fe composition [12] with the Tb-dominant (Tb at% > 28, shown in Fig. 1) region two orders of magnitude larger than the Fe-dominant (Tb at% < 28) region. Therefore, the applied strains significantly change the magnetic anisotropy of the Tb-dominant region while the Fe-dominant region remains relatively unchanged. Thus, an applied strain increases (or decreases) H_{S2} under tensile (compressive) strain.

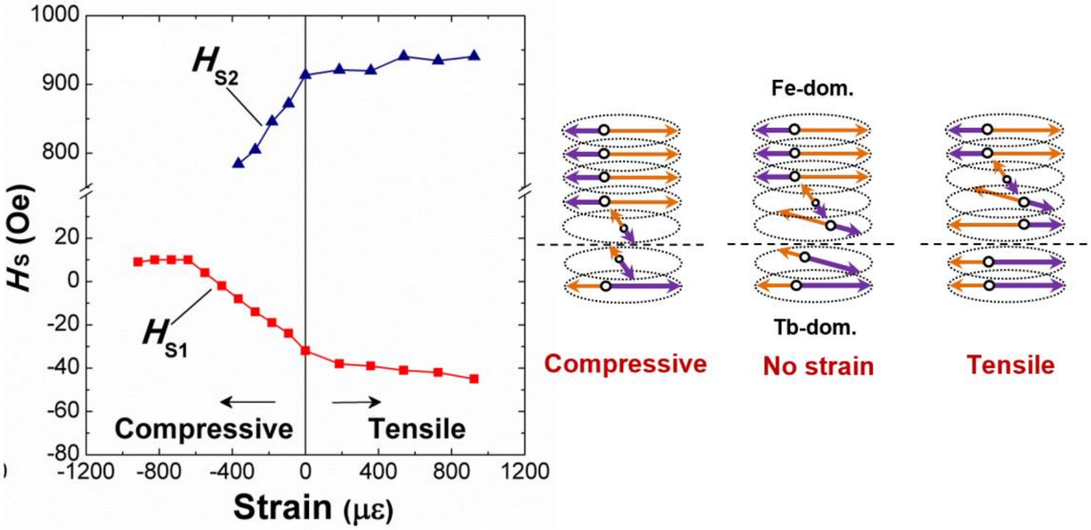

Figure 3.26. The first and second switching field (see H_{S1} and H_{S2} marked in Fig. 3.25(a)) variations as a function of mechanical strain. The arrow illustrations on the right show the change of exchange coupling state depending on mechanical strain [17].

The three schematics at the left, middle, and right side in Fig. 3.26 illustrate the magnetic spin states at P1 of Fig. 3.22 under applied compressive, zero, and tensile strains, respectively. All arrows in these drawings represent in-plane orientations with off-horizontal interface spin arrows representative of in-plane canting. As a tensile strain is applied to this system (schematic right), the Tb-dominant canting region is essentially eliminated while the Fe-dominant region size substantially increases compared to without a strain (schematic middle). This is caused by the large magnetostriction present in the Tb dominant region. In general, the smaller the canting angle of Tb dominant phase, the broader the transition region in the Fe-dominant region. For compressive strains, the canting angle in the Tb dominant region increases while the size of the transition in Fe dominant region decreases, i.e. exactly converse to an applied positive strain. These applied strains produce larger negative H_{S1} values under a tensile strain while smaller negative or even positive H_{S1} under a compressive strain.

Up to here, this chapter has focused on the ESM behavior (i.e. two-step switching, negative coercivity) shown in the one TbFe sample in order to make the explanation clearer. The ESM behavior has been measured in a number of TbFe films other than the one previously studied. Figure 3.27 shows the ESM features of another TbFe film. The top-left panel is the SQUID M-H loop without applied strain and shows the explicit two-step switching. The first switching happens before the magnetic field reaches zero, but the coercivity value is still positive since the Fe-dominant may be relatively thinner than the previous sample. Other panels in Fig. 3.27 present the MOKE M-H loops measured in the same sample with and without applying mechanical strain. The coercive field appears near 0 Oe, and as the tensile (compressive) strain increases, the coercivity moves negative (positive) values as the previous sample showed.

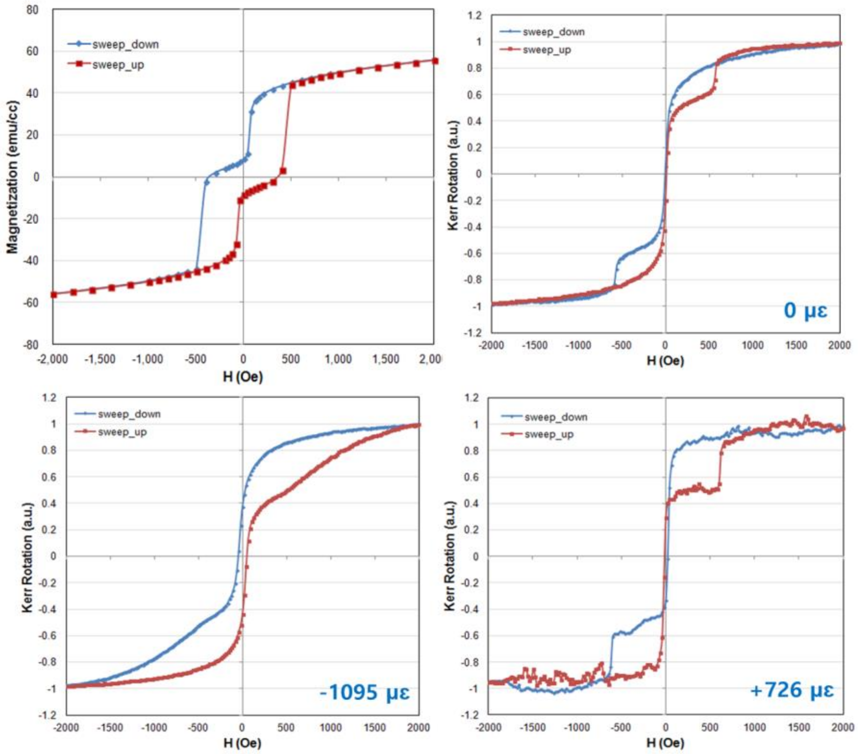

Figure 3.27. SQUID M-H loop without applied strain (Top, Left), MOKE M-H loop without applied strain (Top, Right), and strain-applied MOKE M-H loops (Bottom). Measured in another TbFe film showing a two-step switching and negative coercive field. Without strain, the coercive field is near 0 Oe, but as tensile (compressive) strain is applied, the coercivity moves negative (positive) values.

The coercive fields as well as the remanent magnetization from the strain-applied M-H loops of the sample in Fig. 3.27 are plotted as a function of applied strain in Fig. 3.28. Both of coercive field and remanent magnetization change their sign depending on the applied strain. Under tensile strains, both values change to a negative side indicating enhanced ESM behavior while under compressive strains, they change to a positive side representing disappeared two-step switching.

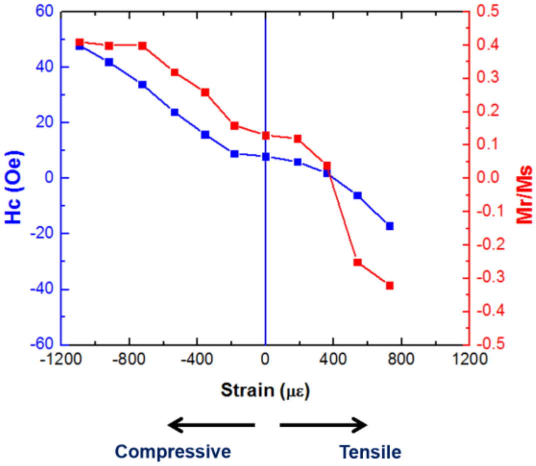

Figure 3.28. The coercive field and remanence magnetization variations as a function of applied strain.

The reproducibility of the TbFe films having ESM behavior is reviewed by using the sputtering power variation chart shown in Fig. 3.14 (see chapter 3.2.1). The hypothesis of the reason for the composition gradient through the film thickness is the alloy target heating during the deposition. If this is a right approach, there can be some correlation between the sputtering power and the presence of ESM behavior of the deposited films. The samples showing clear two-step switching are marked by a red circle in Fig. 3.14. Firstly, it is clear that the films fabricated in high sputtering power (> 240 W) is the required condition for the two-step switching. However, one sample with high power (260 W) and a shorter deposition time (300 sec) does not show any stepped switching behavior. It can be confirmed that both of high sputtering power and a long enough deposition time are required to show the two-step switching behavior. This fact strongly supports the hypothesis about a target heating during deposition because a higher power will definitely heat up the target more, and there should have enough deposition time (thickness) for the composition gradient to exceed the compensation composition of TbFe.

To sum up, exchange spring magnetic behavior has been experimentally observed in a compositionally graded amorphous TbFe thin film at room temperature. The gradient through the TbFe film thickness produces Tb and Fe-dominant regions, and their exchange coupling at the interface creates an ESM behavior. By applying a mechanical strain to the film, a two-step switching with the negative coercive field is both modulated and eliminated showing the promise of 180° switching. The modulation is caused by the relatively higher magnetostriction coefficient in the Tb-dominant region compared to the Fe-dominant producing larger changes in magnetic anisotropy as the strain is applied.

The sign change of coercive field and remanent magnetization measured in multiple TbFe samples represents a potential for the magnetic reversal up to 180° using the applied strain. This strain-applied ESM switching mechanism can be used in future memory devices if more studies are conducted to overcome some practical problems such as stability of a switched state. For these later devices, a voltage-induced strain would be implemented as suggested by other researchers.

3.5 Chapter References

1] E. F. Kneller, and R. Hawig, IEEE mag. **27** (1991) 3588

2] J-M. L. Beaujour, S. N. Gordeev, G. J. Bowden, P. A. J. de Groot, and B. D. Rainford, Appl. Phys. Lett. **78**, 964 (2001)

3] E. E. Fullerton, J. S. Jiang, M. Grimsditch, C. H. Sowers, and S. D. Bader, Phys. Rev. B, **58**, 12193 (1998)

4] E. Fullerton, J. S. Jiang, and S. D. Bader, J. Magn. Magn. Mater. **200**, 392 (1999)

5] H. Xi, J. Rantschler, S. Mao, M. T. Kief, and R. M. White, J. Phys. D: Appl. Phys. **36**, 1464 (2003)

6] M. Sawicki, G. J. Bowden, P. A. J. de Groot, B. D. Rainford, J.-M. L. Beaujour, R. C. C. Ward, and M. R. Wells, Phys. Rev. B, **62**, 5817 (2000)

7] K. Dumesnil, C. Dufour, Ph. Mangin, A. Rogalev, and F. Wilhelm, J. Phys.: Condens. Matter. **17**, L215 (2005)

8] R. K. Kotnala, and J. Shah, Handbook of Magnetic Materials, Elsevier (2015)

9] B. Hebler, A. Hassdenteufel, P. Reinhardt, H. Karl, and M. Albrecht, Front. Mater. **3**, 8 (2016)

10] P. Hansen, C. Clausen, G. Much, M. Rosenkranz, and K. Witter, J. Appl. Phys. **66**, 756 (1989)

11] P. Hansen, S. Klahn, C. Clausen, G. Much, and K. Witter, J. Appl. Phys. **69**, 3194 (1991)

12] J. Huang, C. Prados, J. E. Evetts, and A. Hernando, Phys. Rev. B, **51**, 297 (1995)

13] S. Mangin et al., Nat. Mater. **13**, 286 (2014)

14] I. A. Campbell, J. Phys. F: Met. Phys. **2**, L47 (1972)

15] W. X. Zhang, W. L. Zhang, L. W. Lin, B. Peng, H. C. Jiang, and S. Q. Yang, J. Magn. Magn. Mater. **280**, 143 (2004)

16] G. Cliff, and G. W. Lorimer, J. Microsc. **103**, 203 (1975)

17] T. Lee, M. K. Panduranga, C. W. Han, V. Ortalan, and G. P. Carman, Phys. Rev. Appl. **8**, 024024 (2017)

18] K. K. Ho, K. P. Mohanchandra, and G. P. Carman, Thin Solid Films, **413**, 1 (2002)

19] C. B. Hill, W. R. Hendren, R. M. Bowman, P. K. McGeehin, M. A. Gubbins, and V. A. Venugopal, Meas. Sci. Technol. **24**, 045601 (2013)

20] J. J. Rhyne, J. H. Schelleng, and N. C. Koon, Phys. Rev. B, **10**, 4672 (1974)

21] M. Sawicki, G. J. Bowden, P. A. J. de Groot, B. D. Rainford, R. C. C. Ward, and M. R. Wells, J. Appl. Phys. **87**, 6839 (2000)

22] R. Pellicelli, M. Solzi, C. Pernechele, and M. Ghidini, Phys. Rev. B, **83**, 054434 (2011)

23] S. Jain, D. Tripathy, and A. O. Adeyeye, J. Appl. Phys. **105**, 123916 (2009)

24] Y. J. Nam, and S. H. Lim, Appl. Phys. Lett. **99**, 092503 (2011)

25] C. Schubert, Chap. 2. Thin Amorphous Fe–Tb Alloy Films. In: Magnetic Order and Coupling Phenomena, Springer, Cham (2014)

26] S.-C. N. Cheng and M. H. Kryder, J. Appl. Phys. **69**, 7202 (1991)

4. TbFe Thin Films Having Perpendicular Magnetic Anisotropy (PMA)

4.1 Introduction

4.1.1 Usefulness of PMA

Magnetic thin films having perpendicular magnetic anisotropy (PMA) have been extensively researched for a recent decade to break the limitations of in-plane magnetic cells of STT-MRAM. As the magnetic cell dimensions are scaled down, magnetic tunnel junction (MTJ) with in-plane magnetic anisotropy suffers from its modest thermal stability, high power consumption, and manufactural challenges [1]. MTJs having PMA, on the other hand, have larger anisotropy energy compared to most of the in-plane anisotropy materials. In addition, for the patterned device, the magnetization of PMA materials is more uniform and does not suffer from thermal instability due to magnetization curling observed at the edge of the in-plane case. From the point of view of STT switching current, it is easier to reverse the magnetization of PMA free layer than the in-plane anisotropy one [2-5].

However, the current-based switching methods like STT are known to produce substantial ohmic heating losses resulting in energy inefficiencies. One of the promising alternatives is the strain-mediated multiferroics, which uses the voltage signal instead of the current flow. Even for the strain-mediated multiferroics, magnetoelastic PMA cells are preferred since 180° magnetization reversal is possible. A strain is basically a bi-directional input signal, and hence, previous strain-mediated multiferroic studies have demonstrated 90° in-plane magnetic switching both experimentally and theoretically. As an effort to overcome this limitation, the 180° in-plane switching using ESM with negative coercivity is performed and presented in Chapter 3. However, attention to in-plane magnetic memory elements has decreased because the element sizes needed for thermal stability are sufficiently large to cause multi-domain formation that leads to inefficient and complicated switching dynamics. This problem can be avoided by using nanopatterned memory elements that exhibit PMA, which has higher thermal stability at a comparably smaller size [6].

The left panel of Fig. 4.1 suggests the nanoscale magnetic structure for the strain-mediated 180° PMA switching [6]. The nano-patterned magnetoelastic element having PMA at the center can be switched by the voltage pulse applied on the patterned electrodes. The voltage pulse induces in-plane strain to the magnetic element, and the magnetization switches 180° by controlling the voltage pulse width. The right panel of Fig. 4.1 shows magnetization versus time for a single CoFeB element subjected to the voltage pulses. The pulse durations required for the three flips are 0.65 ns, 0.2 ns, and 0.26 ns, which are much longer than the relaxation time of PZT substrate.

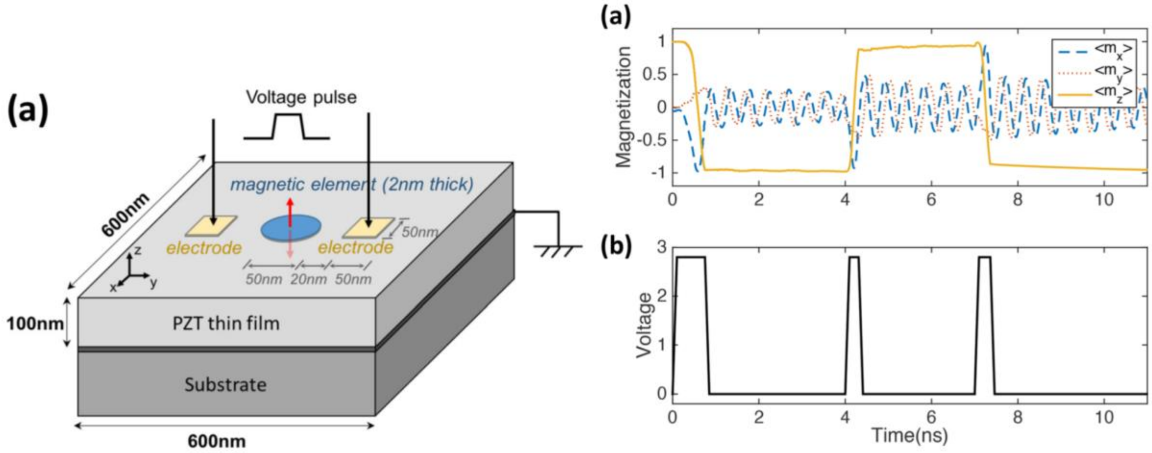

Figure 4.1. (Left) Structure for the strain-mediated 180° PMA switching (Right) Consecutive 180° perpendicular switching of CoFeB by applied voltage pulses [6].

4.1.2 Origin of PMA

Multilayers based on transition metal (TM) like Co, Fe and CoFe and a noble metal such as Pt, Pd and Au show perpendicular magnetic anisotropy for a certain range of thickness and number of periods [2,7-10]. Although these materials have been extensively studied for magneto-optics and magnetic recording, especially bit-patterned media, they have also gained interest in spintronics applications. The magnetic properties of these materials such as saturation magnetization and anisotropy energy can be easily tailored changing the number of bilayers and also by adjusting the thicknesses of TM and Pt (or Pd). The commonly used multilayers so far are Co/Pd, Co/Pt and Co/Ni due to their relatively larger PMA compared to Co/Au or Co/Ag for example. Firstly, multilayers were used as part of spin valves in the soft layer and hard layer without the need of anti-ferromagnetic layer which is required for the in-plane magnetoresistive case. In an earlier work on Co/Pd multilayers, Carcia et al. demonstrated that for Co thickness less than 0.8 nm the multilayer showed PMA which has been attributed to the surface anisotropy at Co and Pd interfaces and the strain in Co thin layers [7].

More recently, Yakushiji et al. showed that by using very thin Co and Pd (or Pt) of less than 0.2 nm, it is possible to achieve a high tunneling magnetoresistance (TMR) in MgO based junctions [11]. The multilayer called superlattice can be annealed at a high temperature exceeding 350 °C which is important for promoting the (001) phase of MgO, essential for high TMR. In comparison, the conventional multilayers (referring to relatively thicker Co and Pd) will face degradation of their intrinsic properties at such high temperature because of the Co and Pd (or Pt) intermixing. As can be seen in Fig. 4.2, a TMR of 62% could be obtained in a structure where the soft layer is composed of $[\mathrm{Co}(0.2\ \mathrm{nm})/\mathrm{Pd}(0.2\ \mathrm{nm})]_4$ and 0.8 nm thick $\mathrm{Co}_{60}\mathrm{Fe}_{20}\mathrm{B}_{20}$. The hard layer is composed of 1.3 nm CoFeB and 16 nm TbFeCo. Although Co/Pd and Co/Pt superlattices can be annealed at 350 °C without degradation of their magnetic properties, the existence of TbFeCo as part of the hard layer limits the annealing temperature. It is then expected that larger TMR could be obtained if one could find a replacement material for the hard layer [2].

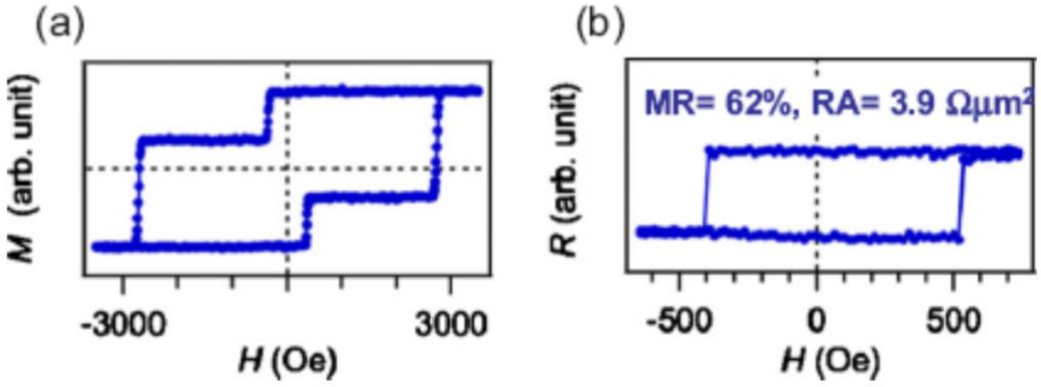

Figure 4.2. (a) Magnetization versus field and (b) resistance versus field for perpendicular MgO-based MTJ with a free layer made of $[Co(0.2\ nm)/\ Pd(0.2\ nm)]_4/Co_{60}Fe_{20}B_{20}$ (0.8 nm) [2,11].

The heavy metal elements of the multilayer PMA structures (i.e. Pd and Pt) has a strong spin-orbit coupling resulting in the several times larger damping constant α and the higher switching current. In 2010, first principle calculations conducted by Shimabukuro predicted that the hybridization of Fe-3d and O-2p orbitals may introduce PMA in a MgO/Fe/MgO system [12]. In the same year, Ikeda et al. demonstrated PMA in CoFeB-MgO-based MTJ devices as can be seen in Fig.4.3 [13]. The easy axis of magnetization of a CoFeB layer is in-plane of the film for a relatively large thickness (more than 1.5 nm or so) while it is oriented in the out-of-plane direction for small thickness. The PMA energy density (K_u) of the CoFeB-MgO system increases with reducing CoFeB thickness. The achieved K_u could support a memory cell size as small as 40 nm with 10 years of thermal stability.

On the other hand, the STT study shows that J_{c0} of the system has a fairly low value of 4 MA/cm^2, despite the thermal stability factor of 46. J_{c0} is the value of J_c when an STT current pulse of 1 ns is applied. Since the system is based on crystallized CoFeB-MgO structure, a TMR of more than 100% was achieved. The demonstrated perpendicular CoFeB-MgO MTJ system combines sufficient thermal stability, low switching current, and relatively high TMR signal. Having these characteristics at the same time is a real breakthrough for STT-MRAM.

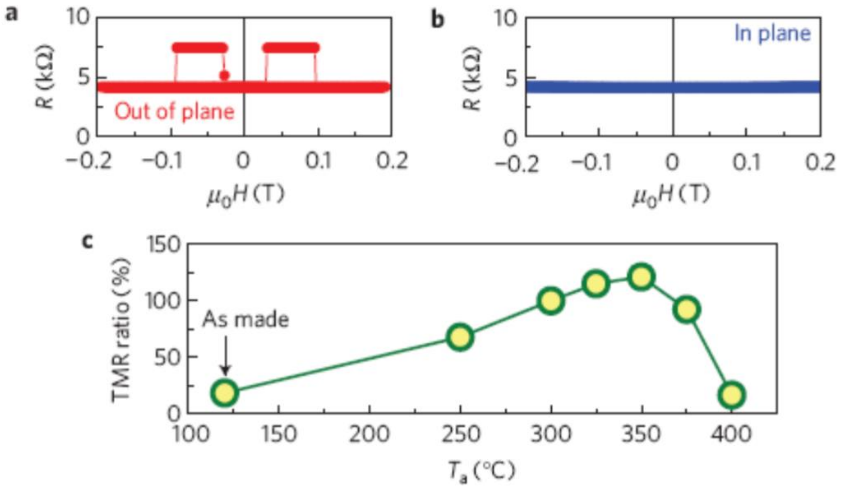

Figure 4.3. Resistance versus magnetic field for CoFeB/MgO/CoFeB with 150 nm device size annealed at 300 °C. (a) and (b) are cases where the magnetic field is applied out-of-plane and in-plane, respectively. (c) TMR as function of annealing temperature [13].

The PMA structures previously discussed are based on the interface effects from the very thin regime (sub-nm) and have very small magnetoelastic properties. In order to apply a PMA element to the strain-mediated multiferroics, PMA materials having high magnetoelastic effects are required. Moreover, the PMA material without the thickness restriction (i.e. very thin as several nm) will be preferred because the thermal stability of the magnetic cell is proportional to a volume of the cell. For many amorphous rare earth-transition metal (R-T) alloys, uniaxial anisotropy energy, $E_u = K_u sin^2\theta$, was found in fairly thick films with values of the uniaxial anisotropy constant, K_u, some hundred kJ/m^3. θ represents the angle between the preferred axis and the direction of magnetization. Significant larger K_u values occur for amorphous transition metal-based alloys when the alloy is formed of two different magnetic atoms. The strong uniaxial anisotropies occurring in R-T films are due to the deposition process (evaporation or sputtering) causing a locally anisotropic atomic arrangement that leads to a preferred axis parallel to the film normal (K_u > 0) or to an easy plane (K_u < 0) of magnetization [14].

The magnitude of K_u depends on the degree of short-range order and the magnitude of the magnetic anisotropy per atom. The former is primarily controlled by the energy of the atoms at the growing surface and the latter by spin-orbit coupling leading to high anisotropies for R-T alloys with non-S-state rare earths like Tb or Dy. Different origins were discussed to account for the observed anisotropies such as structural inhomogeneities, incorporation of oxygen, columnar microstructures, stress-induced anisotropies, dipolar interactions, pair ordering, anisotropic exchange, and anelastic deformation [14].

In 1991, Shih-Cheng N. et al. investigated the separation of perpendicular anisotropy components in dc-magnetron sputtered TbFe amorphous films [15]. The inverse magnetostrictive anisotropy component was determined by comparing the anisotropy of $Tb_{30}Fe_{70}$ films when they were removed from their substrates and when they were still attached to their substrates. The single-ion anisotropy component was then derived by subtracting the pair-ordering anisotropy, which was determined as the anisotropy of $Gd_{21}Fe_{79}$ films which had been removed from their substrates, from the anisotropy of $Tb_{30}Fe_{70}$ films which had been removed from their substrates.

Figure 4.4 shows single-ion, pair-ordering, and inverse magnetostrictive anisotropy components of the TbFe films, separated based on the method described earlier [15]. The inverse magnetostrictive anisotropy was determined as the anisotropy changes due to removing the films from their substrates. The inverse magnetostrictive anisotropy remains relatively constant at 1.3 × 10^6 ergs/cm^3 as the argon pressure is increased from 6 to 9 mTorr and decreases to 0.6 × 10^6 ergs/cm^3 at the argon pressure of 14 mTorr. This anisotropy component contributes 30 - 65% of the total anisotropy of these $Tb_{30}Fe_{70}$ films. The anisotropy, 1.3 - 2.0 × 10^5 ergs/cm^3, of GdFe films, which have been removed from their substrates, is assumed to be equal to the pair-ordering anisotropy component of $Tb_{30}Fe_{70}$ films. The pair-ordering anisotropy contributes less than 10% of the total anisotropy. The single-ion anisotropy is obtained by subtracting the pair-ordering anisotropy from the anisotropy 0.7 - 1.3 × 10^6 ergs/cm^3 in $Tb_{30}Fe_{70}$ films, which have been removed from their substrates. The single-ion anisotropy increases from 0.6 to 1.1 × 10^6 ergs/cm^3 with an increase of the argon pressure and contributes 30 - 60% of the total anisotropy.

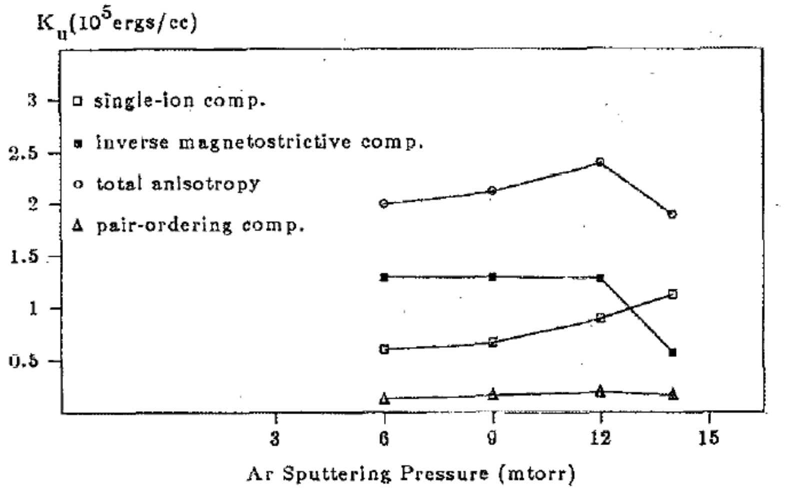

Figure 4.4. Single-ion, inverse magnetostrictive, and pair-ordering anisotropy components as percentages of total anisotropy in $Tb_{30}Fe_{70}$ films [15].

Figure 4.5 presents the dependences of K_u on composition and temperature and the comparison with calculation results from the mean-field analysis. They revealed a good agreement for various alloy compositions. The compositional variation of K_u of amorphous TbFe alloys demonstrates the strong influence of composition on the magnitude of K_u. The deposition parameters of sputtering sensitively affect K_u such as sputter gas, gas pressure, bias voltage, or substrate temperature [14]. The influence of the substrate temperature on K_u is shown in Fig. 4.5(a) for magnetron sputtered TbFe alloys, reflecting the reduction in mobility of adatoms on the film surface with decreasing substrate temperature [16]. The anisotropy of amorphous TbFe alloys is larger by more than one order of magnitude as compared to the Gd-based alloys which are associated with the high single-ion contribution of the Tb. In that case, a linear increase of K_u with the R content is expected and indeed can be observed as shown in Fig. 4.5(b) [17].

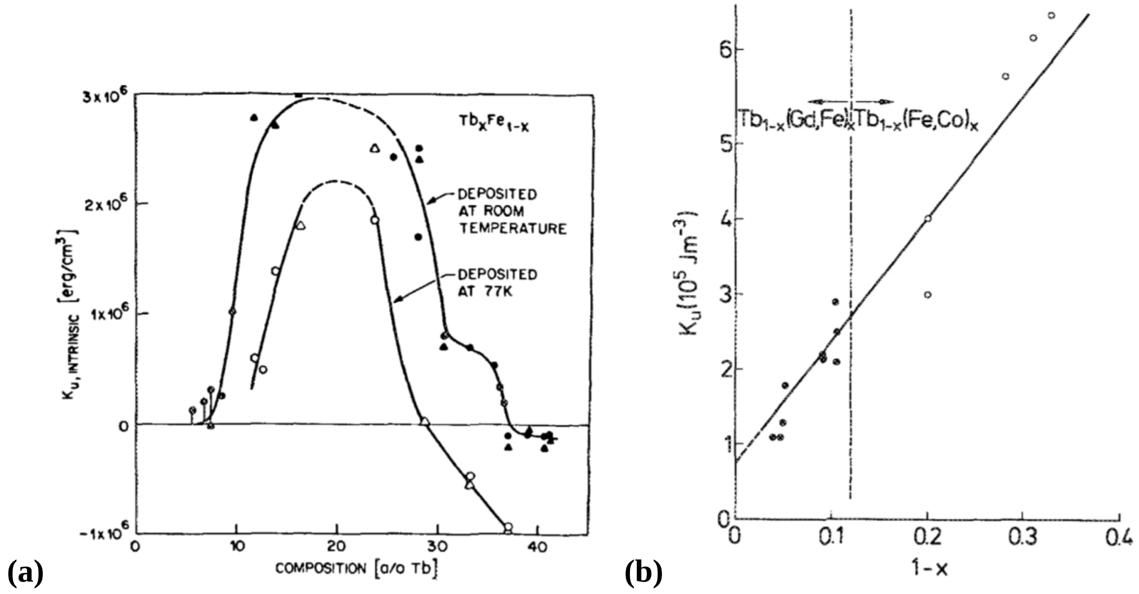

Figure 4.5. (a) The intrinsic anisotropy of TbFe thin films as a function of composition. (b) Variation of the uniaxial anisotropy constant with the Tb content at T = 295 K for GdTbFe and TbFeCo alloys [16,17].

4.2 Fabrication of PMA TbFe Films

The various possible origins of amorphous PMA R-T alloys are discussed in Chapter 4.1.2. Among them, two factors of columnar microstructure and stress-induced anisotropy are selected and experimentally tested. First, the design of experiment for columnar microstructure is motivated by the cross-sectional TEM images taken in the ESM TbFe film discussed in Chapter 3. Figure 4.6 shows one of the TEM images of TbFe film, indicating the amorphous state of the film. The in-plane and out-of-plane directions are indicated by red arrows beside the image. Other than the absence of crystallinity, we can see some preferred atomic arrangements along the specific axis from the image (marked as red lines), and the axis is parallel to the in-plane axis of the film. Hence, one hypothesis brought from this is that this film shows in-plane anisotropy due to this atomic arrangement, and the film having PMA can be obtained if the arrangement is rotated to the out-of-plane axis.

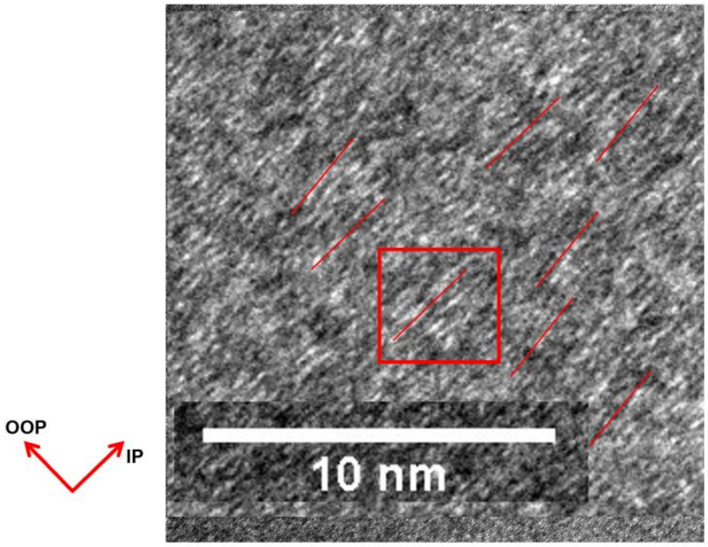

Figure 4.6. Cross section TEM image of the ESM TbFe thin film from Chapter 3. In-plane and out-of-plane directions are indicated by red arrows, and the preferred atomic arrangements are marked on the image by red lines.

The in-plane atomic preference can be attributed to the unique sputtering tool where the gun is installed with an angle and the substrate holder rotates during depositions. The rotational motion can influence in the atomic arrangements on the film and make in-plane axis more stable sites. Figure 4.7 represents the design of the experiment to verify the hypothesis. The left panel represents a substrate holder rotation during the deposition as other previous films while on the right panel the holder is fixed to the position just below the TbFe sputtering gun. The same sputtering parameters are applied to the two depositions except for the deposition time which is controlled to have the same film thickness (i.e. 1/3 of time for the fixed holder).

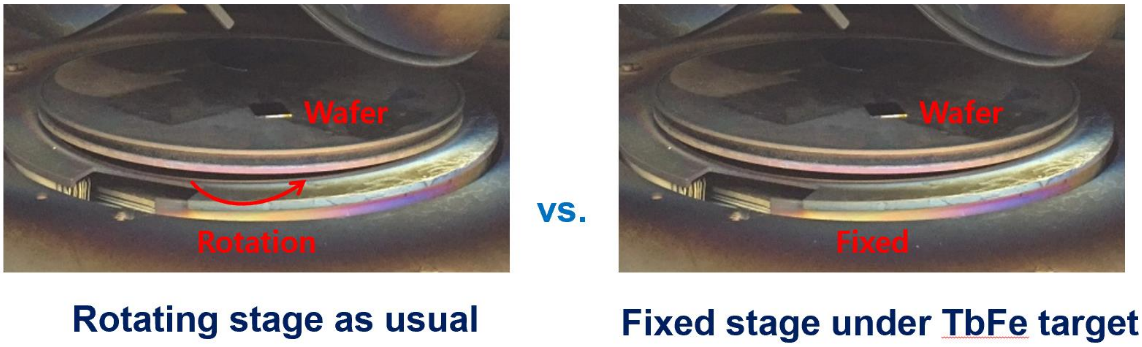

Rotating stage as usual

Fixed stage under TbFe target

Figure 4.7. Experiment setting to check the sample stage rotation dependence on TbFe anisotropy.

Figure 4.8 shows the out-of-plane MOKE M-H loops measured in the TbFe films deposited on the rotating substrate holder (left) and on the fixed holder (right). The thickness of both films is ~270 nm, which is about two order thicker than the transition metal film thickness showing PMA. As can be seen, both loops are showing high magnetic remanence and clear switching, indicating that the films have an easy axis along the normal to the film surface. The coercive fields, on the other hand, have a noticeable difference between the two films. The fixed-holder TbFe film has a higher coercive field (1250 Oe) than the rotated-holder one (1000 Oe). This means that the fixed-holder TbFe has larger PMA constant (K_u) due to the reduced preference for the in-plane atomic arrangement.

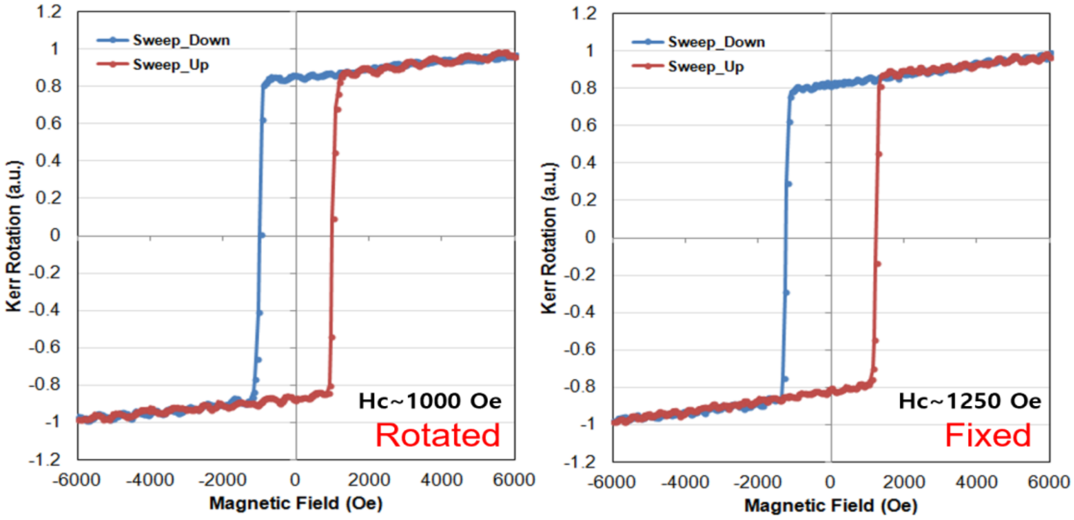

Figure 4.8. Out-of-plane MOKE M-H loops measured in TbFe films fabricated on the rotating substrate holder (left) and on the fixed holder (right).

The second important factor that can influence in PMA of TbFe films is the stress-induced anisotropy. It means that some residual stress formed on the film during deposition, in turn, induces magnetoelastic anisotropy to the TbFe film due to the high magnetostrictive property of TbFe. Since it is difficult to estimate the deposition parameters that directly impact on the residual stress, many parameters are tested and their results should be quantitatively analyzed. For the quantitative analysis of the PMA, both of in-plane and out-of-plane M-H loops with absolute magnetization values are required. Figure 4.9 represents the two TbFe films' M-H loops of in-plane and out-of-plane geometry measured by SQUID. Both films are showing clear magnetic preference to the out-of-plane axis. Based on the M-H loops from many different deposition conditions, the detailed discussion will be discussed in the next chapter.

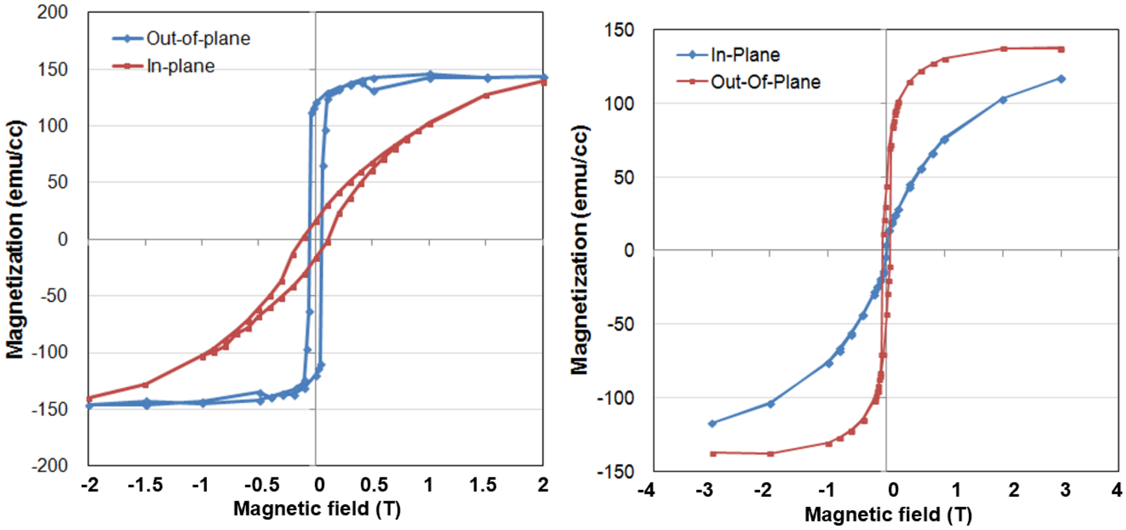

Figure 4.9. SQUID M-H loops along in-plane and out-of-plane axis measured in two TbFe films.

Figure 4.10 displays schematics for the potential designs of PMA TbFe for the practical strain-mediated 180° switching while the actual fabrication is not covered in this dissertation. The upper panel represents the PMA TbFe film deposited on a crystalline PMN-PT substrate that can be 180° switched by an applied voltage. When a voltage is applied between the bottom electrode and top TbFe film, a strain along the diagonal axis is induced in PMN-PT and transferred to the TbFe film as an in-plane strain. The strain will switch the perpendicular magnetization of TbFe into in-plane axis. When the input voltage is turned off, the in-plane magnetization will rotate to one of perpendicular directions (up or down). The bottom panel shows a design for nano-patterned PMA TbFe on PZT substrate. This is basically the same structure with one in Fig. 4.1 except for the thickness of the magnetic cell. For TbFe films, the thickness can be much thicker than transition metal-based PMA materials, which are significantly affected by their thickness.

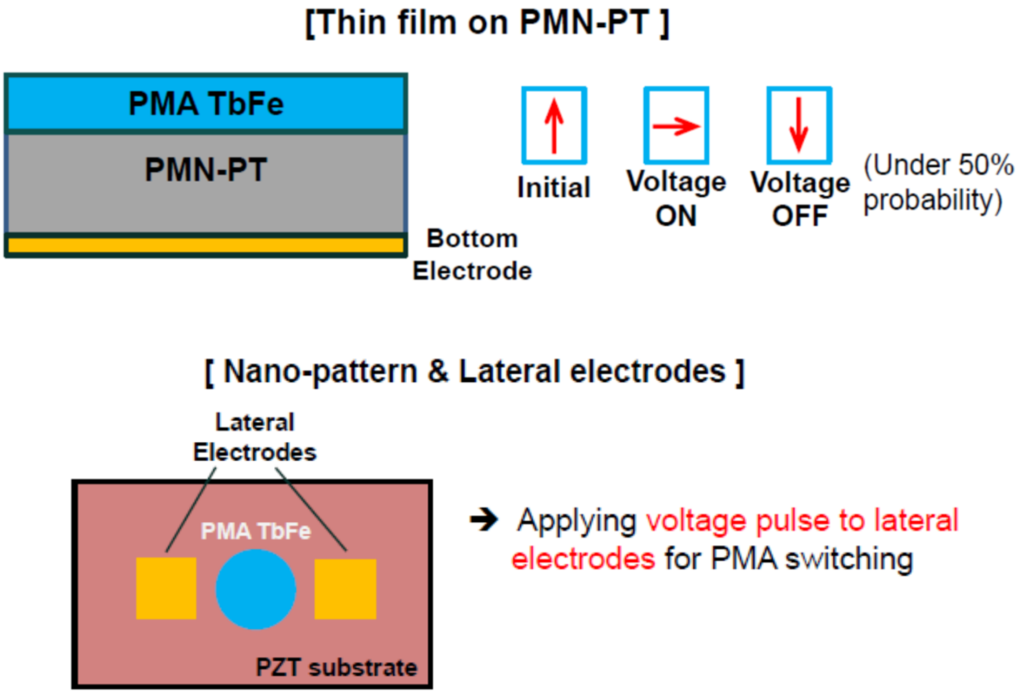

Figure 4.10. Potential designs of PMA TbFe to realize a voltage-applied 180° PMA switching. (Upper) Thin film TbFe deposited on PMN-PT and (Bottom) nano-patterned TbFe deposited on PZT along with lateral electrodes besides the magnetic pattern.

4.3 Parameters Affecting PMA of TbFe Films

The deposition parameters of Ar gas pressure and sputtering power are controlled to see their impact on the residual film stress of TbFe films. However, both deposition parameters also have a crucial influence in the relative atomic composition of the films as discussed in Chapter 3, and there is a strong atomic composition dependence on the PMA constant (see Fig. 4.5). In order to figure out the dependence between deposition parameters, residual stress, atomic composition, and PMA, quite complex, but systematic studies are required. Figure 4.11 depicts the correlations between the input parameters, intermediate properties, and PMA. The factor of holder rotation and the microstructure discussed in the previous chapter is also included in the figure.

In Fig. 4.11, each dependence (or relationship) is marked as its specific numbers for convenient explanations. For example, the holder rotation dependence on microstructure (#1) is just presumed, and the microstructure dependence on PMA (#2) is checked by the M-H loops in Fig. 4.8. From the following paragraphs, each dependence from #3 will be discussed using proper analysis tools and their plots.

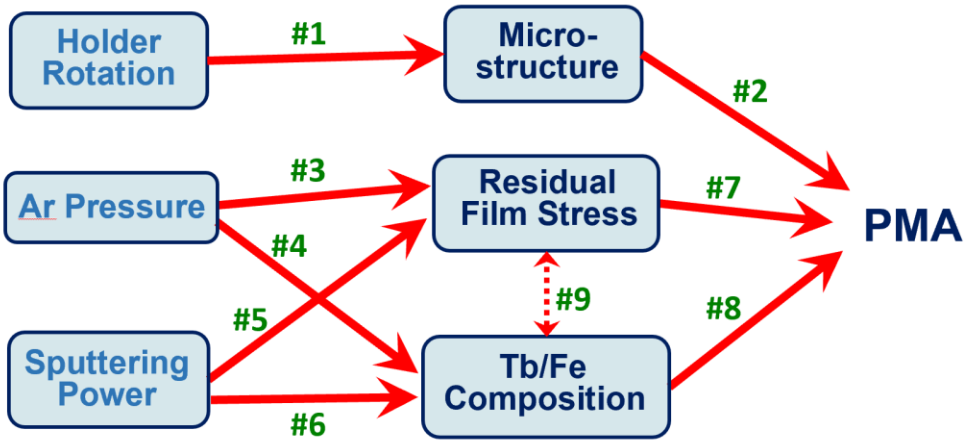

Figure 4.11. Diagram showing input parameters and intermediate properties affecting PMA. Each dependence (or relationship) is numbered for convenient explanations.

The residual film stress is measured using a wafer curvature technique employing a dual wavelength (λ_1 = 670 nm and λ_2 = 750 nm) Tencore Flexus 2024 system [18]. The average film stress, σ, is calculated using Stoney's equations $\sigma = \frac{1}{6R}\frac{E}{1-\nu}\frac{{t_{sub}}^2}{t_{film}}$. Here R is the relative radius of curvature, $\frac{R_1 R_2}{(R_1 - R_2)}$. R_1 and R_2 are the radii of curvature of the substrate before and after deposition, the elastic properties of the Si substrate are E = 130 GPa, ν = 0.25, and the thickness of the film and the thickness of the substrate are t_{film} and t_{sub}, respectively.

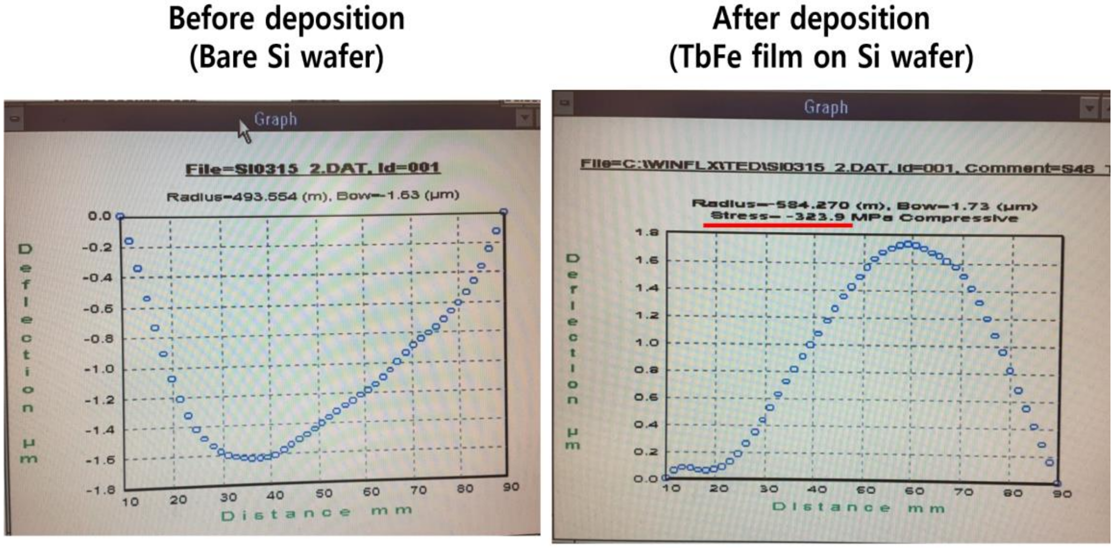

Before deposition (Bare Si wafer)

```
File=SI0315 2.DAT, Id=001
Radius=493.554 (m), Bow=-1.63 (µm)
```

After deposition (TbFe film on Si wafer)

```
File=C:\WINFLX\TED\SI0315 2.DAT, Id=001, Comment=S48
Radius=-584.270 (m), Bow=1.73 (µm)
Stress= -323.9 MPa Compressive
```

Figure 4.12. The measurements on wafer curvature and its residual stress detected by a dual wavelength Tencore Flexus 2024 system. Two sets of curvature measurements are needed before (left) and after (right) the film deposition.

Figure 4.12 shows a representative result on the residual film stress of TbFe film. For this measurement, 3-inch full Si substrate is prepared and TbFe film is deposited on it without dicing. The left plot of Si substrate curvature is measured before the TbFe deposition, and the curvature radius of 493.554 m is recorded. After the TbFe deposition on the exact Si substrate, the curvature measurement is performed again as shown in the right plot. The sign of curvature is reversed by the TbFe deposition, and the curvature radius is -584.27 m. Along with the curvature radius, the residual stress value is extracted using the Stoney's equation and the result on bare Si substrate, and the measured stress is -323.9 MPa (i.e. compressive stress). Note that all the PMA TbFe films show in-plane compressive stress, which is obvious in that out-of-plane tensile stress should be induced from it resulting in the perpendicular magnetoelastic anisotropy.

The PMA constant (K_u) of the TbFe films is quantitatively extracted from the M-H loops of in-plane and out-of-plane axis. Figure 4.13 graphically presents an example of the calculation method for K_u. The area between two M-H curves represents the anisotropy constant, K_u, and it can be calculated by $\int M_{OOP}\, dH - \int M_{IP}\, dH$.

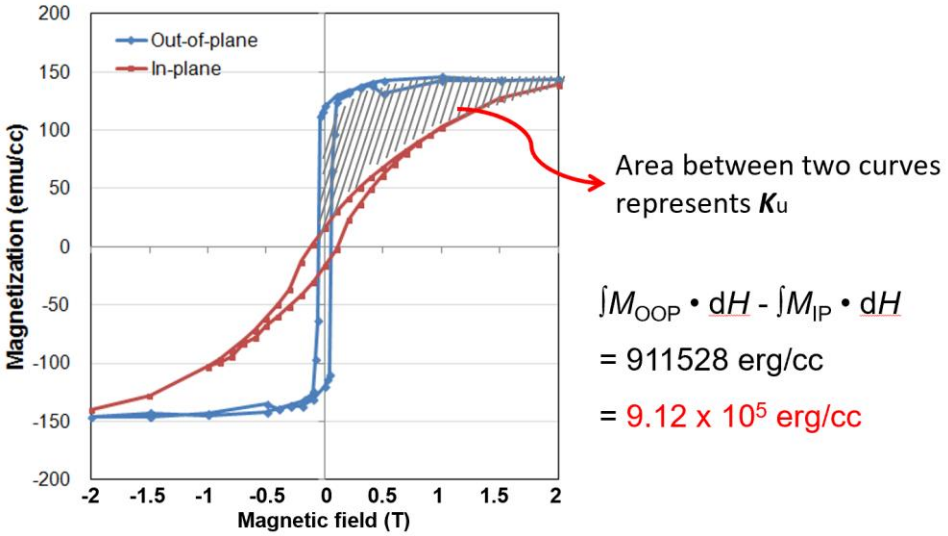

Area between two curves represents $\boldsymbol{K}_u$

$\int M_{OOP} \bullet dH - \int M_{IP} \bullet dH$

$= 911528$ erg/cc

$= 9.12 \times 10^5$ erg/cc

Figure 4.13. An example of the calculation method for K_u. The area between in-plane and out-of-plane M-H curves represents the anisotropy constant, K_u.

The values for K_u and residual stress are measured in all the deposited TbFe films using the mentioned methods. Also, the Tb atomic compositions are measured for all the films by using ICP-MS and EDS. Figure 4.14 plots the Ar pressure dependence on the residual stress (#3) and the

Tb atomic composition (#4). Since some of the data points are from the depositions using different sputtering power, the overall tendency seems a little ambiguous. However, the higher compressive residual stress values are measured in the low Ar pressure condition. This trend is corresponding to the previous results on as-deposited amorphous Terfenol-D films presented in [18]. At low Ar pressures, sputtered atoms have higher energy at substrate surface than at high pressures due to the reduced collisions with Ar ions. So, their higher surface mobility produces dense amorphous films with compressive stress while at higher Ar pressures, less energetic sputtered atoms produce films with tensile stresses [18]. The Tb atomic composition, on the other hand, increases as the Ar pressure increases. This Tb composition results as a function of Ar pressure are in sync with the one in Chapter 3 (see Fig. 3.17).

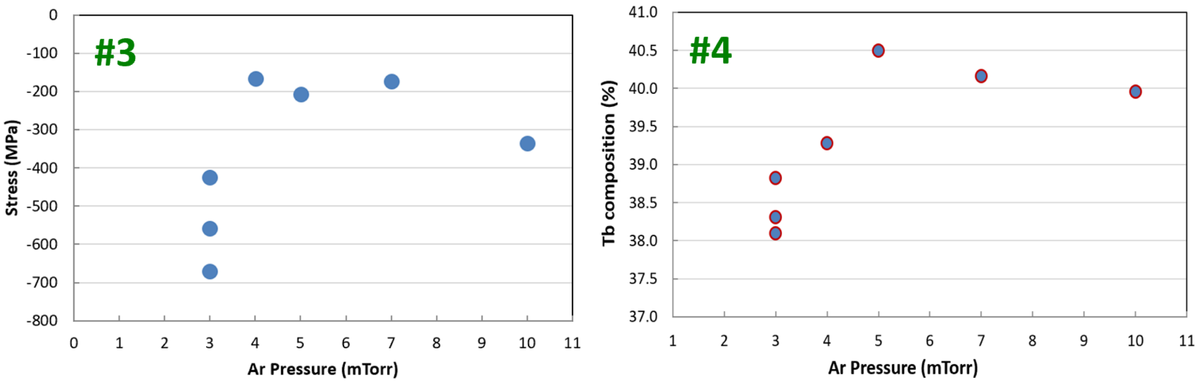

Figure 4.14. The Ar pressure dependence on the residual stress (#3) and the Tb atomic composition (#4).

Figure 4.15 shows the plots of the sputtering power dependence on the residual stress (#5) and the Tb atomic composition (#6). The highest compressive residual stress value is measured in the high sputtering power condition, which also can be explained by the higher surface mobility that the sputtered atoms have. The Tb atomic composition roughly decreases as the sputtering power increases. The Tb composition results depending on the sputtering power match with the one in Chapter 3 (see Fig. 3.16). Since some of the films are fabricated using different Ar pressure, there are several tangent data points from the trend.

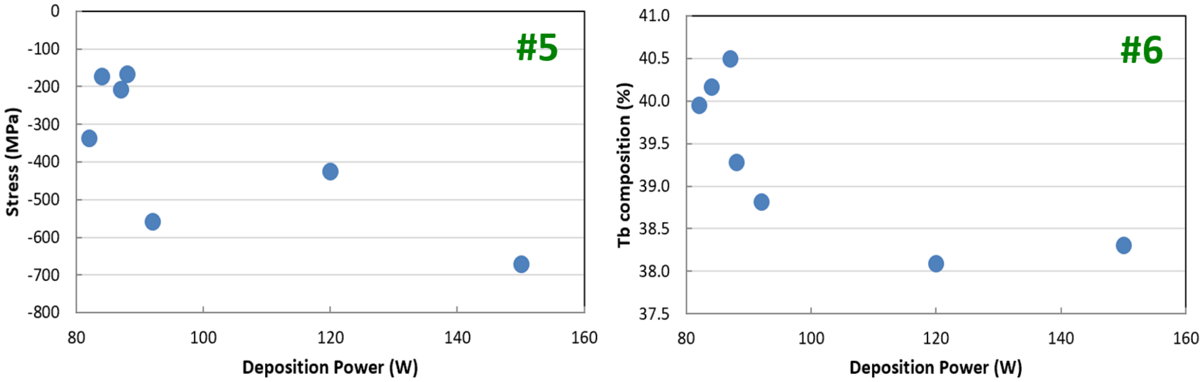

Figure 4.15. The deposition power dependence on the residual stress (#5) and the Tb atomic composition (#6).

So far, the dependences of the deposition parameters on the intermediate properties are investigated. The ultimate impacts of the intermediate properties on PMA of TbFe films are plotted in Fig. 4.16. The left panel shows the residual stress dependence on the PMA of TbFe films (#7), and the right the Tb atomic composition dependence (#8). Note that the anisotropy constants are plotted in a log scale for both panels. As the residual compressive stress increases, the K_u increases, and as the Tb atomic composition increases, the K_u decreases. Form these sets of correlations, the residual compressive stress has a strong impact on the films' PMA, but there also are other important factors like the atomic composition. This complex influence should be accepted since even for the fixed residual stress, the induced magnetoelastic anisotropy is proportional to the magnetostriction coefficient (λ_S) of the films, and the λ_S, in turn, is a function of the relative atomic composition as discussed in Chapter 3.

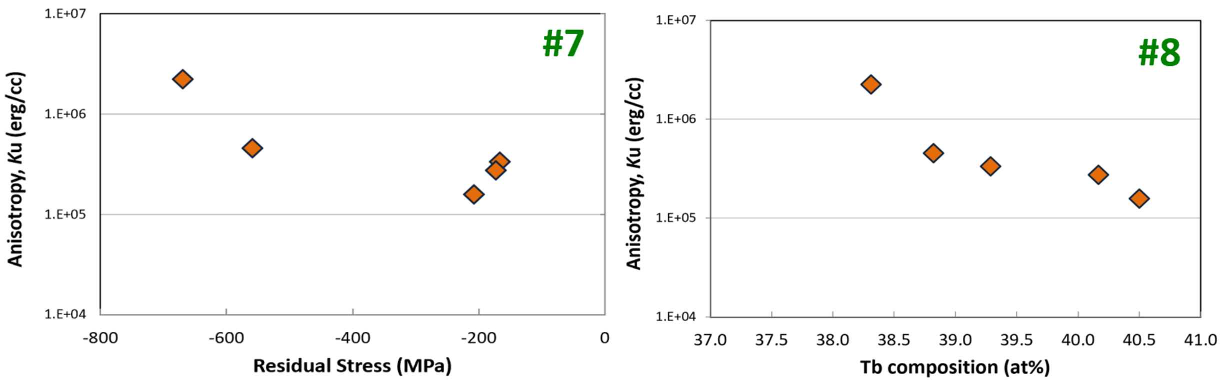

Figure 4.16. The residual stress (#7) and Tb atomic composition (#8) dependence on the anisotropy constant (K_u).

As a reference, the relationship between the residual stress and Tb atomic composition (#9) is plotted in Fig. 4.17. There seems a linear correlation between them: the residual compressive stress increases as Tb composition decreases. However, more complex parameters should be reviewed in more number of samples in order to explain this tendency.

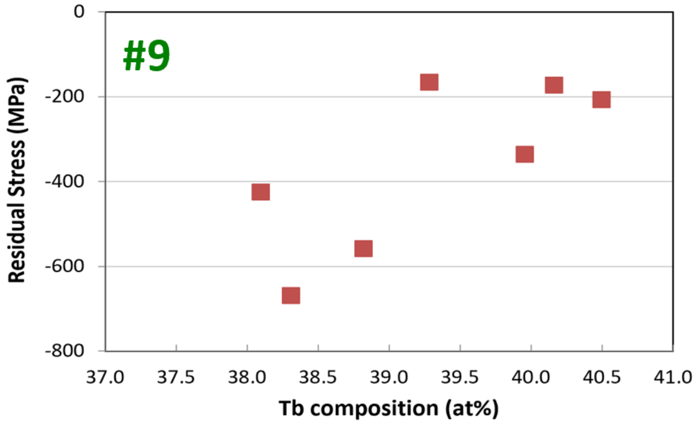

Figure 4.17. The relationship between the residual stress and Tb atomic composition (#9).

Up to now, all the dependencies and relationship marked in Fig. 4.11 are discussed. Each parameter and each intermediate property have an impact on PMA in either explainable or unclear ways. So, from these researched baselines, more studies on various parameters should be performed to figure out the origins of PMA in TbFe films.

4.4 Chapter References

1] M. Wang, Y. Zhang, X. Zhao, and W. Zhao, Micromachines, **6**, 1023-1045 (2015)

2] R. Sbiaa, H. Meng, and S. N. Piramanayagam, Phys. Stat. Sol. RRL, **5**, 413 (2011)

3] Y. Zheng, and J.-G Zhu, J. Appl. Phys. **81**, 5471 (1997)

4] S. Mangin, D. Ravelosona, J. A. Katine, M. J. Carey, B. D. Terris, and E. E. Fullerton, Science, **5**, 210 (2006)

5] R. Sbiaa, S. Y. H. Lua, R. Law, H. Meng, R. Lye, and H. K. Tan, J. Appl. Phys. **109**, 07C707 (2011)

6] Q. Wang, X. Li, C. Liang, A. Barra, J. Domann, C. Lynch, A. Sepulveda, and G. Carman, Appl. Phys. Lett. **110**, 102903 (2017)

7] P. F. Carcia, A. D. Mcinhaldt, and A. Sunna, Appl. Phys. Lett. **47**, 178 (1985)

8] F. J. A. den Broeder, H. C. Donkersloot, H. J. G. Draaisma, and W. J. M. de Jonge, J. Appl. Phys. **61**, 4317 (1987)

9] B. N. Engel, C. D. England, R. A. Vanleeuwen, M. H. Wiedmann, and C. M. Falco, J. Appl. Phys. **70**, 5873 (1991)

10] T. Sugimoto, T. Katayama, Y. Suzuki, M. Hashimoto, Y. Nishihara, A. Itoh, and K. Kawanishi, J. Magn. Magn. Mater. **104–107**, 1845 (1992)

11] K. Yakushiji, T. Saruya, H. Kubota, A. Fukushima, T. Na-gahama, S. Yuasa, and K. Ando, Appl. Phys. Lett. **97**, 232508 (2010).

12] R. Shimabukuro, K. Nakamura, T. Akiyama, and T. Ito, Physica E, **42**, 1014 (2010)

13] S. Ikeda, K. Miura, H. Yamamoto, K. Mizunuma, H. D. Gan, M. Endo, S. Kanai, J. Hayakawa, and H. Ohno, Nat. Mater. **9**, 721 (2010)

14] P. Hansen, Handbook of Magnetic Materials, **6**, 289-452 (1991)

15] S.-C. N. Cheng, and M. H. Kryder, J. Appl. Phys. **69**, 7202 (1991)

16] R. B. van Dover, M. Hong, E. M. Gyorgy, J. F. Dillon Jr., and S. D. Albiston, J. Appl. Phys. **57**, 3897 (1985)

17] P. Hansen, C. Clausen, G. Much, M. Rosenkranz, and K. Witter, J. Appl. Phys. **66**, 756 (1989)

18] K. P. Mohanchandra, S. V. Prikhodko, K. P. Wetzlar, W. Y. Sun, P. Nordeen, and G. P. Carman, AIP Advances, **5**, 097119 (2015)

5. Summary and Conclusion

This dissertation focused on developing thin-film magnetoelastic materials that can be applied to practical strain-mediated multiferroic devices. Since various multiferroic devices demand different requirements for magnetic materials, magnetoelastic materials having different key features have been investigated.

In Chapter 2, the high-quality polycrystalline Terfenol-D films, showing the highest magnetostriction at room temperature, are fabricated by optimizing the sputtering deposition conditions. Their material and magnetic properties are tested and confirmed to have high magnetoelastic properties. The elemental magnetic moments of the Terfenol-D films are investigated by using the XMCD technique. The spin and orbital moments of each element are separated by performing XMCD sum rule analysis. The correlation between the elements' orbital moments and crystalline anisotropy of the films is figured out as a function of temperature. As a result, it is turned out that the large difference of the orbital moments between Dy and Tb is partly responsible for the enhanced crystalline anisotropy of Terfenol-D films at low temperatures. The developed Terfenol-D films can be applied to fabricate various strain-mediated multiferroic devices such as a nanomotor, memory cell, or drug delivery system.

Chapter 3 focused on the amorphous magnetoelastic TbFe films representing ESM behavior. The ESM properties in TbFe films are enabled by the atomic composition gradient formed through the film thickness. The gradient produces Tb and Fe-dominant regions, and their exchange coupling at the interface creates an ESM behavior. By applying a mechanical strain to the film, a two-step switching with the negative coercive field is both modulated and eliminated showing the promise of 180° switching. The modulation is caused by the relatively higher magnetostriction coefficient in the Tb-dominant region compared to the Fe-dominant producing larger changes in magnetic anisotropy as the strain is applied. This strain-applied ESM switching mechanism can be used in future memory devices if more studies are conducted to overcome practical problems.

Chapter 4 presented the development of amorphous TbFe films having PMA and the correlations between the process parameters, intermediate properties, and PMA. For this work, another process parameter of substrate rotation is varied, and its effect on PMA is checked. Also, a wafer curvature technique is used to measure the residual stress of deposited films. The correlations between all the parameters and properties are plotted and analyzed. It is turned out that both of residual film stress and atomic composition strongly impact on the PMA property simultaneously. However, since the process parameters make a difference in the intermediate properties in combination, it is hard to figure out specific critical parameters affecting PMA. With more research works on this topic, the origin of PMA TbFe films will be realized, and eventually, they can be applied to practical strain-mediated devices which require 180° PMA switching.

The material developments of the magnetoelastic films are shown in various useful directions in this dissertation. It is true that the field of strain-mediated multiferroics still requires to overcome many challenges for its practical application such as embedding piezoelectric components to the existing systems and reducing the burden of rare earth elements' cost. However, I believe that the research on the high-quality and functional magnetoelastic films, presented here, will definitely facilitate the applications.